ABSTRACT

Brillouin and Transverse Mode Instabilities in Fiber Amplifiers
for High-Energy Laser Systems

Joshua T. Young, Ph.D.

Advisor: Jonathan Hu, Ph.D.

High-energy fiber lasers have developed a lot of interest due to their applications in industry, medicine, and defense. Recent advances enabled an explosive growth in operating power to the scale of multi-kilowatts. However, nonlinear effects such as the Brillouin instability (BI) and the transverse mode instability (TMI) impose limits on the power of high-energy fiber amplifiers. This dissertation focuses on the theoretical modeling of these nonlinear effects. The goal is to model these effects and further propose new mitigation techniques to increase the operating powers and advance the techniques for high-energy fiber amplifiers. The nonlinear effects in optical fibers often involve mode coupling. Avoided crossings occur when two modes are strongly coupled to each other and share similar propagation constants. We start with a tutorial to study avoided crossings in one-dimensional slab waveguides in both index guiding and antiresonant waveguides. We use simple one-dimensional slab waveguides as examples to illustrate the physics and properties of avoided crossings in more complicated specialty optical fibers. We study the TMI in an Yb-doped fiber amplifier in the presence of a single higher-order mode (HOM). Current modeling techniques for TMI require that the longitudinal discretization be substantially smaller than the beat length between the fundamental mode and HOM. We formulate the phase-matched model for TMI, which only considers the phase-matched

terms that contribute to the coupling between the fundamental mode and HOMs. By doing so, the number of sections in the longitudinal discretization may be greatly decreased, which leads to a large computational win with no loss of accuracy. The BI may be modeled as a three-wave mixing process where two optical modes interact with a resonant acoustic mode. We consider phase modulation of the input pump as a suppression technique for BI. We show that piecewise parabolic phase waveforms like sawtooth and triangle phase may provide larger power thresholds compared to that of the more commonly used pseudorandom bitstream (PRBS) modulation. Because of the nearly rectangular spectrum associated with piecewise parabolic phase modulation, these modulation schemes are better fitted for power scaling such as spectral beam combining. Recently, our piecewise parabolic phase idea that was published was experimentally demonstrated. We further consider a single computational model that models BI and TMI together. A multi-time-scale approach must be used since these nonlinear effects evolve over drastically different time scales. Both BI and TMI depend differently on the core diameter of the fiber. At and under the pump power threshold for the combined BI-TMI model, the pump power threshold closely follows that of the individual BI and TMI models. However, BI may trigger TMI when strong BI leads to stochastic oscillations in the fundamental mode amplitude. This feature cannot be predicted by modeling either BI or TMI alone. At the end, we discuss the future prospects for high-energy laser fiber amplifiers and give a summary.

Brillouin and Transverse Mode Instabilities in Fiber Amplifiers
for High-Energy Laser Systems

by

Joshua T. Young, B.S.

A Dissertation

Approved by the Department of Electrical and Computer Engineering

---

Kwang Y. Lee, Ph.D., Chairperson

Submitted to the Graduate Faculty of
Baylor University in Partial Fulfillment of the
Requirements for the Degree
of
Doctor of Philosophy

Approved by the Dissertation Committee

Jonathan Hu, Ph.D., Chairperson

Yang Li, Ph.D.

Robert J. Marks, Ph.D.

Linda Olafsen, Ph.D.

Jill Klentzman, Ph.D.

Accepted by the Graduate School
December 2022

J. Larry Lyon, Ph.D., Dean

Page bearing signatures is kept on file in the Graduate School.

TABLE OF CONTENTS

LIST OF FIGURES viii

LIST OF TABLES xi

ACKNOWLEDGMENTS xii

DEDICATION xiii

ATTRIBUTIONS xiv

1 Introduction 1

1.1 High-power lasers 1

1.2 Brillouin instability 2

1.3 Transverse mode instability 4

1.4 Other nonlinear effects 5

1.5 Organization of dissertation 6

2 Avoided Crossings in Slab Waveguides 7

2.1 Introduction 8

2.1.1 Avoided crossings in different devices 8

2.1.2 Brief history on the study of avoided crossings 9

2.2 Coupled-mode theory for guided modes in a slab waveguide 10

2.3 Example of mode coupling in a slab waveguide with guided modes . . 15

2.4 Coupled-mode theory in an antiresonant slab waveguide 18

2.5 Mode coupling in antiresonant slab waveguides 23

2.6 Avoided crossings in optical fibers 28

2.7 Summary 33

3 Phase-Matched Model for the Transverse Mode Instability 35

3.1 Introduction 35

3.2 Theoretical model 37

3.3 Verification, accuracy, and timing of the phase-matched model 43

3.3.1 Verification 43

3.3.2 Accuracy and timing 46

3.4 TMI as an STRS process 50

3.5 Coupled-mode theory background for TMI 51

3.6 Conclusions and discussion 60

4 Piecewise Parabolic Phase Modulation for BI Suppression 61

4.1 Phase modulation as a suppression technique 61

4.2 Theoretical model and parameters 67

4.3 Power threshold for different modulation schemes 68

4.4 Discussion 71

4.5 Conclusions 72

5 Tradeoff Between the Brillouin and Transverse Mode Instabilities 74

5.1 Introduction 75

5.2 Modeling scheme 77

5.3 Model for BI and TMI 79

5.4 BI and TMI threshold at core diameters of 30 and 45 μm 83

5.5 BI and TMI thresholds as a function of core diameter 86

5.6 Comparison of the individual and full models 88

5.7 Conclusions 94

6 Summary and Future Prospects 96

6.1 Summary 96

6.2 Future Prospects 98

BIBLIOGRAPHY 101

LIST OF FIGURES

1.1 Double clad fiber geometry. 2

1.2 Schematic of modes for BI. 3

1.3 Schematic of modes for TMI. 5

2.1 Illustration of index-guided structure and refractive index profiles. . . 11

2.2 Effective index of index-guided modes vs. changing core size. 16

2.3 Avoided crossing width calculated using the minimum difference in the effective index, δ, vs. the gap separation. 18

2.4 Illustration of the two-core antiresonant slab waveguide and refractive index profiles. 19

2.5 Effective index for the fundamental mode and loss vs. core size for an antiresonant slab waveguide. 25

2.6 Avoided crossing width and loss vs. glass thickness. 26

2.7 Avoided crossing width and loss vs. air gap. 27

2.8 Schematic structure of a rare-earth doped double-clad LPF. 28

2.9 Detailed plot of one broad and two narrow avoided crossings (marked in green vertical lines). 29

2.10 Transverse mode profiles of the modes involved in the broad avoided crossing of Fig. 2.9 around an air-clad diameter of 188.5 μm. 30

2.11 Schematic and modes for a negative curvature fiber. 31

2.12 Refractive indices and loss for negative curvature fiber. 32

3.1 Schematic flow diagram for the transverse-mode instability. 39

3.2 Power ratio $\rho(t) = P_{\mathrm{HOM}}(t)/P_{\mathrm{total}}(t)$ at the end of the amplifier vs. time t. 44

3.3 Maximum power ratio vs. input pump power. 45

3.4 Temperature and spatial Fourier transform vs. z. 47

3.5 Convergence of the maximum power ratio at the amplifier end as $L_B/\Delta z$ increases. 48

3.6 Relative error and runtime vs. $L_\mathrm{B}/\Delta z$. 49

4.1 Phase and frequency as a function of time. 65

4.2 Frequency spectra for various phase modulation types in linear and log scale. 66

4.3 Stokes power vs. laser power for different modulation types. 69

4.4 Normalized threshold vs. the period for different waveforms at 85% bandwidth. 70

4.5 Normalized threshold vs. the period for different waveforms at 90% bandwidth. 70

4.6 Normalized threshold vs. the period for different waveforms at 95% bandwidth. 71

5.1 Illustration of the tradeoff between the Brillouin instability and the transverse mode instability. 76

5.2 Time step scheme. 77

5.3 Illustration of the modes for the BI and TMI simulations. 78

5.4 Reflectivity ρ_S due to BI and the HOM content ρ_H due to TMI as a function of pump power for a core diameter of (a) $d = 30$ μm and (b) $d = 45$ μm. 84

5.5 Pump power threshold when we consider BI and TMI altogether or BI and TMI separately. 87

5.6 Reflectivity and HOM content from the full model and the TMI only model as a function of pump power. 89

5.7 Reflectivity and HOM content as a function of pump power and core diameter. 90

5.8 Absolute value of the difference in the predicted (a) reflectivity and (b) HOM content between the full and individual models. 92

5.9 Reflectivity and HOM content as a function of time for different pump powers with a core diameter of 30 μm. 93

LIST OF TABLES

3.1 TMI model simulation parameters 43

4.1 BI simulation parameters 68

5.1 BI-TMI model simulation parameters 85

ACKNOWLEDGMENTS

First off, I would like to thank my dissertation supervisor, Dr. Jonathan Hu, for introducing me to this dissertation topic. I've learned a lot about self-disipline and efficient working habits thanks to his strict and rigorous attitude toward research. I am grateful for his pateince, understanding, and willingness to guide me as I progessed through my research projects. I consider Dr. Jonathan Hu as a mentor and as a model for my professional career.

I would also like to thank my disertation committee members Dr. Yang Li, Dr. Robert J. Marks, Dr. Linda Olafsen, and Dr. Jill Klentzman for their helpful guidance and thoughtful discussions on my proposal, dissertation, and research.

I would like to thank Dr. Curtis R. Menyuk who has dedicated a lot of his time and effort towards our research projects. It's been an honor to work with such a distinguished professor.

I would like to give thanks to Mark Niece and Cristina Crowson and the rest of the Directed Energy Professional Society (DEPS) for supporting me throughout my time in graduate school.

I would like to recognize my friends and colleagues, Dr. Chao Niu, Dr. Chengli Wei, Wei Zhang, and Zhihao Hu for their help in both school and life.

I would like to thank my parents for giving me consistent and selfless support in the past 27 years. They taught me how to love, how to be thankful, and how to be humble and consistent. I believe these are the most precious treasures they have given me in my whole life.

Finally, I would like to thank Baylor University, where I spent my five years in graduate school.

To my parents

ATTRIBUTIONS

In Chapter One, Josh Young prepared the initial draft. Dr. Jonathan Hu provided comments and assisted in revising the chapter.

Chapter Two is based on the paper "Mode coupling at avoided crossings in slab waveguides with comparison to optical fibers: tutorial" in the *Journal of the Optical Society of America B*. The first author, Josh Young, wrote the initial draft for the paper and carried out simulation work to generate figures. The second author, Dr. Chengli Wei, also worked on simulation and assisted the first author. The third author, Dr. Curtis Menyuk, analyzed data, gave constructive suggestions, and contributed a lot to this revision. The last author, Dr. Jonathan Hu, worked as the advisor of the first author, Josh Young, to write this paper. All authors contributed to the revision of the paper.

Chapter Three is based on the paper "Accurate and efficient modeling of the transverse mode instability in high energy laser amplifiers" in the journal of *Optics Express*. Curtis Menyuk, the first author, proposed the original research idea, analyzed data, and revised much of the manuscript. Josh Young, the second author, prepared part of the initial draft and carried out simulation to generate figures. The third author, Jonathan Hu, worked as the advisor of the second author, Josh Young, and provided useful guidance and discussion along with the first author, Dr. Curtis Menyuk, as how to implement the theoretical model. The fourth, fifth, and sixth authors, Dr. Andy Goers, Dr. Michael Dennis, and Dr. David Brown, contributed useful discussions, gave constructive suggestions, and contributed a lot to this revision.

Chapter Four is based on the paper "Seeding fiber amplifiers with piecewise parabolic phase modulation for high SBS thresholds and compact spectra" in the journal of *Optics Express*. The first author, Jeffrey White, wrote the initial draft. The first author, Dr. Jeffrey White, and the fifth author, Dr. Curtis Menyuk proposed the original research topic. The second author, Josh Young, worked with the fourth author, Dr. Jonathan Hu, to regenerate Figs. 1, 6–9 in the paper. The third, fourth, and fifth authors, Dr. Chengli Wei, Dr. Jonathan Hu, and Dr. Curtis Menyuk analyzed data, gave constructive suggestions, and contributed a lot to this revision.

Chapter Five is based on the paper "Tradeoff Between the Brillouin and Transverse Mode Instabilities in Yb-doped Fiber Amplifiers" in the journal of *Optics Express*. The first author, Josh Young, carried out simulations to generate figures and prepared the first draft. Dr. Andy Goers, Dr. David Brown, Dr. Michael Dennis, Dr. Kevin Lehr, and Dr. Curtis Menyuk proposed original research topic. The seventh author, Dr. Curtis Menyuk, worked with the first author, Josh Young, and eighth author, Dr. Jonathan Hu to implement the theoretical model into a simulation. The eighth author, Dr. Jonathan Hu, worked as the advisor of the first author, Josh Young, to write the paper. All authors analyzed data, gave constructive suggestions, and contributed a lot to the revision.

In Chapter Six, Josh Young prepared the initial draft. Jonathan Hu provided comments and assisted in revising the chapter.

CHAPTER ONE

Introduction

1.1 High-power lasers

Fiber lasers have desirable features such as robust single mode operation, high gain, and efficient energy conversion [1–4]. Over the last few decades fiber lasers have seen an explosive increase in operating powers [1–4]. Originally fiber lasers were thought to only apply to telecommunication applications because of low attenuation and the ability to support high-capacity channels compared to regular cables [3, 5–7]. The performance improvement has made fiber lasers a successful, fast increasing commercial business, thanks to the advanced technologies in high-quality fibers and fiber components. High energy lasers now have a plethora of applications ranging from material machining and cutting [8], medicine [8], and defense [8, 9]. Even with 60 years of successful active research since laser invention [10], the research on high-power lasers has not reached an end, and the demand for lasers with a higher power keeps increasing. High-energy fiber amplifiers have made significant headway and improvement in output powers due to the use of double-clad fiber geometries [11, 12], which were first proposed in 1974. Figure 1.1 shows a schematic of the double-clad fiber geometry. The dark blue region represents the high index doped core, the black circles in the dark blue region represent the rare-earth dopants, the light blue region represents the inner cladding, the dark gray region shows the outer cladding, and the red and yellow arrows represent the pump and signal light, respectively. The main benefit of the double-clad fiber is the ease of getting the pump light into the fiber. Rather than attempting to couple high power pump light into a small core, the double-clad fiber has a high power, low brightness pump injected into a much larger inner cladding. As the pump light propagates down the fiber, the light gets absorbed by a rare-earth doped core. The result is extremely efficient conversion of low brightness pump light into a high-power coherent output. Since then, there has been an almost exponential growth in output power for continuous wave lasers, reaching to the 10-kW level [13]; however, further increase of the power threshold in single mode fibers has been challenging.

Nonlinear effects have regularly been a roadblock in achieving larger output powers, such as self-focusing [14], stimulated Raman scattering (SRS) [14], the Brillouin instability (BI) due to stimulated Brillouin scattering (SBS) [14], and the transverse mode instability (TMI) [15]. While extensive work has been done on the modeling and mitigation of certain nonlinear effects, the interaction between multiple nonlinear effects is not well understood. With current suppression techniques and fiber designs, BI and TMI appear to be the main limiting nonlinear effects that prohibit further power scaling. There is a strong motivation to further study these effects so that effective simulation modeling tools and mitigation techniques may be developed to increase operating powers. The study of the BI and TMI is the focus of this dissertation.

1.2 Brillouin instability

The Brillouin instability (BI) arises in fiber amplifiers from stimulated Brillouin scattering (SBS). For SBS to emerge, thermally seeded acoustic phonons interact with a forward propagating optical mode. At low input pump powers, this interaction

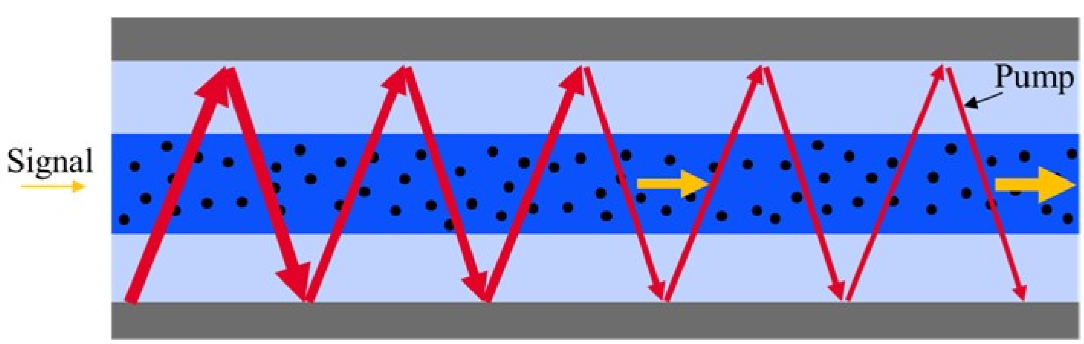

Figure 1.1. Double clad fiber geometry.

results in spontaneous Brillouin scattering where acoustic phonons are spontaneously excited. These acoustic phonons enable the transfer energy to a backward propagating Stokes mode due to the acousto-optic effect. As the pump power increases, the forward and backward optical modes constructively and destructively interfere with each other, which at sufficiently high powers can lead to a resonant acoustic wave that enables significant power transfer between forward and backward propagating optical modes due to electrostriction. This will often cause a drop in output power with large, reflected pulses that are directed toward the pump or laser source but can also cause physical damage to the fiber in extreme cases. Figure 1.2 shows the modes used to describe the behavior of BI. The Stokes mode has a negative wavenumber, the fundamental (pump) mode has a positive wavenumber, and the acoustic mode varies longitudinally along the fiber.

Typical concepts for suppressing BI involve either reducing the overlap between optical and acoustic modes, disrupting the resonant acoustic mode, and broadening the laser linewidth to that greater than the Brillouin linewidth. Reducing the overlap between acoustic and optical modes requires specially designed fibers such as photonic crystal fibers (PCFs). Disrupting the density fluctuations in the material has been done experimentally by applying thermal and mechanical stress gradients along the fiber. Of the concepts previously discussed, broadening the laser linewidth does not require any modifications to the amplifier design since broadening the laser linewidth may be done with phase modulation [16–19]. Power threshold for BI is commonly defined as when the reflected Stokes power reaches 1% of the pump power [16–19].

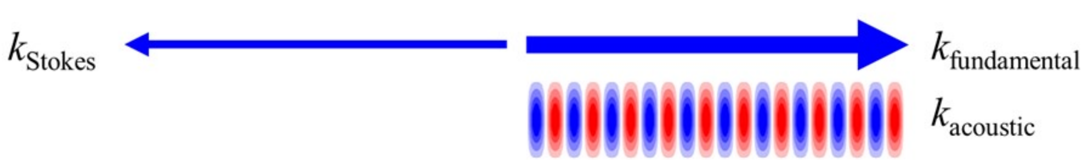

Figure 1.2. Schematic of modes for BI.

When light passes through an optical fiber, each component in the spectrum will have a Brillouin gain linewidth associated with it, which is typically redshifted by tens of GHz [20–22]. Phase modulation techniques such as white noise [17, 23], sinusoidal [17], chirped seed [24], piecewise parabolic phase [19], and pseudo-random bitstream (PRBS) [17,18,23,25,26] have all been used in experiment and simulation to suppress BI. Phase modulation suppresses BI by broadening the effective Brillouin linewidth, lowering the peak Brillouin gain, and equalizing the gain across the Brillouin gain spectra.

1.3 Transverse mode instability

The transverse mode instability (TMI) is another nonlinear effect that limits the output power of HEL fiber amplifiers. First documented in 2010 [15], TMI is observed as the sudden onset in an unstable transverse output mode profile. What starts as a near Gaussian beam quickly devolves into a time dependent multimode output profile. TMI significantly reduces the output beam quality and increases the difficulty of successful beam combining for power scaling applications. TMI's root comes from quantum defect heating. TMI starts from the constructive and destructive interference between the forward optical fundamental mode and forward optical higher-order mode (HOM) that is offset by the fundamental mode by around a kHz. The light interference pattern that develops creates a temperature grating along the longitudinal direction of the fiber because of the thermo-optic effect. The temperature grating causes a refractive index grating that enables power transfer between the fundamental mode and HOM. In low power cases there is oscillatory power transfer between the fundamental mode and HOM but increasing operating power may lead to chaos where nearly all of the power in the fundamental mode transfers to HOMs with no steady state reached. Figure 1.3 shows a schematic of the modes present when considering TMI. Both the fundamental and HOM travel in the forward direction of the fiber. For TMI, only the transverse temperature profile is considered.

Suppressing TMI can be divided between intrinsic and extrinsic methods. Intrinsic suppression techniques involve modifying fiber design such as reducing the spatial overlap between the gain profile and HOMs [27], reducing the spatial overlap between the fundamental mode and HOMs [27], minimizing the distance between the shift in total intensity when HOMs are present [27], and designing the fiber such that HOMs are not supported in some region [27]. Extrinsic techniques refer to suppression of TMI without modifying the fiber design such as inducing bend loss [28, 29] for the HOM and optimizing the difference between pump and signal wavelengths [2, 30, 31].

1.4 Other nonlinear effects

While BI and TMI are the lowest order nonlinear effects exhibited in fiber amplifiers, other nonlinear effects may arise, such as stimulated Raman scattering (SRS) and self-focusing [14, 32]. Like SBS, SRS can be induced by the interaction of vibrations in the crystal lattice of the waveguide. When these vibrations correspond to optical phonons, SRS arises, whereas when the vibrations involve acoustic phonons SBS is manifested. The frequency shifts are also different for SRS and SBS, the former is usually on the scale of THz and the latter on the scale of GHz. Self-focusing is another unique nonlinear effect in that it does not depend on the light intensity like

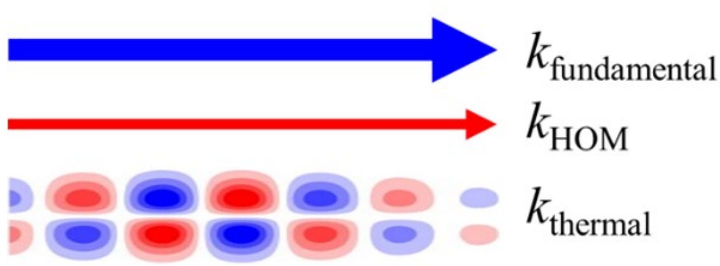

Figure 1.3. Schematic of modes for TMI.

BI and TMI do, but rather on the total power [32]. Therefore, changing the mode diameter alone will not suppress self-focusing. On the other hand, self-focusing has a power threshold a few orders of magnitude larger than that of BI or TMI, which in the case for silica fibers is around 5 MW [32].

1.5 Organization of dissertation

The rest of the dissertation is organized as follows: Chapter two describes mode coupling in simple one-dimensional slab waveguides for both index guiding and anti-resonant structures. The avoided crossings in effective index for the modes are also studied. The coupled-mode equations that describe the interaction in simple slab waveguide structures are expanded to understand and compare avoided crossing behavior with that of the more complicated in design hollow-core fibers. Chapter three reviews the current theoretical models used to simulate the transverse mode instability based on coupled-mode theory. The full model and phase-matched model are compared. TMI is computationally intensive to model on the account that the entire fiber must be discretized in three dimensions. The phase-matched model allows for a much coarser longitudinal discretization and leads to a large computational speedup with no loss of accuracy. Chapter four describes theoretical modeling and suppression of the Brillouin instability using phase modulation. Chapter five describes a multi-time-scale approach to simultaneously model the Brillouin and transverse mode instabilities in a single simulation. Fiber geometry is optimized to achieve the largest output power at the pump power threshold. A summary is then given in Chapter six. We also discuss future prospects for mitigation and modeling of nonlinear effects that limit operating power in fiber amplifiers.

CHAPTER TWO

Avoided Crossings in Slab Waveguides

This chapter published as part of [33]: J. T. Young, C. Wei, J. Hu, and C. R. Menyuk, "Mode coupling at the avoided crossings in slab waveguides with comparison to optical fibers: tutorial" J. Opt. Soc. Am. B **38**(12), F104–F114 (2021).

In this chapter, we describe the avoided crossings in slab waveguides and compare the behavior to that of optical fibers. Avoided crossings are important in many waveguides and resonators. That is particularly the case in modern-day solid-core and air-core optical fibers that often have a complex geometry. The study of the mode coupling at the avoided crossings often leads to a complicated analysis. In this tutorial, we aim to explain the basic features of avoided crossings in a simple slab waveguide structure so that the modes can be found analytically, with simple sinusoidal and exponential forms. We first review coupled-mode theory for the guided mode in a slab waveguide, which has a higher index in the core. We study the effective index of the guided true mode for the five-layer slab waveguide including two core layers with a higher index compared to the index in the three cladding layers. Then, we study the same structure by using the overlap between approximate modes that are confined in the two individual core slabs. When the two individual core slabs are not near each other, the avoided crossing using the true modes within the two-slab waveguide agrees well with the results using the overlap between the two approximate modes. We also study coupled-mode theory and avoided crossings for leaky modes in an antiresonant slab waveguide. We obtain good agreement between the results using the true leaky mode and the results using the overlap between the approximate modes. We then discuss examples of avoided crossings in solid-core and air-core optical fibers. We describe the similarities and differences between the optical fibers and the simple slab waveguides that we have analyzed in detail.

2.1 Introduction

2.1.1 Avoided crossings in different devices

Avoided crossings between modes appear in many optical waveguides and resonators. They often occur between modes in a single waveguide or resonator, or due to coupling between modes in different waveguides or resonators that are in close proximity. The study of the mode coupling in hollow-core fibers often leads to a complicated analysis, because the modes experiencing avoided crossings in hollow-core fibers are leaky modes [34], which requires a computational solution due to the complex structures. Leaky modes and avoided crossings have long been studied in optical systems. While the theory of avoided crossing is well understood in the case of guided modes in optical waveguides, there has been little or no study of avoided crossings in optical waveguides that have leaky modes and whose structure is sufficiently simple for the modes to be derived analytically. In this tutorial, we focus on one-dimensional slab waveguides to study the avoided crossings for leaky modes in a simple context. The formulation of coupled-mode analysis has been presented in Ref. [35]. This formulation of coupled-mode theory applies to guided modes, and it cannot be directly applied to leaky modes. We describe here the revision of the coupled-mode equations that is necessary to describe leaky modes in one-dimensional slab waveguides.

Optical waveguides can be divided into two categories: one-dimensional waveguides and two-dimensional waveguides. The slab waveguides in one-dimensional structures appear in a wide range of applications, including photonic-integrated circuits (PICs). PICs may make possible high-throughput and low-power signal processors that overcome the limits of conventional electronic digital signal processing technology [36]. One-dimensional PIC structures have been studied, but no detailed study of avoided crossings has been carried out using slab waveguides. Avoided crossings can play an important role in the mode coupling in silicon PICs [37]. Recently, hollow-core optical fibers that are two-dimensional waveguides have been widely studied and can have low loss values around 0.5 dB/km [38–44]. These fibers can be designed so that most of the power is transmitted through an air core with low loss and low nonlinearity. As a result, hollow-core fibers are useful for a variety of applications, such as high-power delivery [45], biological applications [46,47], gas lasers [48–50], and supercontinuum generations [51]. In air-core optical fibers, such as negative curvature fibers, the fundamental core mode couples strongly to additional core and cladding modes in certain conditions. The analysis of avoided crossings using antiresonant glass partitions can provide insight into the mode coupling and the loss of the core mode in negative curvature fibers [52–54]. If the glass partition thickness corresponds to antiresonance in the slab waveguide, then the fundamental mode loss is low. In this case, the width of the avoided crossing, which is defined as the minimum difference in effective indices of the coupled modes, is small due to weak coupling. When the glass thickness corresponds to resonance, there is a larger avoided crossing width, and the fundamental mode experiences a higher loss. In addition, ring resonators have been successfully used for filters, biosensing, and frequency comb generation [55]. Mode coupling and avoided crossings are important in understanding the efficiency of ring resonators.

2.1.2 Brief history on the study of avoided crossings

Avoided crossings, also known as anticrossings, were first described in quantum mechanics by Neumann and Wigner who showed that energy levels of electronic states cannot cross [56]. Avoided crossings have also been used to explain the non-intersection of electron energy states for different molecules [57, 58]. The first discussion of avoided crossings in optics was made in 1963 by Eck et al. in their study of fluorescence [59]. In 1979, Marcuse and Kaminow observed avoided crossings of transverse electric (TE) and transverse magnetic (TM) modes within a thin-film slab waveguide [60]. The first study of avoided crossings in optical fibers was carried out in 1988 in a fiber-optic ring resonator [61]. More recently, avoided crossings have become important in understanding the coupling between the core and cladding modes in solid-core photonic crystal fibers [62], photonic bandgap fibers (PBGFs) [63–67], negative curvature fibers [52–54], and kagome fibers [68]. In high power laser systems using a photonic crystal fiber, it was later found that the avoided crossing induced by the pump profile, bending, or index depression may lead to unwanted deformations of the output beam [62]. On the other hand, avoided crossings have been used for optical filters [69], refractive index sensors [70–72], temperature sensors [73], and higher-order mode (HOM) suppression [52, 74, 75].

The rest of this tutorial is organized as follows: in Sec. 2.2, we review the equations for the coupled-mode theory for the guided mode in a high-index core slab waveguide. Section 2.3 describes an example of a guided mode in a slab waveguide, where the index of core, n_g, is larger than the index of cladding, n_c. We compare the computational results, computed using the finite difference method (FDM), to the results from coupled-mode theory. Section 2.4 describes the derivation of the coupled-mode theory for leaky modes in an antiresonant slab waveguide. Section 2.5 shows an example of mode coupling in an antiresonant slab waveguide. We again compare the computational results to the results from coupled-mode theory. In Sec. 2.6, we discuss how the insights that we have gained can be applied to more complex geometries, and we conclude in Sec. 2.7.

2.2 Coupled-mode theory for guided modes in a slab waveguide

We start with a description of the guided modes in a one-dimensional five-layer slab waveguide with two core layers and three cladding layers, shown in Fig. 2.1(a). The refractive index of the two guiding layers is n_g and the refractive index of the surrounding layers is n_c. To have guided modes, we must have $n_g > n_c$. The thick-

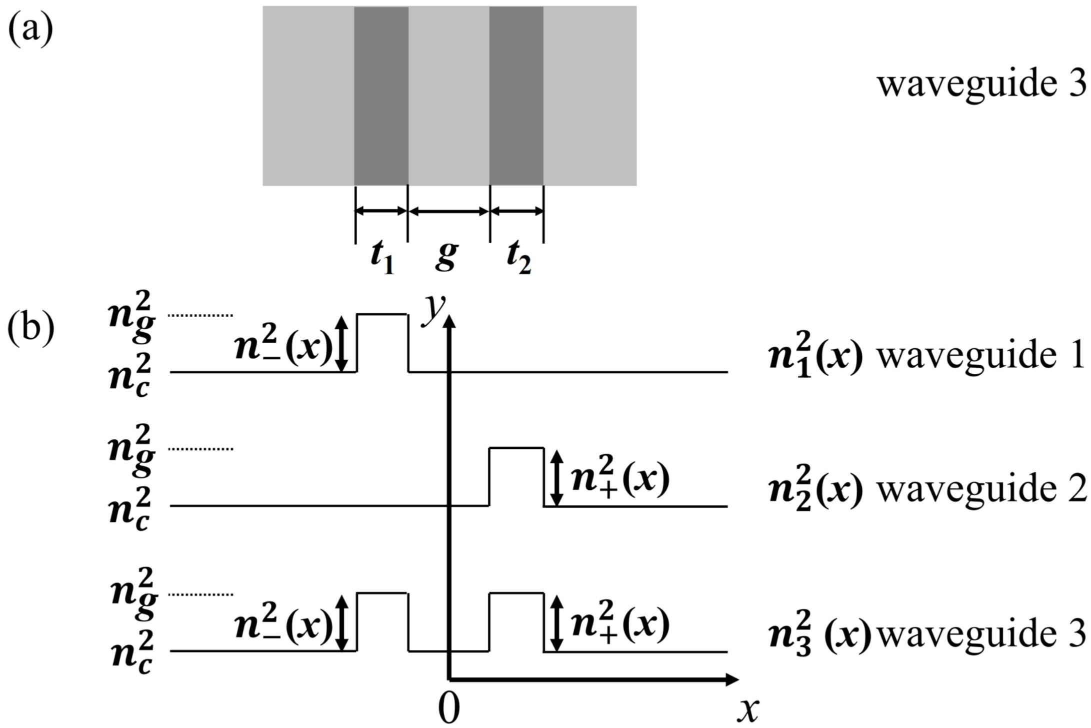

Figure 2.1: (a) Illustration of the two-core index-guided waveguide structure. (b) Illustration of the refractive index profiles for waveguides 1, 2, and 3. [Reprinted/Adapted] with permission from [33] © Optica Publishing Group.

nesses of the guiding layers are t_1 and t_2. In coupled-mode theory, we decouple the two guiding layers by considering the modes in two waveguides each of which has one guiding layer, corresponding to one of the two guiding layers in the original waveguide, labeled waveguide 3 in Fig 2.1(b).

The refractive index distributions for waveguides 1, 2, and 3 are denoted by $n_1(x)$, $n_2(x)$, and $n_3(x)$, respectively, and may be written as

$$\begin{aligned} n_1^2(x) &= n_c^2 + n_-^2(x), \\ n_2^2(x) &= n_c^2 + n_+^2(x), \\ n_3^2(x) &= n_c^2 + n_-^2(x) + n_+^2(x), \end{aligned} \tag{2.1}$$

where $n_+^2(x)$ and $n_-^2(x)$ are defined as

$$
n_+^2(x) = \begin{cases} n_g^2 - n_c^2 & g/2 < x < g/2 + t_2 \\ 0 & \text{otherwise} \end{cases},
$$
$$
n_-^2(x) = \begin{cases} n_g^2 - n_c^2 & -t_1 - g/2 < x < -g/2 \\ 0 & \text{otherwise} \end{cases}. \tag{2.2}
$$

We will focus on TE modes. In this case, the field component E_y obeys the Helmholtz equation,

$$
\frac{\partial^2 E_y}{\partial z^2} + \frac{\partial^2 E_y}{\partial x^2} + \frac{n^2(x)\omega_0^2}{c^2} E_y = 0. \tag{2.3}
$$

If we consider one mode in waveguide 1 with a normalized transverse profile $\psi_1(x)$ and wavenumber β_1 and one mode in waveguide 2 with normalized transverse profile $\psi_2(x)$ and wavenumber β_2, then there is a propagating electric field in waveguide 3 that may be written approximately as

$$
E_y(x, z, t) = A_1(z)\psi_1(x)\exp[i(\omega_0 t - \beta_1 z)] + A_2(z)\psi_2(x)\exp[i(\omega_0 t - \beta_2 z)]. \tag{2.4}
$$

The transverse mode profiles $\psi_1(x)$ and $\psi_2(x)$ are normalized so that $\int_{-\infty}^{\infty} |\psi_{1,2}|^2 dx = 1$. The parameters $A_1(z)$ and $A_2(z)$ are slowly varying amplitudes for waveguides 1 and 2 respectively, so that

$$
\begin{aligned}
-\beta_1^2\psi_1 + \frac{\partial^2 \psi_1}{\partial x^2} + \frac{n_1^2(x)\omega_0^2}{c^2}\psi_1 &= 0, \\
-\beta_2^2\psi_2 + \frac{\partial^2 \psi_2}{\partial x^2} + \frac{n_2^2(x)\omega_0^2}{c^2}\psi_2 &= 0.
\end{aligned} \tag{2.5}
$$

Substituting Eq. (2.4) into Eq. (2.3) and using Eq. (2.5) with the slowly varying envelope approximation so that, $|\partial^2 A_{1,2}/\partial z^2| \ll \beta_{1,2}|\partial A_{1,2}/\partial z|$, we obtain

$$
\begin{aligned}
-2i\beta_1\psi_1\frac{\partial A_1}{\partial z}\exp(-i\beta_1 z) - 2i\beta_2\psi_2\frac{\partial A_2}{\partial z}\exp(-i\beta_2 z) \\
+\frac{n_+^2(x)\omega_0^2}{c^2}A_1\psi_1\exp(-i\beta_1 z) + \frac{n_-^2(x)\omega_0^2}{c^2}A_2\psi_2\exp(-i\beta_2 z) = 0.
\end{aligned}
\tag{2.6}
$$

We now multiply the above equation by $\psi_1^*(x)$ and $\psi_2^*(x)$, integrate over x, and use the normalized fields, yielding two equations,

$$
\begin{aligned}
\frac{\partial A_1}{\partial z} + \frac{i\kappa_{12}}{2\beta_1}A_2\exp[i(\beta_1-\beta_2)z] = 0, \\
\frac{\partial A_2}{\partial z} + \frac{i\kappa_{21}}{2\beta_2}A_1\exp[-i(\beta_1-\beta_2)z] = 0,
\end{aligned}
\tag{2.7}
$$

where

$$
\begin{aligned}
\kappa_{11} &= \frac{\omega_0^2}{c^2}\int_{-\infty}^{\infty} n_+^2(x)|\psi_1(x)|^2 dx, \\
\kappa_{12} &= \frac{\omega_0^2}{c^2}\int_{-\infty}^{\infty} n_-^2(x)\psi_1^*(x)\psi_2(x) dx, \\
\kappa_{21} &= \frac{\omega_0^2}{c^2}\int_{-\infty}^{\infty} n_+^2(x)\psi_1(x)\psi_2^*(x) dx, \\
\kappa_{22} &= \frac{\omega_0^2}{c^2}\int_{-\infty}^{\infty} n_-^2(x)|\psi_2(x)|^2 dx.
\end{aligned}
\tag{2.8}
$$

In the derivation, we assume that $\psi_1(x)$ and $\psi_2(x)$ are well confined in the individual waveguides, so that $\int_{-\infty}^{\infty}\psi_1^*(x)\psi_2(x)dx \ll 1$, $\kappa_{11} \ll \kappa_{12}$, and $\kappa_{22} \ll \kappa_{21}$. The amplitudes in the individual waveguides can be written as

$$
\begin{aligned}
A_1 &= R_1\exp[i\Delta\beta z/2], \\
A_2 &= R_2\exp[-i\Delta\beta z/2],
\end{aligned}
\tag{2.9}
$$

where $\Delta\beta = \beta_1 - \beta_2$, while R_1 and R_2 are slowly varying quantities. Using Eq. (2.9), we can rewrite Eq. (2.7) in matrix form as

$$
\frac{d\mathbf{R}}{dz} = i\lambda\mathbf{R} = -i\begin{bmatrix} \Delta\beta/2 & \kappa_{12}/(2\beta_1) \\ \kappa_{21}/(2\beta_2) & -\Delta\beta/2 \end{bmatrix}\mathbf{R}, \tag{2.10}
$$

where **R** can be written as

$$\mathbf{R} = \begin{bmatrix} V_1 \\ V_2 \end{bmatrix} e^{i\lambda z} = \mathbf{V}e^{i\lambda z}. \tag{2.11}$$

Equation (2.10) is a standard matrix algebra eigenvalue problem, where **V** is the eigenvector. The condition for a nontrivial solution for **V** is that the determinant of the matrix in Eq. (2.10) must vanish. We then find

$$-\frac{(\Delta\beta)^2}{4} + \lambda^2 - \frac{\kappa_{12}\kappa_{21}}{4\beta_1\beta_2} = 0, \tag{2.12}$$

which yields the solution $\lambda_{1,2}$, where

$$\lambda_{1,2} = \mp\frac{1}{2}\left[(\Delta\beta)^2 + \frac{\kappa_{12}\kappa_{21}}{\beta_1\beta_2}\right]^{1/2}. \tag{2.13}$$

According to Eq. (2.11), the corresponding normalized eigenvectors are

$$\begin{bmatrix} V_1 \\ V_2 \end{bmatrix} = \begin{bmatrix} -\kappa_{12} \\ \beta_1(\Delta\beta + 2\lambda) \end{bmatrix} / \{\kappa_{12}^2 + [\beta_1(\Delta\beta + 2\lambda)]^2\}^{1/2}. \tag{2.14}$$

When $\Delta\beta \gg \kappa_{12}, \kappa_{21}$, we find that $\lambda_{1,2} = \mp\Delta\beta/2$, and the solutions for **V** are $(0, 1)$ or $(1, 0)$ which means the two solutions are entirely in waveguide 2 or waveguide 1. When $\Delta\beta = 0$, we find that $\beta_1 = \beta_2$ and $\kappa_{12} = \kappa_{21}$ yielding the solutions of $(1/2, 1/2)$ or $(-1/2, 1/2)$ for **V**; hence, the solution in field intensity is nearly equal in both waveguides.

Using Eqs. (2.4), (2.9), and (2.11), the field in waveguide 3 may be written as

$$E_y(x, z, t) = V_1\psi_1(x)\exp[i(\omega_0 t - \beta_1' z)] + V_2\psi_2(x)\exp[i(\omega_0 t - \beta_2' z)], \tag{2.15}$$

with

$$\begin{aligned} n_{\text{eff1}} &= \beta_1'/k_0 = \frac{1}{k_0}\left(\frac{\beta_1 + \beta_2}{2} - \lambda_1\right), \\ n_{\text{eff2}} &= \beta_2'/k_0 = \frac{1}{k_0}\left(\frac{\beta_1 + \beta_2}{2} - \lambda_2\right), \end{aligned} \tag{2.16}$$

where k_0 is the wavenumber, and $n_{\text{eff}1,2} = \beta'_{1,2}/k_0$ are the effective indices of the two modes that we are considering. We now obtain the width of the avoided crossing when $\beta_1 = \beta_2$ and $\Delta\beta = 0$,

$$\delta = |n_{\text{eff}1} - n_{\text{eff}2}| = \frac{1}{k_0}\left(\frac{\kappa_{12}\kappa_{21}}{\beta_1\beta_2}\right)^{1/2}, \tag{2.17}$$

which we define as the minimum difference in effective indices for the two modes in waveguide 3. The coupling coefficients κ_{12} and κ_{21} are given in terms of the approximate modes according to Eq. (2.8). We have thus found that the refractive index of the true modes and the avoided crossing in waveguide 3 can be approximately obtained using the refractive index and mode profiles of the modes of waveguides 1 and 2.

2.3 *Example of mode coupling in a slab waveguide with guided modes*

In this section, we will use the equations from Sec. 2.2 to study the mode coupling between the fundamental modes in the five-layer slab waveguide with two core layers and three cladding layers (waveguide 3). We consider an example with $n_g = 1.45$ and $n_c = 0.96 n_g = 1.39$ that was previously studied [34]. The thickness of the first glass layer, t_1, is fixed at 5 μm. The wavelength is 1 μm. The gap between glass slabs, g, is fixed at 2 μm. We increase the thickness of the second glass layer, t_2, from 4 μm to 12 μm so that the avoided crossing can be observed. In Fig. 2.2(a), the solid blue curves show the effective indices of the modes in the two-layer slab waveguide 3, shown in Fig. 2.1. The dotted green curve shows the effective index for the fundamental mode of waveguide 1, which has a constant value of 1.44742. The dotted orange curves show the effective indices for the fundamental mode and the first high-order mode of waveguide 2, which has a changing thickness, t_2. We use the FDM to calculate the computational modes and the effective indices.

In Fig. 2.2(a), the dotted curves for the effective index of the two single-layer waveguides overlap with the solid blue curves for the effective index of the two-layer waveguide, except within an avoided crossing region. An avoided crossing occurs when

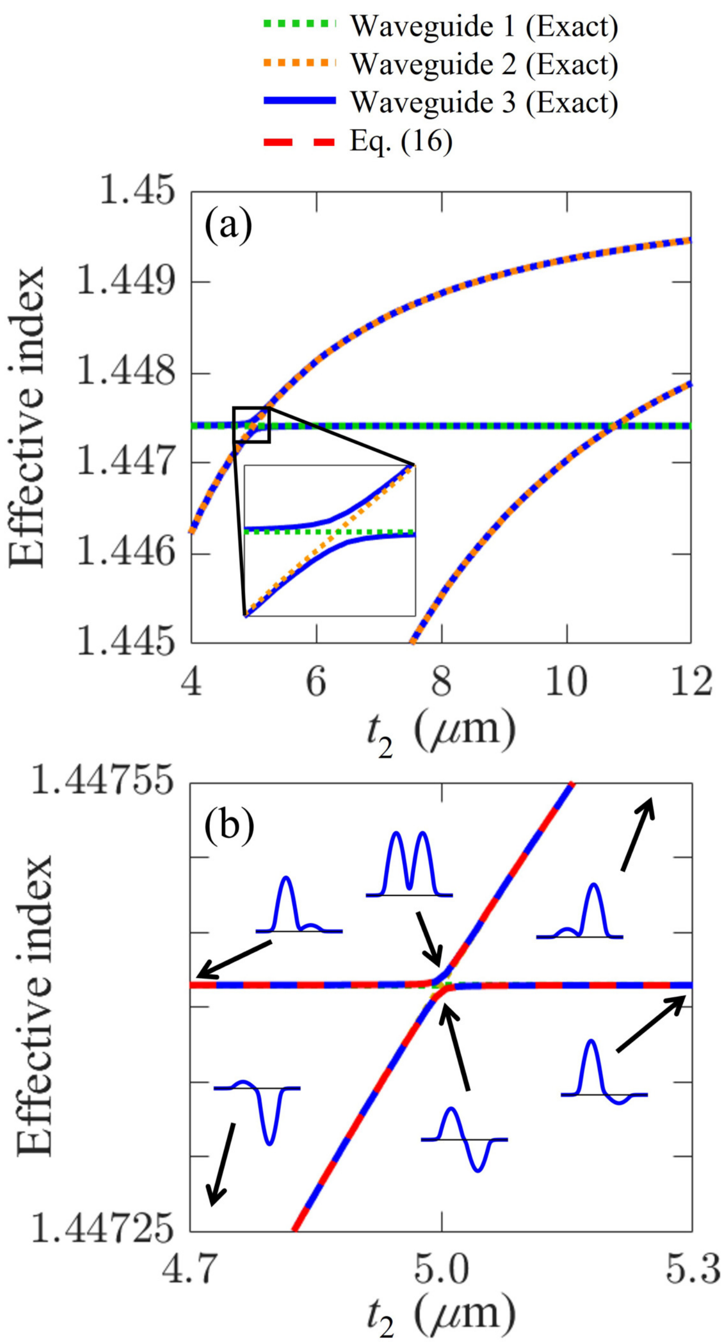

Figure 2.2: (a) Effective index for the fundamental core mode in waveguide 1 and 2 (dashed curves) and waveguide 3 (solid curve) as a function of t_2. Inset in (a) shows a magnified plot so that the avoided crossing may be easily seen. (b) Magnified plot in Fig. 2.2(a) around the first avoided crossing at $t_2 = 5$ μm. Insets show mode profiles in the waveguide 3. The red dashed curve shows the effective index obtained from Eq. (2.16). [Reprinted/Adapted] with permission from [33] © Optica Publishing Group.

t_2 is 5.0 μm or 10.6 μm, and the modes in the two high-index glass layers couple. To show the avoided crossing clearly, the inset in Fig. 2.2(a) shows a magnified plot near the first avoided crossing so that the differences in the effective indices may be easily distinguished. The insets in Fig. 2.2(b) show the mode profiles in waveguide 3 for different t_2 thicknesses equal to 4.7, 5.0, and 5.3 μm near the first avoided crossing. When $t_2 < 5$ μm, the modes are well confined in one of the glass layers. When $t_2 = 5$ μm, where the avoided crossing occurs, the two modes become a hybrid even or odd mode, which is located in both of the two high-index layers. When $t_2 > 5$ μm, the coupling decreases and the two modes are again primarily located in one of the two glass waveguides. If we follow the modes along either of the continuous branches of the effective index, we see that the mode switched from one waveguide to the other. This mode-swapping is a characteristic feature of avoided crossings. We now use Eq. (2.17) from coupled-mode theory to study the avoided crossing, as shown in the dashed red curves in Fig. 2.2(b). We found that the dashed red curves using Eq. (2.17) agree exactly with a computational FDM calculation of the modes in waveguide 3. Hence, the overlap of approximate modes confined in waveguides 1 and 2 via coupled-mode theory can account for the avoided crossing and makes it possible to approximate the true modes in waveguide 3.

We now set $t_1 = t_2 = 5$ μm and vary the gap, g, between the core layers. We plot the difference in the effective indices during the avoided crossing, δ, between the fundamental mode in core layer 1 and the fundamental mode in core layer 2, in Fig. 2.3. The top right inset in Fig. 2.3 gives an illustration of δ, showing the minimum difference between effective indices of the modes in waveguide 3. The bottom left inset shows a magnified plot of δ for small gap sizes so that differences between the computational result and the result from coupled-mode theory may be distinguished. The parameter, δ, can be used to quantify the width of the avoided crossing and the strength of coupling between modes. A larger avoided crossing corresponds to a

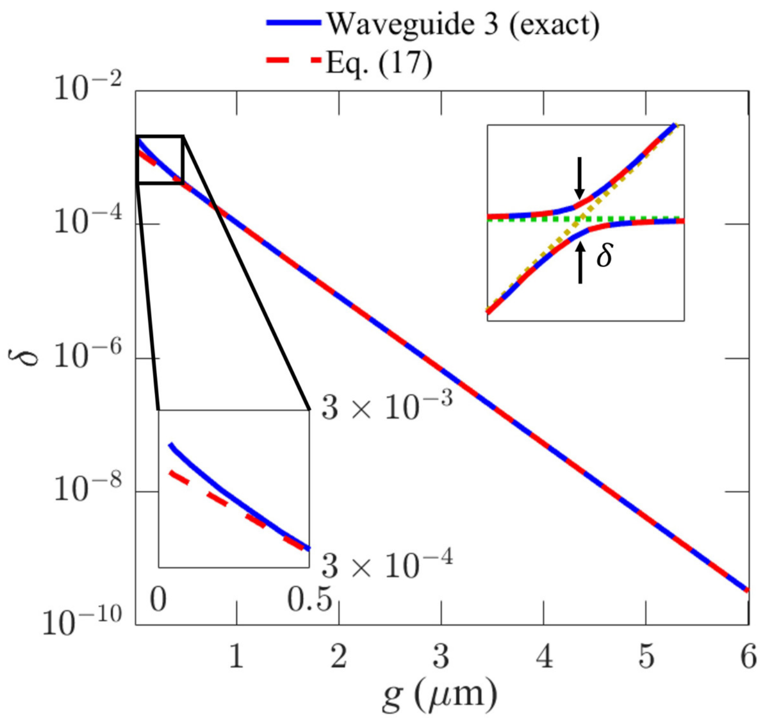

Figure 2.3: Avoided crossing width calculated using the minimum difference in the effective index, δ, vs. the gap separation in waveguide 3. The solid blue curve shows the computational result, and the dashed red curve shows the approximate result from coupled-mode theory [Eq. (2.17)]. The top right inset shows a magnified plot of Fig. 2.2(b) to illustrate the avoided crossing at when $g = 2$ μm and $t_1 = t_2 = 5$ μm. The bottom left inset shows a magnified plot when g is between 0.04 and 0.5 μm. [Reprinted/Adapted] with permission from [33] © Optica Publishing Group.

stronger coupling. The value of δ decreases exponentially as g increases. As the gap between adjacent core layers increases, the overlap between modes decreases, leading to the decrease of the avoided crossing width. For very small gaps, the agreement between the computational result and the approximate result from Eq. (2.17) breaks down.

2.4 Coupled-mode theory in an antiresonant slab waveguide

In an antiresonant slab waveguide, the antiresonance condition is needed to guide the mode in the central air slab [76]. To satisfy the antiresonance condition, the phase difference in the directly transmitted transverse wave vector and transverse wave vector with an additional two reflections must be an odd multiple of π. The glass thickness required for the antiresonance condition is given by [76–78]

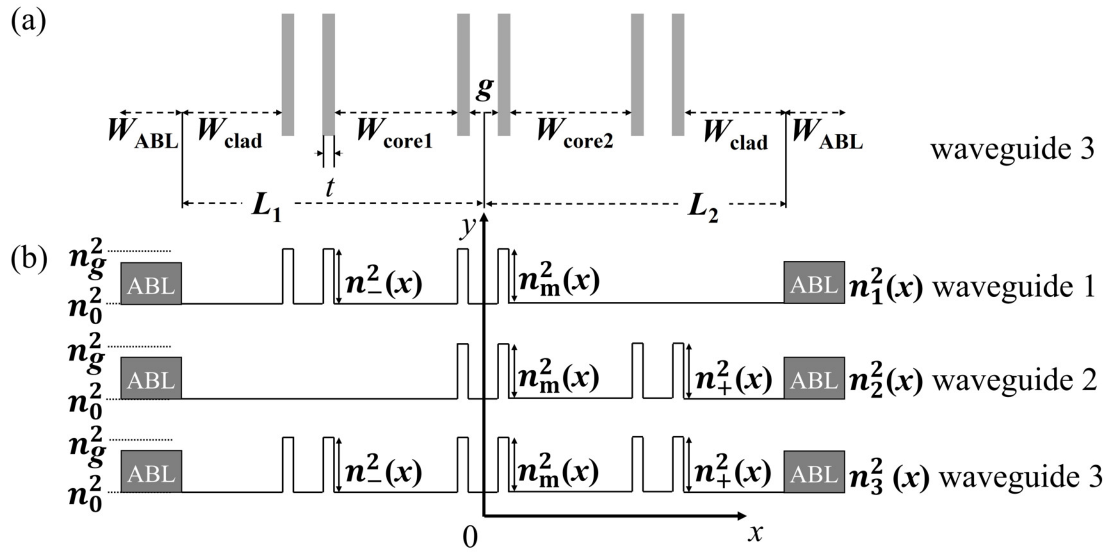

Figure 2.4: (a) Illustration of the two-core antiresonant slab waveguide. (b) Definitions of refractive index profiles. [Reprinted/Adapted] with permission from [33] © Optica Publishing Group.

$$t = (m - 0.5)\lambda/[2(n_g^2 - n_0^2)^{1/2}], \tag{2.18}$$

where m is a positive integer. To study coupled-mode theory in a leaky, antiresonant slab waveguide, we consider the slab waveguide that we show in Fig. 2.4(a), which has two large air slabs surrounded by glass-air-glass layers. We use two closely-spaced higher-index glass layers (a double glass partition) as a barrier between the mode-confining air slabs, denoted as $W_{\mathrm{core1,2}}$, to reduce the mode content between cores 1 and 2. In negative curvature fibers [77], center modes are naturally separated from the cladding air modes. The negative curvature in the glass layer strongly confines the fundamental mode so that it has low loss. To achieve a similar confinement in the single slab structures that we are considering, we have found that it is necessary to use the double glass partitions that we show in Fig. 2.4.

Antiresonant waveguides are waveguides in which a lower index or air core is surrounded by higher-index or glass barriers, which is then surrounded in turn by more lower-index or air regions [34]. These can then be surrounded by more barriers, leading to more complex structures. Slab waveguides with this structure are antiresonant reflecting optical waveguides (ARROW) [76, 79], and if the outside cladding layers are lower-index or air, then there are no completely confined modes, and the modes of the structure will all be leaky [34]. However, the modes can be well-confined in the core with low leakage if an antiresonant condition is obeyed [76, 77].

Similar to the five-layer slab waveguide simulations that appeared in Sec. 2.2, three structures are used to understand the coupling of adjacent air-core layers. The refractive index distributions for the waveguides 1, 2, and 3 in Fig. 2.4(b) are given by $n_1(x)$, $n_2(x)$, and $n_3(x)$,

$$\begin{aligned} n_1^2(x) &= n_-^2(x) + n_m^2(x) + n_0^2, \\ n_2^2(x) &= n_+^2(x) + n_m^2(x) + n_0^2, \\ n_3^2(x) &= n_-^2(x) + n_+^2(x) + n_m^2(x) + n_0^2, \end{aligned} \tag{2.19}$$

where

$$\begin{aligned} n_+^2(x) &= \begin{cases} n_g^2 - n_0^2 & (t + g/2 + W_{\text{core2}}) < x < (2t + g/2 + W_{\text{core2}}) \\ n_g^2 - n_0^2 & (2t + 3g/2 + W_{\text{core2}}) < x < (3t + 3g/2 + W_{\text{core2}}) \\ 0 & \text{otherwise} \end{cases}, \\ n_-^2(x) &= \begin{cases} n_g^2 - n_0^2 & -(3t + 3g/2 + W_{\text{core1}}) < x < -(2t + 3g/2 + W_{\text{core1}}) \\ n_g^2 - n_0^2 & -(2t + g/2 + W_{\text{core1}}) < x < -(t + g/2 + W_{\text{core1}}) \\ 0 & \text{otherwise} \end{cases}, \\ n_m^2(x) &= \begin{cases} n_g^2 - n_0^2 & -(g/2 + t) < x < -g/2 \\ n_g^2 - n_0^2 & g/2 < x < g/2 + t \\ 0 & \text{otherwise} \end{cases}. \end{aligned} \tag{2.20}$$

The field component E_y once again obeys the Helmholtz equation, Eq. (2.3); however, all the modes are leaky [34]. Absorbing boundary layers (ABLs) must be used to calculate the propagation constants in leaky waveguides and the validity of this approach is described in detail in [34]. The field in the coupled structure with an index of $n_3(x)$ is approximated by Eq. (2.4). The transverse electric field distributions and propagation constants for the modes in waveguides 1 and 2 are denoted by $\psi_1(x)$, $\psi_2(x)$, β_1, and β_2, respectively. The transverse field distributions $\psi_1(x)$ and $\psi_2(x)$ are the solutions of the wave equation in the corresponding waveguide with the index distributions $n_1(x)$ and $n_2(x)$, which yields

$$\begin{aligned} -\beta_1^2\psi_1 + \frac{\partial^2\psi_1}{\partial x^2} + \frac{n_1^2(x)\omega_0^2}{c^2}\psi_1 = 0, \\ -\beta_2^2\psi_2 + \frac{\partial^2\psi_2}{\partial x^2} + \frac{n_2^2(x)\omega_0^2}{c^2}\psi_2 = 0. \end{aligned} \tag{2.21}$$

We normalize the transverse mode fields so that $\int_{-\infty}^{\infty} |\psi_{1,2}|^2 dx = 1$, which is possible once the absorbing layers are added and is feasible if the leakage power in the modes is small [34]. We carry out an analysis that is analogous to the analysis in Sec. 2.2, and we find

$$\begin{aligned} \frac{\partial A_1}{\partial z} + \frac{i\kappa_{11}A_1}{2\beta_1} + \frac{i\kappa_{12}}{2\beta_1}A_2\exp[i(\beta_1-\beta_2)z] = 0, \\ \frac{\partial A_2}{\partial z} + \frac{i\kappa_{22}A_2}{2\beta_2} + \frac{i\kappa_{21}}{2\beta_2}A_1\exp[-i(\beta_1-\beta_2)z] = 0, \end{aligned} \tag{2.22}$$

where

$$
\begin{aligned}
\kappa_{11} &= \frac{\kappa_{11}^{+} - I_{12}\kappa_{21}^{+}}{1-|I_{12}|^2}, \\
\kappa_{12} &= \frac{\kappa_{12}^{-} - I_{12}\kappa_{22}^{-}}{1-|I_{12}|^2}, \\
\kappa_{21} &= \frac{\kappa_{21}^{+} - I_{12}^{*}\kappa_{11}^{+}}{1-|I_{12}|^2}, \\
\kappa_{22} &= \frac{\kappa_{22}^{-} - I_{12}^{*}\kappa_{12}^{-}}{1-|I_{12}|^2}, \\
\kappa_{11}^{+} &= \frac{\omega_0^2}{c^2}\int_{-\infty}^{\infty} n_{+}^2(x)|\psi_1(x)|^2 dx, \\
\kappa_{12}^{-} &= \frac{\omega_0^2}{c^2}\int_{-\infty}^{\infty} n_{-}^2(x)\psi_1^{*}(x)\psi_2(x) dx, \\
\kappa_{21}^{+} &= \frac{\omega_0^2}{c^2}\int_{-\infty}^{\infty} n_{+}^2(x)\psi_1(x)\psi_2^{*}(x) dx, \\
\kappa_{22}^{-} &= \frac{\omega_0^2}{c^2}\int_{-\infty}^{\infty} n_{-}^2(x)|\psi_2(x)|^2 dx, \\
I_{12} &= \int_{-\infty}^{\infty} \psi_1^{*}(x)\psi_2(x) dx.
\end{aligned}
\tag{2.23}
$$

We note that I_{12} may not be negligible since there can be significant overlap within the two glass and air slabs that separate the air-core layers. We now introduce new variables $\tilde{A}_1$ and $\tilde{A}_2$ as

$$
\begin{aligned}
A_1 &= \tilde{A}_1 \exp\left(-\frac{i\kappa_{11}}{2\beta_1}z\right), \\
A_2 &= \tilde{A}_2 \exp\left(-\frac{i\kappa_{22}}{2\beta_2}z\right).
\end{aligned}
\tag{2.24}
$$

Equation (2.22) then becomes

$$
\begin{aligned}
\frac{\partial \tilde{A}_1}{\partial z} + \frac{i\kappa_{12}}{2\beta_1}\tilde{A}_2 \exp[i(\Delta\beta)z] = 0, \\
\frac{\partial \tilde{A}_2}{\partial z} + \frac{i\kappa_{21}}{2\beta_2}\tilde{A}_1 \exp[-i(\Delta\beta)z] = 0,
\end{aligned}
\tag{2.25}
$$

where $\Delta\beta = \beta_1 - \beta_2 + \frac{\kappa_{11}}{2\beta_1} - \frac{\kappa_{22}}{2\beta_2}$. The amplitudes in the individual waveguides can be written as

$$
\begin{aligned}
\tilde{A}_1 &= R_1 \exp(i\Delta\beta z/2), \\
\tilde{A}_2 &= R_2 \exp(-i\Delta\beta z/2),
\end{aligned}
\tag{2.26}
$$

where R_1 and R_2 are slowly vary quantities. Substituting Eq. (2.26) into Eq. (2.25), we obtain the same matrix form as Eq. (2.10),

$$\frac{d\mathbf{R}}{dz} = i\lambda\mathbf{R} = -i \begin{bmatrix} \Delta\beta/2 & \kappa_{12}/(2\beta_1) \\ \kappa_{21}/(2\beta_2) & -\Delta\beta/2 \end{bmatrix} \mathbf{R}, \tag{2.27}$$

where $\mathbf{R}$ can be written as, $e^{i\lambda z}[V_1 \;\; V_2]^{\mathrm{T}}$, and T represents the matrix transpose operator. We may use the same procedure that is described by Eqs. (2.10) $-$ (2.14) in Sec. 2.2 with a slightly changed β_1' and β_2'. The effective indices of the modes in waveguide 3 are given by

$$\begin{aligned} n_{\text{eff1}} &= \beta_1'/k_0 = \frac{1}{k_0}\left(\beta_1 + \frac{\kappa_{11}}{2\beta_1} - \frac{\Delta\beta}{2} - \lambda_1\right), \\ n_{\text{eff2}} &= \beta_2'/k_0 = \frac{1}{k_0}\left(\beta_2 + \frac{\kappa_{22}}{2\beta_2} + \frac{\Delta\beta}{2} - \lambda_2\right). \end{aligned} \tag{2.28}$$

Again, the width of the avoided crossing, which is defined as the minimum difference in effective indices for the modes in waveguide 3, is given by

$$\delta = |n_{\text{eff1}} - n_{\text{eff2}}| = \frac{1}{k_0}\left(\frac{\kappa_{12}\kappa_{21}}{\beta_1\beta_2}\right)^{1/2}, \tag{2.29}$$

which is the same as in Eq. (2.17), but with different expressions for κ_{12} and κ_{21} in Eq. (2.23). The refractive index of the modes and the avoided crossing in the multi-layer slab waveguide can then be derived using the refractive index and mode profiles of the approximate modes in the two single air-core antiresonant slab waveguides, just as we did with guided modes in Sec. 2.2.

2.5 Mode coupling in antiresonant slab waveguides

In this section, we will use the equations in Sec. 2.4 to study the mode coupling of the antiresonant slab waveguide in Fig. 2.4(a). According to the structures shown in Fig. 2.4, the thickness of the air-core layer in waveguide 1, W_{core1}, is fixed at 30 μm. The cladding thickness, W_{clad}, is fixed at 37 μm. The glass thickness, t, is fixed at 0.72 μm, which yields the antiresonance condition for a wavelength of 1 μm. The air gap, g, is set to 5 μm. An absorbing boundary condition was introduced in the simulation with a width of 150 μm. The index in the ABL is modeled as [34]

$$n(x) = n_0 \left[1 + i\left(\frac{|x| - L_{1,2}}{W_{\mathrm{ABL}}}\right)^2 s\right]^{1/2}, \tag{2.30}$$

where n_0 is the index of air, W_{ABL} is the ABL thickness, $L_{1,2}$ are the distances from the center to the beginning of the ABL as denoted in Fig. 2.4(a). We set $s = 6 \times 10^{-6}$ so that the mode field will decay as it reaches the edge of the simulation window. We increase W_{core2} from 20 μm to 70 μm so that the avoided crossings can be observed in waveguide 3. In Fig. 2.5(a), the effective indices for the modes in waveguide 1 and waveguide 2 are plotted by dotted green and orange curves, respectively. The effective indices for the modes in waveguide 3 are plotted by solid blue curves. Their effective indices cross with the effective index of waveguide 1 at 30 μm and 60 μm, respectively. The inset in Fig. 2.5(a) shows a magnified plot at the first avoided crossing so that differences in effective indices may be easily distinguished. This index matching explains the avoided crossing and coupling of the modes in waveguide 3 when W_{core2} is 30 μm or 60 μm. If W_{core2} further increases, more couplings will occur when W_{core2} is a multiple of W_{core1}, which corresponds to the coupling between the fundamental mode in the first air core and an HOM in the second air core in waveguide 3. Figure 2.5(b) shows a magnified plot of Fig. 2.5(a) so that the differences in mode profiles near the first avoided crossing may be illustrated. The insets show mode profiles when W_{core2} is 29.95 μm, 30 μm, or 30.05 μm. The solid blue curves in Fig. 2.5(b) show the mode indices in waveguide 3. The dashed red curves show the effective indices using Eq. (2.28). The two methods agree well. When $W_{\mathrm{core2}} < 30$ μm, the modes are well confined in one of the air-core layers. When $W_{\mathrm{core2}} = 30$ μm, where the avoided crossing occurs, the two modes couple with each other and become a hybrid even or odd mode, which is located in both air-cores. When $W_{\mathrm{core2}} > 30$ μm, the coupling disappears and the two modes change places between the two air layers.

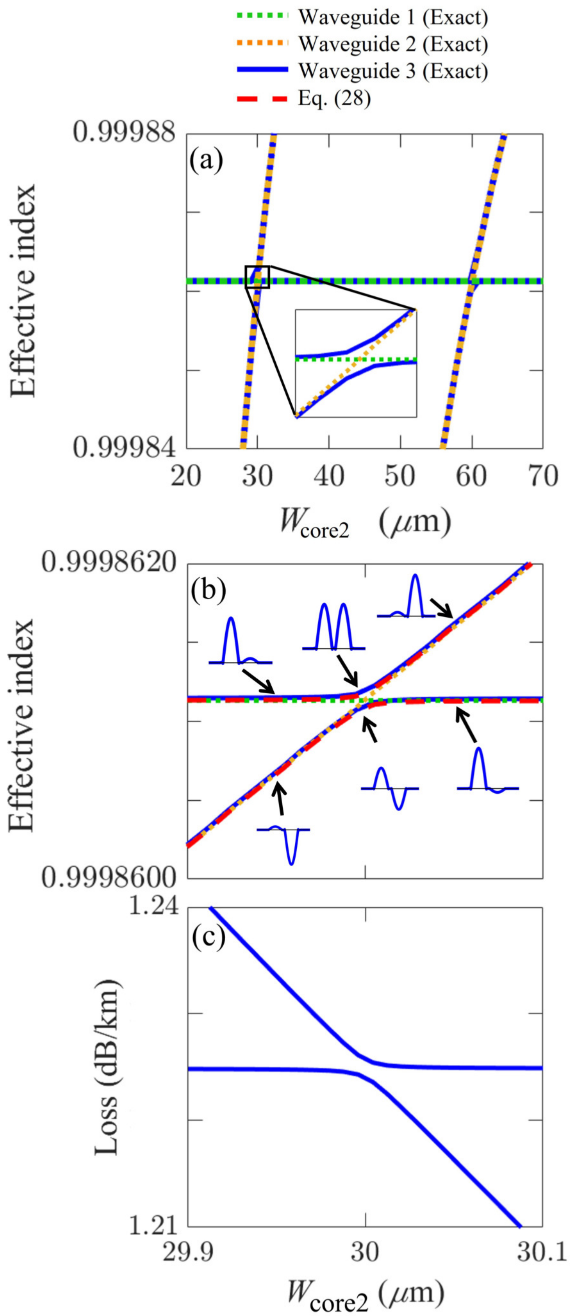

Figure 2.5: (a) Effective index for the fundamental core mode in waveguide 1 and 2 (dotted curves). Effective indices for the two fundamental core modes in waveguide 3 (solid curves). (b) Magnified plot in Fig. 2.5(a) around the first avoided crossing at $W_{\mathrm{core2}} = 30\ \mu$m. Insets show the mode in the waveguide 3 around the avoided crossing with different W_{core2}. The dashed red curves show results using Eq. (2.28). (c) Leakage loss of the hybrid modes in waveguide 3 at the first avoided crossing. [Reprinted/Adapted] with permission from [33] © Optica Publishing Group.

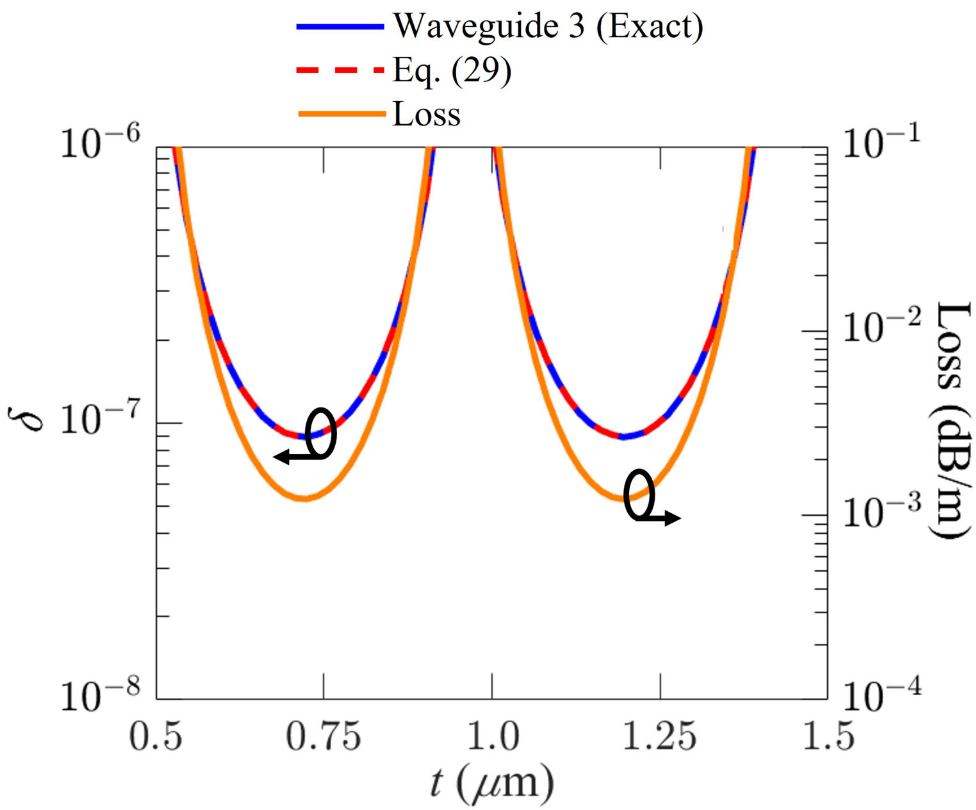

Figure 2.6: Width of the avoided crossing and loss at the avoided crossing as a function of the glass thickness with $g = 2$ μm and $W_{\text{core1}} = W_{\text{core2}} = 30$ μm. [Reprinted/Adapted] with permission from [33] © Optica Publishing Group.

Figure 2.5(c) shows that the leakage loss curves calculated using the FDM for the modes in waveguide 3 also exhibit an avoided crossing. As shown in Figs. 2.5(a)−(b), one of the two coupled modes always resides in the wider air layer and has a larger effective index, as the core size in W_{core2} increases. The leakage loss for the modes confined in the core is dominated by the core size, when the same antiresonant layers are used. Hence, the mode that resides in the wider air layer always has a lower leakage loss, which leads to an avoided crossing in the leakage loss curves.

Next, we study the impact of glass layer thickness, t, on the width of the avoided crossing, δ, in waveguide 3. We fix W_{core1} and W_{core2} at 30 μm. We show the results in Fig. 2.6. The solid blue and dashed red curves show the width of the avoided crossing as the glass thickness varies. The solid blue curve shows the computational

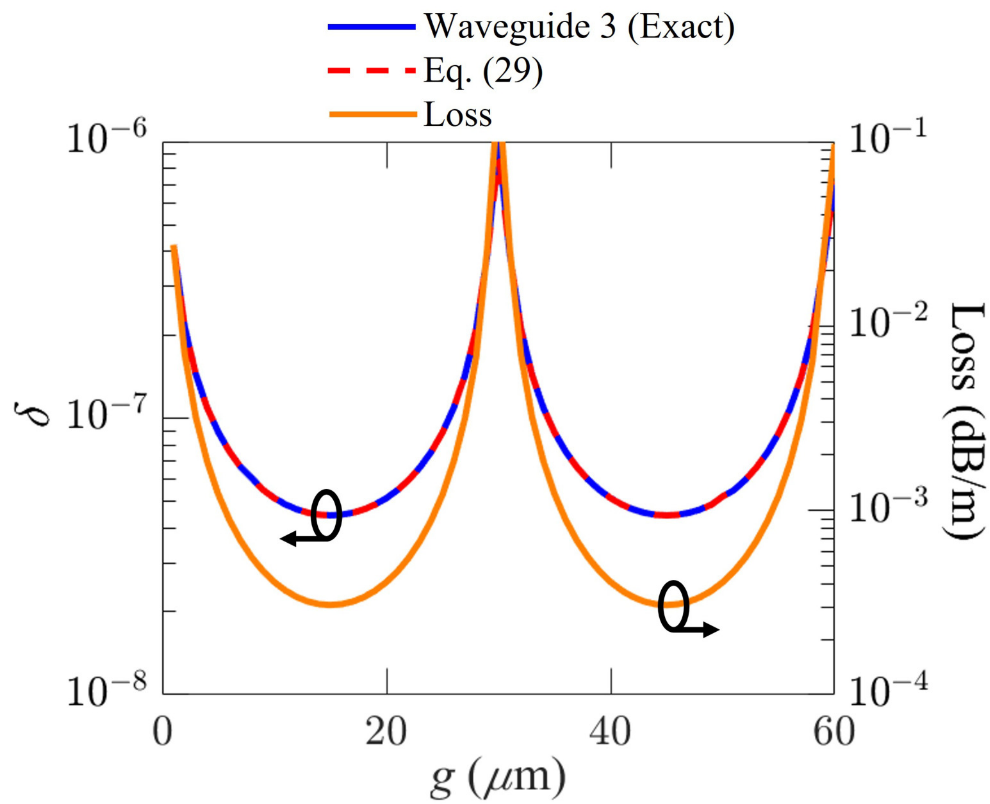

Figure 2.7: Width of avoided crossing and loss during an avoided crossing as a function of the width of air gap g with $t = 0.72$ μm and $W_{\text{core1}} = W_{\text{core2}} = 30$ μm. [Reprinted/Adapted] with permission from [33] © Optica Publishing Group.

result, while the dashed red curve shows the result from Eq. (2.29). The solid orange curve represents the loss. When the glass thickness is near 0.72 and 1.2 μm, which corresponds to antiresonance, the mode loss is low, and the width of the avoided crossing is small due to weak coupling. When the glass thickness is 0.95 μm, the resonance condition is satisfied, which leads to a large avoided crossing width and high loss.

We also study different gap sizes and show the results in Fig. 2.7. The glass thickness is now fixed at 0.72 μm. The solid blue and dashed red curves show respectively the computational result and the result from Eq. (2.29) for the avoided crossing width in waveguide 3. The solid orange curve represents the loss. When the air gap approaches a multiple of $W_{\text{core1}} = W_{\text{core2}} = 30$ μm, coupling between the air mode in

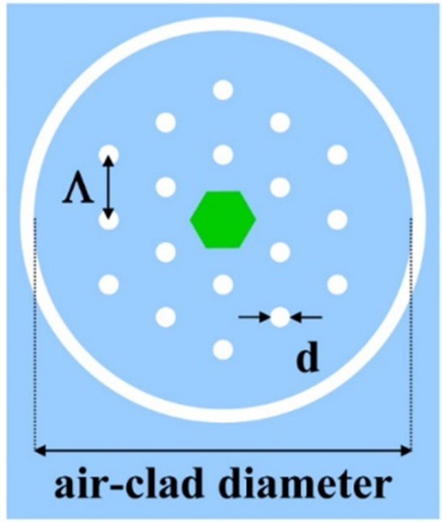

Figure 2.8: Schematic structure of a rare-earth doped (green region) double-clad LPF. [Reprinted/Adapted] with permission from [62] © Optica Publishing Group.

the core and HOM in the air gap becomes strong, the loss increases, and the width of avoided crossing increases.

2.6 Avoided crossings in optical fibers

Previous sections describe avoided crossings for the guided modes and leaky modes in slab waveguides where the modes can be described analytically. Avoided crossings play an important role in solid-core photonic crystal fibers [62], photonic bandgap fibers [63–67], negative curvature fibers [52–54], and kagome fibers [68], where simple analytical expressions for the modes do not exist and the modes must be found computationally. This section discusses two examples of avoided crossings in solid-core and air-core photonic crystal fibers. We then describe the similarities and differences between avoided crossings in the optical fibers and the simpler slab waveguides that we have analyzed in detail.

Jansen et al. [62] studied a large pitch photonic crystal fiber (LPF) as shown in Fig. 2.8. The pitch, Λ, diameter of hole, d, and wavelength are 30 μm, 0.9 μm, and 1.03 μm, respectively. The motivation to use an LPF with a large mode area comes from the

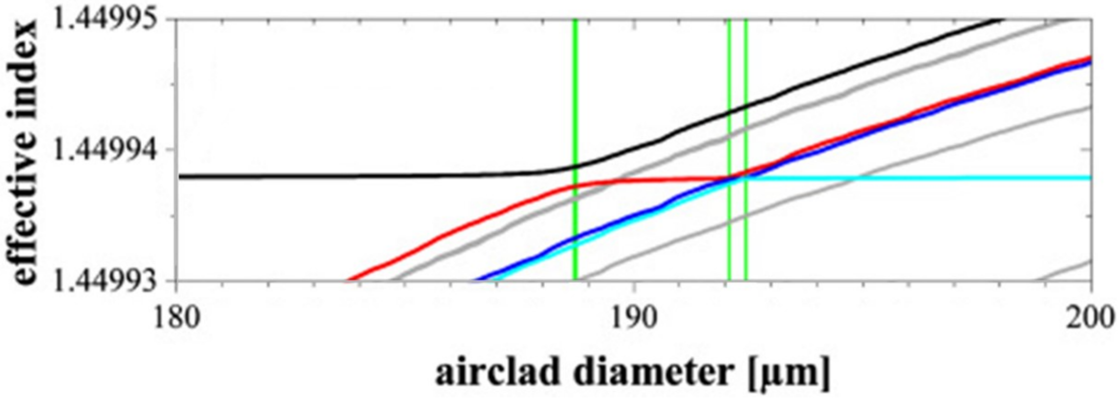

Figure 2.9: Detailed plot of one broad and two narrow avoided crossings (marked in green vertical lines). The modes involved in avoided crossings are shown in black, red, light blue, and blue. [Reprinted/Adapted] with permission from [62] © Optica Publishing Group.

requirement for high average output power. The advantage of using an LPF is that the HOMs are delocalized from the core, which leads to a reduction in the excitation of HOMs from a near-Gaussian beam, as well as increased loss for the HOMs [62]. Jansen et al. [62] also showed that different pump core diameters, bending radii and/or index depression may lead to avoided crossings that manifest themselves in unwanted deformations of the output beam. Figure 2.9 shows three avoided crossings in the effective index curves for the fundamental mode and the HOMs. As the air-clad diameter increases, the transverse mode profiles switch between modes. The same switching behavior is present in the slab waveguides that we analyzed in the previous sections and is generally present in any system with avoided crossings. Figure 2.10 shows the evolution of the transverse mode profiles at the first avoided crossing. As the air-clad diameter changes from 185 μm to 195 μm, the fundamental mode evolves to the HOM and the HOM profile completely switches places from the cladding to the core. The mode-switching that we show in Figs. 2.9 and 2.10 for the solid-core LPFs is analogous to the mode-switching that we showed in Figs. 2.2 and 2.5 for the slab waveguides.

Hollow-core fibers may also exhibit avoided crossings. A large core size is often used in hollow-core fibers to lower the fiber loss. At the same time, HOMs exist in

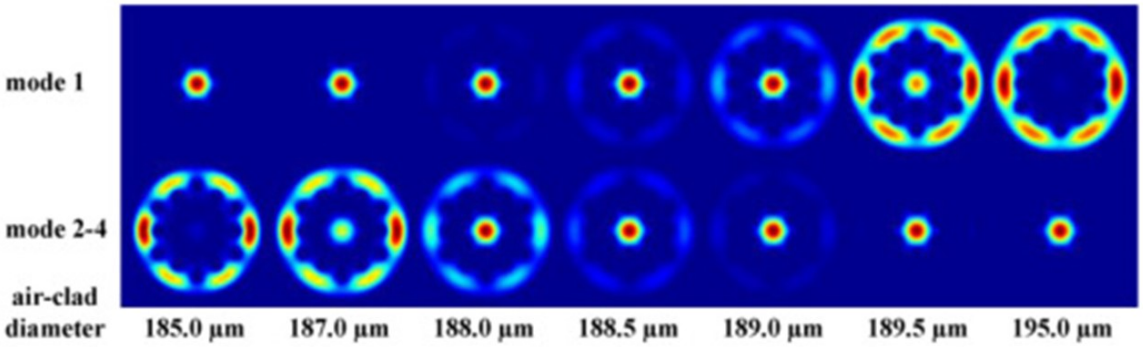

Figure 2.10: Transverse mode profiles of the modes involved in the broad avoided crossing of Fig. 2.9 around an air-clad diameter of 188.5 μm. Across the avoided crossing, the former fundamental mode evolves into an HOM, and an HOM takes over the role as the fundamental mode. Reprinted with permission from [62]. Copyright 2011 Optical Society of America.

the fiber with a large core. It is preferable to suppress higher-order core modes while preserving low leakage loss for the fundamental core mode [52, 75]. This approach is analogous to using resonant coupling between the core modes and defect modes in photonic bandgap fibers [63–67]. The work by Uebel et al. [75] optimized the ratio of the capillary tube diameter, d, to the air-core diameter, D so that an avoided crossing between the higher-order core modes and the fundamental tube modes leads to an increase in the loss of the higher-order core modes. Figure 2.11(a) shows the cross-section of the negative curvature fiber considered along with illustrations for the parameters d and D. Figures 2.11(b) and 2.11(c) show the transverse mode profiles for the fundamental mode and first HOM, respectively. Figure 2.12(a) shows the effective indices of the fundamental mode in orange, the first HOM in blue, and the antiresonant element (ARE) mode in red. The effective indices for the HOM and ARE mode exhibit an avoided crossing at a ratio $d/D = 0.68$. Figure 2.12(b) shows the loss for the fundamental mode, HOM, and ARE mode. At the ratio $d/D = 0.68$, the HOM loss exponentially increases while the fundamental mode loss stays low. To quantify the suppression of HOMs, Uebel et al. [75] introduced a figure of merit (FOM) as $\mathrm{FOM}_{lm} = \alpha_{lm}/\alpha_{01} - 1$, where α_{lm} is the loss for the LP_{lm} mode in dB/m and α_{01} is the loss of the fundamental core mode. The gray-shaded area in Fig. 2.12(b)

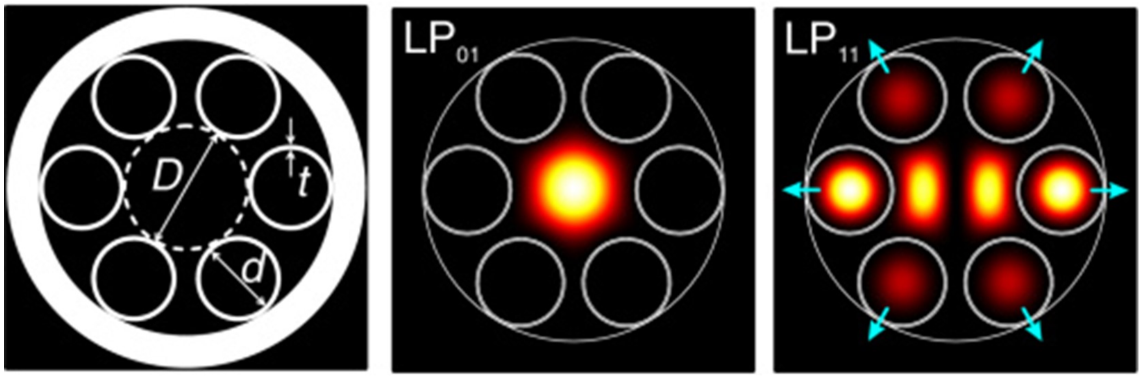

Figure 2.11: (a) Sketch of the structure, with the key dimensions marked in core diameter D, capillary inner diameter d, and wall thickness t. (b) Fundamental LP_{01} mode is strongly confined. (c) HOM experiences high loss because they are coupled to modes in the capillaries. Light in the core leaks out to the solid glass sheath (indicated by the blue arrows). [Reprinted/Adapted] with permission from [75] © Optica Publishing Group.

shows the region where $\mathrm{FOM}_{11} > 20$. Figure 2.12(c) shows a magnified plot of the avoided crossing between the HOM and the ARE mode.

In two-dimensional air-core bandgap fibers, West et al. [64] showed that loss is related to the width of the avoided crossing between the air-core mode and the surface modes supported at the core-cladding interface, which is consistent to what appears in Fig. 2.12 near the avoided crossing. Hence, the width of an avoided crossing is a key parameter in determining the loss of the fundamental core mode. Debord et al. [68] observed and analyzed a similar avoided crossing in the kagome fibers.

In both solid-core and air-core optical fibers, the core mode couples strongly to other core modes and cladding modes under certain conditions. The analysis of avoided crossings is useful in determining the mode coupling and the loss of the core mode in specialty solid-core and hollow-core fibers when coupling occurs between the core mode and cladding modes. Due to the complexity in design of many modern-day specialty fibers, numerical solutions must be employed to calculate the effective indices and observe the avoided crossings. However, the basic switching behavior and its dependence on the width of the avoided crossing are unchanged.

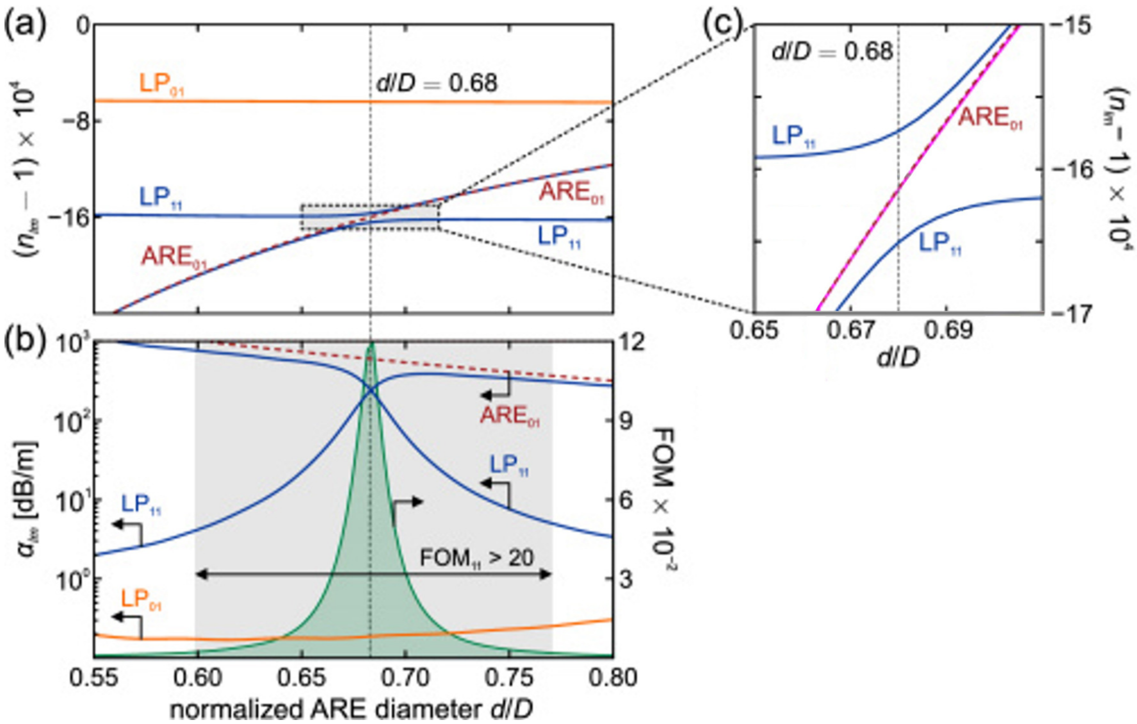

Figure 2.12: (a) Modal refractive indices of the LP_{01} (orange) and even and odd LP_{11} (blue) modes. (b) Modal losses and FOM_{11} (green). The brown dashed curves in each plot refer to the antiresonant element (ARE) mode of an isolated ARE capillary. For optimal HOM suppression, $d/\Lambda = 0.68$. The geometrical parameters are $t/D = 0.01$ and $D/\lambda = 20$. The gray-shaded area in (b) shows the region where $FOM_{11} > 20$. (c) Magnified plot of the avoided crossing in Fig. 2.12(a). [Reprinted/Adapted] with permission from [75] © Optica Publishing Group.

There are differences in the leakage loss curves during the avoided crossings between the slab waveguides and optical fibers. Because the slab waveguide is a one-dimensional structure, the leakage loss is dominated by the core size, meaning that one of the two modes will always have a higher loss as we change W_{core2} during the avoided crossing, as shown in Fig. 2.5. Hence, one of the two coupled modes always has a lower loss compared to the other coupled mode, and an avoided crossing is manifested in the leakage loss curves in Fig. 2.5(c). In two-dimensional structures, such as specialty optical fibers, the mode in the cladding has a higher loss than the mode in the core. Hence, the leakage loss curves in Fig. 2.12(b) cross, rather than forming an avoided crossing.

2.7 Summary

In this tutorial, we present coupled-mode theory in slab waveguides for both guided modes in index-guided waveguides and leaky modes in antiresonant waveguides. The theory for the former is classical and is covered in many textbooks, but the latter is not. Our goal is to emphasize the analogy between these two waveguide types. Antiresonant photonic crystal fibers have become important in applications, but geometries are too complex to be simply analyzed. For both waveguide types, we considered a geometry with two cores. For the index-guided waveguide, the two cores are separated and surrounded by a lower-index cladding. For the antiresonant waveguide, the two air cores are separated from each other and from the air cladding by double-glass partitions. Although the modes in the antiresonant waveguides are leaky, the theoretical development to determine the mode coupling near an avoided crossing is almost identical. Antiresonance implies that the avoided crossings are weak and the modes are well confined to the cores. This behavior is analogous to guided-mode waveguides with a large gap between cores. When the modes are well-confined, the leakage is low, and hence so is the loss. The correlation between loss and width of the avoided crossing is important in applications to photonic crystal fibers since it is usually desirable to have low loss. There is no analogous loss mechanism in index-guided waveguides. Coupled-mode theory accurately predicts the magnitude of the avoided crossings and their locations as parameters vary for both waveguide types.

In conclusion, we have shown that it is possible to explain the principal features of avoided crossings in index-guided and antiresonant waveguides using a simple slab waveguide model. We have also shown that a coupled-mode theory that is close to the standard theory for guided modes can be used to predict the behavior of the avoided crossings for leaky modes. We discussed examples of avoided crossings in solid-core and air-core optical fibers. We described the similarities and differences between the specialty optical fibers and the simpler slab waveguides that we have analyzed in detail. Thus, this model is a useful basis for understanding avoided crossings in the more complex geometries that are typically found in photonic crystal fibers.

CHAPTER THREE

Phase-Matched Model for the Transverse Mode Instability

This chapter published as [80]: C. R. Menyuk, J. T. Young, J. Hu, A. J. Goers, D. M. Brown, and M. L. Dennis, "Accurate and Efficient Modeling of the Transverse Mode Instability in High Energy Laser Amplifiers," Opt. Express **29**(12), 17746–17757 (2021).

In this chapter, we formulate the phase-matched model for the transverse mode instability (TMI) and compare it to the full model. We study TMI in the limit where a single higher-order mode (HOM) is present. We demonstrate that when the beat length between the fundamental mode and the HOM is small compared to the length scales on which the pump amplitude and the optical mode amplitudes vary, TMI is a three-wave mixing process in which the two optical modes beat with the phase-matched component of the index of refraction that is induced by the thermal grating. This limit is the usual limit in applications, and in this limit TMI is identified as a stimulated thermal Rayleigh scattering (STRS) process. We demonstrate that a phase-matched model that is based on the three-wave mixing equations can have a large computational advantage over current coupled mode methods that must use longitudinal step sizes that are small compared to the beat length.

3.1 Introduction

Ytterbium-doped fiber amplifiers that produce kilowatt output powers have been developed in the past decade [4, 26, 81–85]. However, the thermal or transverse mode instability (TMI) has become a major barrier to achieving even higher output powers [2,3,86]. Despite almost a decade of work since the original observation of TMI in fiber amplifiers by Jauregui et al. [87] and Eidam et al. [88], it still remains only partially understood, and computationally-efficient methods that are sufficiently accurate for amplifier design have been lacking. It was recognized early by Smith and Smith [89] that the instability could be explained by a thermal grating that is induced by the beating of the fundamental mode of the optical fiber with a higher-order mode at a slightly lower frequency and the quantum defect heating that ensues.

Subsequent work by Jauregui et al. [90], Dong [91], and Smith and Smith [92] identified the instability as a stimulated thermal Rayleigh scattering (STRS) process. In particular, Dong [91] developed a three-wave mixing model that is analogous to models of the Brillouin instability due to stimulated Brillouin scattering (SBS). This identification has remained somewhat controversial, although Kong et al. [93] directly observed the STRS process in a fiber amplifier. Ward et al. [94] and Naderi et al. [95] developed a model of TMI based on a coupled mode method that makes no reference to three-wave interactions. The complexity of TMI has obscured its identification as an STRS-driven, three-wave process. The conditions that are required to treat TMI as a three-wave instability have not been elucidated.

In this work, we demonstrate that the key requirement is that the beat length $L_{\mathrm{B}} = 2\pi/\Delta\beta$ must be small compared to any other longitudinal scale lengths, where $\Delta\beta$ is the difference between the wavenumber of the fundamental mode and any higher-order modes (HOMs) at the same frequency. This condition usually applies in practice. In this limit, we derive the three-wave equations that govern TMI. Terms that are not phase-matched are neglected. This approach is similar to Dong's approach [91], but is more general.

We further demonstrate that this approach has a large computational advantage. Approaches that use the coupled mode method, like the approach of Naderi et al. [95], must use longitudinal steps in their computations that are small compared to the beat length. As a result, Naderi et al. [95] limited their study to a high-gain amplifier with a length of 1.6 m, which is substantially shorter than typical ytterbium-doped fiber amplifiers. Approaches that use the finite-element method to calculate the optical mode profile on each longitudinal step like that of Ward [96] must take steps that are small compared to the optical wavelength and typically require large computational resources. Our approach is only limited by the longitudinal scale lengths over which the amplitudes of the optical modes, the thermal mode, and the pump mode change. These lengths are typically far larger than the beat length. For the examples that we consider in this chapter, which correspond to realistic Yb^{3+}-doped fiber amplifiers, the computational speedup is more than a factor of 100.

3.2 *Theoretical model*

We may write the index of refraction as $n(\mathbf{r}_\perp, z, t) = n_0(\mathbf{r}_\perp) + \Delta n(\mathbf{r}_\perp, z, t)$, where $n_0(\mathbf{r}_\perp)$ is the unperturbed index of refraction, and we set $\Delta n \ll n_0$, which is always the case ($\Delta n/n_0 \sim 10^{-5}$). We will use the slowly varying envelope approximation, which is an excellent approximation in this system due to the large discrepancy between the wavelength and the next-smallest scale, which is the intermodal beat length L_B. We will also assume that time derivatives of the index of refraction can be ignored when calculating the inter-modal coupling. That is again an excellent approximation, given the large disparity between the light period and the time scale on which either the gain changes (microseconds) or the temperature changes (milliseconds). We assume as well that the only coupling is between modes that are propagating in the forward direction. We start with the expression from coupled mode theory for two coupled modes [97, 98],

$$\begin{aligned} \frac{dA_0}{dz} &= \frac{i\omega^2}{\beta c^2} \int d^2\mathbf{r}_\perp n_0 \Delta n \left[|\boldsymbol{\mathcal{E}}_0|^2 A_0 + \boldsymbol{\mathcal{E}}_0^* \cdot \boldsymbol{\mathcal{E}}_1 \exp(-i\Delta\beta z) A_1 \right], \\ \frac{dA_1}{dz} &= \frac{i\omega^2}{\beta c^2} \int d^2\mathbf{r}_\perp n_0 \Delta n \left[|\boldsymbol{\mathcal{E}}_1|^2 A_1 + \boldsymbol{\mathcal{E}}_1^* \cdot \boldsymbol{\mathcal{E}}_0 \exp(i\Delta\beta z) A_0 \right], \end{aligned} \tag{3.1}$$

where $\boldsymbol{\mathcal{E}}_0$ and $\boldsymbol{\mathcal{E}}_1$ are the normalized transverse mode profiles for the fundamental mode and the HOM, while A_0 and A_1 are the corresponding amplitudes. We have set $\beta \equiv \beta_0 \approx \beta_1$ since $\Delta\beta = \beta_0 - \beta_1 \ll \beta_{0,1}$. Equation (3.1) is valid when only a single HOM is present or when the amplitudes of the other HOMs are small compared to A_0 and A_1.

To solve Eq. (3.1) at any point in time t, we must find $\Delta n(\mathbf{r}_\perp, z, t)$. Due to the factors $\exp(\pm i\Delta\beta z)$ that appear in Eq. (3.1), it is necessary to determine $\Delta n(\mathbf{r}_\perp, z, t)$ with a computational resolution Δz that is small compared to the beat length $L_\mathrm{B} = 2\pi/\Delta\beta$ even though the field amplitudes vary slowly compared to this length. Since we must determine the transverse dependence of Δn as well, this constraint is computationally demanding. We can bypass this difficulty by replacing the field $\Delta n(\mathbf{r}_\perp, z, t)$ with three fields $\Delta n_0(\mathbf{r}_\perp, z, t)$, $\Delta n_+(\mathbf{r}_\perp, z, t)$, and $\Delta n_-(\mathbf{r}_\perp, z, t)$, which are defined so that

$$\Delta n = \Delta n_0 + \frac{1}{2}[\Delta n_+ \exp(i\Delta\beta z) + \Delta n_- \exp(-i\Delta\beta z)], \tag{3.2}$$

and Δn_0, Δn_+, and Δn_- all vary slowly compared to the beat length L_B. When we substitute Eq. (3.2) into Eq. (3.1) and keep only the phase-matched terms, we obtain

$$\begin{aligned}
\frac{dA_0}{dz} &= \frac{i\omega^2}{\beta c^2}\int d^2\mathbf{r}_\perp n_0 \left[|\boldsymbol{\mathcal{E}}_0|^2 \Delta n_0 A_0 + \frac{1}{2}\boldsymbol{\mathcal{E}}_0^* \cdot \boldsymbol{\mathcal{E}}_1 \Delta n_+ A_1\right], \\
\frac{dA_1}{dz} &= \frac{i\omega^2}{\beta c^2}\int d^2\mathbf{r}_\perp n_0 \left[|\boldsymbol{\mathcal{E}}_1|^2 \Delta n_0 A_1 + \frac{1}{2}\boldsymbol{\mathcal{E}}_1^* \cdot \boldsymbol{\mathcal{E}}_0 \Delta n_- A_0\right].
\end{aligned} \tag{3.3}$$

The terms that are not phase-matched are rapidly oscillating and do not contribute significantly to the integrals. All terms in Eq. (3.3) vary slowly in z. It then becomes possible to integrate Eq. (3.3) with no loss of accuracy while using a resolution in z that is far larger than is necessary with Eq. (3.1).

The form of Eq. (3.3) makes clear that in the limit where Eq. (3.3) is valid, TMI is effectively a three-wave process in which two optical fields combine with a density field. The condition for Eq. (3.3) to be valid is that all terms must vary slowly compared to the beat length. This condition is almost always met in practice. Since the density field is thermally driven, this process is a stimulated Rayleigh scattering process. We discuss this identification in more detail in the Appendix.

The procedure that we use to obtain Δn_0, Δn_+, and Δn_- in terms of the field and as a function of time is analogous to the procedure that is used by Naderi et al. [95] that is illustrated in Fig. 3.1.

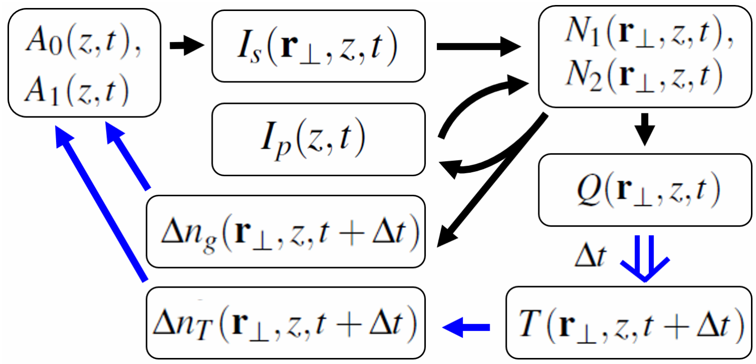

Figure 3.1: Schematic flow diagram of the computational procedure. The time step occurs when $T(t+\Delta t)$ is calculated using $Q(t)$. [Reprinted/Adapted] with permission from [80] © Optica Publishing Group.

We begin by writing the signal intensity $I_s(\mathbf{r}_\perp, z, t)$ as

$$I_s(\mathbf{r}_\perp, z, t) = I_{s0} + \frac{1}{2}\left[I_{s+}\exp(i\Delta\beta z) + I_{s-}\exp(-i\Delta\beta z)\right], \tag{3.4}$$

where

$$I_{s0} = \frac{\beta}{2\mu_0\omega}\left(|\boldsymbol{\mathcal{E}}_0|^2|A_0|^2 + |\boldsymbol{\mathcal{E}}_1|^2|A_1|^2\right), \qquad I_{s+} = I_{s-}^* = \frac{\beta}{\mu_0\omega}\boldsymbol{\mathcal{E}}_1^* \cdot \boldsymbol{\mathcal{E}}_0 A_1^* A_0, \tag{3.5}$$

all vary slowly compared to L_B. The behavior of a Yb-doped fiber amplifier is accurately described as a two-level system at realistic power levels [4]. Given $I_s(\mathbf{r}_\perp, z, t)$ and the pump intensity $I_p(z,t)$, we next compute the upper state density $N_2(\mathbf{r}_\perp, z, t)$ of the Yb ions, which is given by

$$N_2 = \frac{\sigma_p^{(\mathrm{a})}(I_p/\hbar\omega_p) + \sigma_s^{(\mathrm{a})}(I_s/\hbar\omega)}{\left[\sigma_p^{(\mathrm{a})} + \sigma_p^{(\mathrm{e})}\right](I_p/\hbar\omega_p) + \left[\sigma_s^{(\mathrm{a})} + \sigma_s^{(\mathrm{e})}\right](I_s/\hbar\omega) + 1/\tau} N_0, \tag{3.6}$$

where ω and ω_p are the signal and pump angular frequencies, respectively, τ is the spontaneous decay time of the upper level, N_0 is total density of Yb ions, and $\sigma_p^{(\mathrm{a})}$, $\sigma_p^{(\mathrm{e})}$, $\sigma_s^{(\mathrm{a})}$, and $\sigma_s^{(\mathrm{e})}$ are the absorption and emission cross-sections at the pump and signal frequencies. Because I_s appears in both the numerator and denominator of Eq. (3.6), the density N_2 will have higher harmonics that are proportional to $\exp(\pm im\Delta\beta)$ with $m > 1$. We will truncate this expression since the harmonics with $m > 1$ are not phase-matched. Explicitly, we find that Eq. (3.6) has the form

$$N_2 = \frac{A + B\cos\theta}{C + D\cos\theta} N_0, \tag{3.7}$$

where $\theta = \Delta\beta z + \phi$ and $\phi = \angle(A_1^* A_0 \boldsymbol{\mathcal{E}}_1^* \cdot \boldsymbol{\mathcal{E}}_0)$. We have

$$
\begin{aligned}
A = \sigma_p^{(\mathrm{a})} \frac{I_p}{\hbar\omega_p} + \sigma_s^{(\mathrm{a})} \frac{I_{s0}}{\hbar\omega}, \qquad B = \sigma_s^{(\mathrm{a})} \frac{|I_{s+}|}{\hbar\omega}, \\
C = \left[\sigma_p^{(\mathrm{a})} + \sigma_p^{(\mathrm{e})}\right] \frac{I_p}{\hbar\omega_p} + \left[\sigma_s^{(\mathrm{a})} + \sigma_s^{(\mathrm{e})}\right] \frac{I_{s0}}{\hbar\omega} + \frac{1}{\tau}, \\
D = \left[\sigma_s^{(\mathrm{a})} + \sigma_s^{(\mathrm{e})}\right] \frac{|I_{s+}|}{\hbar\omega}.
\end{aligned}
\tag{3.8}
$$

We note that $D < C$ and $B < C$ is a consequence of $I_{s+} < I_{s0}$, which in turn follows from the Cauchy-Schwartz inequality. We now write

$$
N_2 \simeq N_{20} + \frac{1}{2}\left[N_{2+}\exp(i\Delta\beta z) + N_{2-}\exp(-i\Delta\beta z)\right], \tag{3.9}
$$

where

$$
\begin{aligned}
N_{20} = \frac{A}{C}\frac{1}{r}\left(1 - \frac{BD}{AC}\frac{1}{1+r}\right) N_0, \\
N_{2+} = N_{2-}^* = \frac{A}{C}\frac{2}{r(1+r)}\left(\frac{B}{A} - \frac{D}{C}\right) N_0 \exp(i\phi),
\end{aligned}
\tag{3.10}
$$

with $r = (1 - D^2/C^2)^{1/2}$ [99]. Equation (3.10) is an exact truncation, not an expansion. We will show in Sec. 3 that the contribution of higher harmonics with $m > 1$ are negligible.

The next stages in the procedure are more straightforward. TMI is generated by the heat deposition due to the quantum defect between the pump and the signal, which in turn leads to a time-delayed temperature response that changes the index of refraction. The temperature response depends linearly on the heat deposition, which in turn depends linearly on the upper state density. From the expression for the heat deposition Q,

$$
Q = \left(1 - \frac{\omega}{\omega_p}\right)\left[\sigma_p^{(\mathrm{a})} N_0 - \left(\sigma_p^{(\mathrm{a})} + \sigma_p^{(\mathrm{e})}\right) N_2\right] I_p, \tag{3.11}
$$

we find

$$
\begin{aligned}
Q_0 = \left(1 - \frac{\omega}{\omega_p}\right)\left[\sigma_p^{(\mathrm{a})} N_0 - \left(\sigma_p^{(\mathrm{a})} + \sigma_p^{(\mathrm{e})}\right) N_{20}\right] I_p, \\
Q_+ = Q_-^* = -\left(1 - \frac{\omega}{\omega_p}\right)\left(\sigma_p^{(\mathrm{a})} + \sigma_p^{(\mathrm{e})}\right) N_{2+} I_p,
\end{aligned}
\tag{3.12}
$$

where $Q = Q_0 + (1/2)[Q_+ \exp(i\Delta\beta z) + Q_- \exp(-\Delta\beta z)]$. Similarly, from the expression for the temperature evolution,

$$\rho C \frac{\partial T}{\partial t} - \kappa \nabla_\perp^2 T = Q, \tag{3.13}$$

where ρ is the density, C is the heat capacity, and κ is the heat diffusivity, we find

$$\rho C \frac{\partial T_0}{\partial t} - \kappa \nabla_\perp^2 T_0 = Q_0, \qquad \rho C \frac{\partial T_+}{\partial t} - \kappa \nabla_\perp^2 T_+ = Q_+, \tag{3.14}$$

where $T = T_0 + (1/2)[T_+ \exp(i\Delta\beta z) + T_- \exp(-\Delta\beta z)]$ and $T_- = T_+^*$. Integrating Eq. (3.13) over time in the full model and Eq. (3.14) over time in the phase-matched model, we can now obtain $T(\mathbf{r}_\perp, z, t + \Delta t) - T(\mathbf{r}_\perp, z, t)$. Since the temperature tends to a constant T_{room} at large radius, the appropriate boundary conditions for both T and T_0 at large radius are $T_0 = T_{\mathrm{room}}$, and the appropriate boundary condition for T_+ is $T_+ = 0$. This integration is where the basic time step occurs, as we show schematically in Fig. 3.1, and it is this step that is computationally time-consuming.

We can now find the change in the index of refraction. There are two contributions to the index of refraction that we must take into account. The first contribution is from the temperature change, for which $\Delta n_T = (dn/dT)(T - T_{\mathrm{room}})$ and $\Delta n_{T0} = (dn/dT)(T_0 - T_{\mathrm{room}})$, $\Delta n_{T+} = (dn/dT)T_+$ in the phase-matched model. The second contribution is from the gain,

$$g(\mathbf{r}_\perp, z, t) = \left(\sigma_s^{(\mathrm{e})} + \sigma_s^{(\mathrm{a})}\right) N_2(\mathbf{r}_\perp, z, t) - \sigma_s^{(\mathrm{a})} N_0(\mathbf{r}_\perp), \tag{3.15}$$

from which we find

$$\Delta n_g = -i\frac{c}{2\omega}\left[\left(\sigma_s^{(\mathrm{e})} + \sigma_s^{(\mathrm{a})}\right) N_2(\mathbf{r}_\perp, z, t) - \sigma_s^{(\mathrm{a})} N_0(\mathbf{r}_\perp)\right]. \tag{3.16}$$

It follows that

$$\begin{aligned} \Delta n_{g0} &= -i\frac{c}{2\omega}\left[\left(\sigma_s^{(\mathrm{e})} + \sigma_s^{(\mathrm{a})}\right) N_{20} - \sigma_s^{(\mathrm{a})} N_0\right], \\ \Delta n_{g+} &= -\Delta n_{g-}^* = -i\frac{c}{2\omega}\left(\sigma_s^{(\mathrm{e})} + \sigma_s^{(\mathrm{a})}\right) N_{2+}, \end{aligned} \tag{3.17}$$

where $\Delta n_g = \Delta n_{g0} + (1/2)[\Delta n_{g+} \exp(i\Delta\beta z) + \Delta n_{g-} \exp(-i\Delta\beta z)]$. Although Δn_g is purely imaginary, the components Δn_{g+} and Δn_{g-} are not. Naderi et al. [95] have pointed out that the corresponding phase shift does not contribute to the instability, but plays an important role in the energy balance. Finally, we obtain $\Delta n_0 = \Delta n_{T0} + \Delta n_{g0}$, $\Delta n_+ = \Delta n_{T+} + \Delta n_{g+}$, and $\Delta n_- = \Delta n_{T-} + \Delta n_{g-}$. In the full model, the terms that are not phase-matched are rapidly oscillating and do not contribute significantly to the overall gain or loss. In the phase-matched model, the slowly varying terms Δn_0, Δn_+, and Δn_- are used to replace Δn, as shown in Eq. (3.2), and the overall gain or loss for the fundamental mode and HOM can be predicted.

To complete the model equations, we must obtain the pump intensity $I_p(z,t)$. We use the expression

$$\frac{dI_p}{dz} = \pm \left[\left(\sigma_p^{(\mathrm{e})} + \sigma_p^{(\mathrm{a})} \right) \overline{N_2} - \overline{N_0} \right] I_p, \tag{3.18}$$

where the overbar indicates that the population densities are averaged over the cross-section of the pump. The sign depends on whether the pump is forward- or backward-propagating. Eq. (3.18) becomes

$$\frac{dI_p}{dz} = \pm \left[\left(\sigma_p^{(\mathrm{e})} + \sigma_p^{(\mathrm{a})} \right) \overline{N_{20}} - \overline{N_0} \right] I_p, \tag{3.19}$$

in the phase-matched model.

In this chapter, we focused on the contribution to TMI due to the quantum defect heating. It has been shown that photodarkening can also contribute to TMI [30, 100]. Photodarkening contributes to the thermally induced index grating coherently with quantum defect heating [2]. Hence, the heat source term and absorption term from photodarkening [30] could be added to Eqs. (3.11,3.12) and Eqs. (3.15,3.16), respectively, to include the photodarkening effect in the phase-matched model for TMI.

3.3 Verification, accuracy, and timing of the phase-matched model

In this section, we first verify the phase-matched model, [Eqs. (3.3), (3.8), (3.12), (3.14), (3.17), (3.19)] by comparing its predictions to those of the full model, [Eqs. (3.1), (3.6), (3.11), (3.13), (3.16), (3.18)]. We will show that agreement is excellent for a realistic amplifier system similar to the system that Naderi et al. [95] considered, but using a fiber length of 10 m, which is a typical experimental length [85, 101]. We then consider in more detail the error as a function of the step size Δz and show that the phase-matched model has a significant computational advantage.

3.3.1 Verification

We show the basic set of parameters that we are considering in Table 3.1. These parameters are similar to those used in [95], but with a more realistic amplifier length of 10 m. We use the alternating-direct-implicit (ADI) method to integrate the temperature equations, and we used the Runge-Kutta method to carry out the z-integration. In all the simulations reported here, we used a 140×140 μm^2 square grid for the transverse integration with a 2×2 μm^2 grid spacing. We verified that using a larger grid size of 160×160 μm^2 with a smaller grid spacing of 1×1 μm^2 makes a negligible difference in Figs. 3.2 and 3.3. We chose the z-step sufficiently small so that the relative error is below 1%. In all the simulations reported here, we used a noise seed ratio at the entry to the optical fiber of 10^{-4} between the higher-order mode and the

Table 3.1. TMI model simulation parameters

$L_{\text{fiber}} = 10$ m	$n_{\text{core}} = 1.45031$
$D_{\text{core}} = 50$ μm	$N.A. = 0.03$
$D_{\text{cladding}} = 250$ μm	$\lambda_{\text{pump}} = 977$ nm
$N_0 = 1 \times 10^{25}$ m^{-3}	$\lambda_{\text{signal}} = 1064$ nm
$\sigma_p^{(e)} = 1.87 \times 10^{-27}$ m^2	$\sigma_p^{(a)} = 1.53 \times 10^{-24}$ m^2
$\sigma_s^{(e)} = 6 \times 10^{-27}$ m^2	$\sigma_s^{(a)} = 3.58 \times 10^{-25}$ m^2

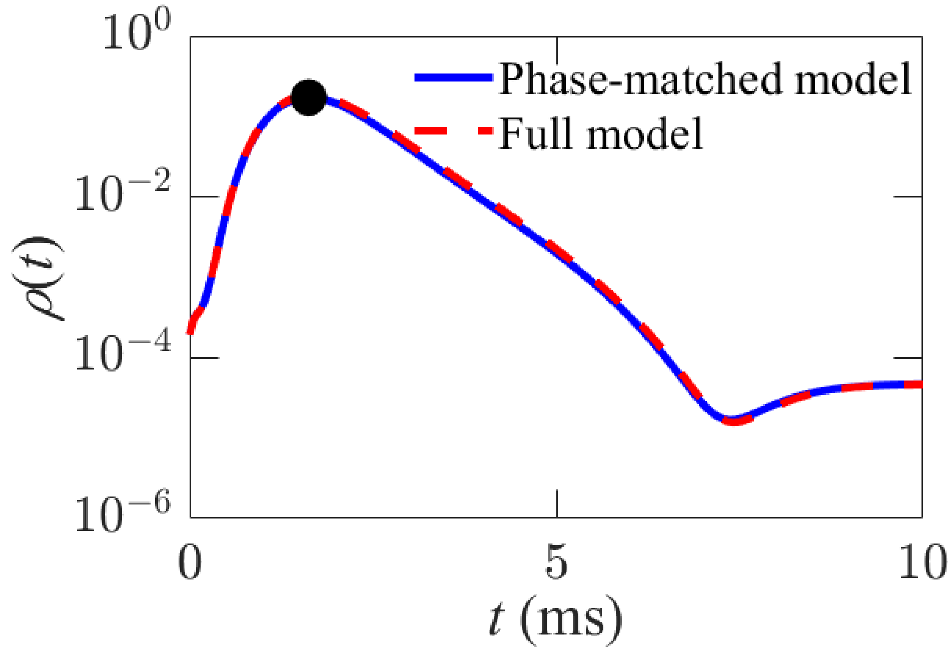

Figure 3.2: Power ratio $\rho(t) = P_{\mathrm{HOM}}(t)/P_{\mathrm{total}}(t)$ at the end of the amplifier vs. time t. The pump power equals 250 W. [Reprinted/Adapted] with permission from [80] © Optica Publishing Group.

fundamental mode. We verified that using a noise seed ratio of 10^{-3} or 10^{-5} does not change the agreement between the full and phase-matched models that we present in Figs. 3.2 and 3.3.

In Fig. 3.2, we show a comparison of the ratio $\rho(t) = P_{\mathrm{HOM}}(t)/P_{\mathrm{total}}(t)$ of the power in the higher-order mode $P_{\mathrm{HOM}}(t)$ to the total power $P_{\mathrm{total}}(t)$ at the end of the fiber as a function of time. In the case that we show here, the input pump power P_{pump} equals 250 W. With this pump power, we find that $\rho(t)$ rises to a maximum of 17%, shown as a dot in Fig. 3.2, before returning to a value that is close to the initial higher-order mode seeding. We observe excellent agreement between the full model and the phase-matched model. As the pump power increases, we continue to observe excellent agreement between the two models, although when the pump power is large enough where both models predict chaotic oscillations, the agreement is qualitative

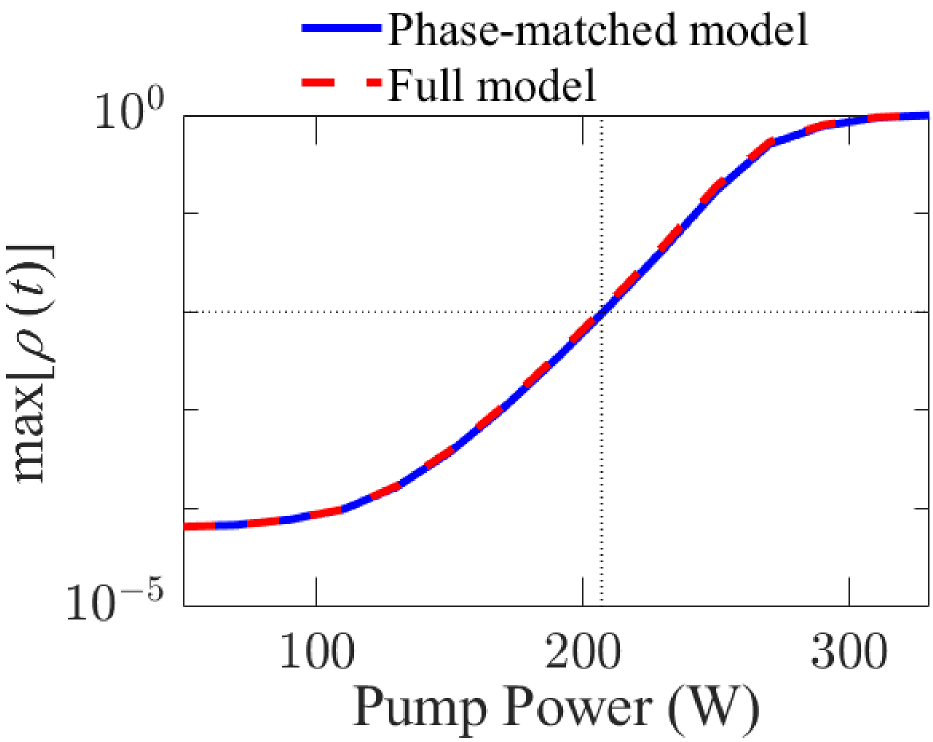

Figure 3.3: Maximum power ratio $\max[\rho(t)]$ at the amplifier end vs. input pump power P_{pump}. The threshold ratio of 1% occurs when $P_{\text{pump}} = 207$ W. [Reprinted/Adapted] with permission from [80] © Optica Publishing Group.

rather than quantitative. This behavior is expected since small changes in the seeding ratio also produce large changes in this limit due to the butterfly effect [102].

In Fig. 3.3, we show $\max[\rho(t)]$ vs. P_{pump} and a dotted line that corresponds to a ratio of 1%. We observe excellent agreement between the phase-matched model and the full model. In this work, we define the threshold power as the lowest pump power at which $\max[\rho(t)] > 0.01$, i.e., the ratio of $P_{\text{HOM}}(t)/P_{\text{total}}(t)$ exceeds 1% at any time. Beyond this threshold, the beam quality rapidly degrades [87, 88, 103, 104]. This definition of the threshold is consistent with studies of amplifier limits due to SBS. In the case considered here, the threshold power equals 207 W.

In Fig. 3.4, we show the temperature as a function of longitudinal position z and the absolute value of its spatial Fourier transform at a distance of 10 μm from the amplifier center and a time $t = 0.5$ ms. We set $P_{\text{pump}} = 450$ W. In Fig. 3.4(a), where we show the temperature as a function of position, we see that the agreement between the full model and the phase-matched model appears excellent. In the inset, where we show the spatial oscillations, the two models appear indistinguishable. However, the subtle difference is visible in Fig. 3.4(b), where we show the absolute value of the spatial Fourier transform, $|\mathrm{FT}(T)| = |\int T(z)\exp(ikz)\,dz|$. Agreement is excellent for the central harmonic, as well as the two surrounding harmonics which are located at $k = \pm\Delta\beta = \pm 528\ \mathrm{m}^{-1}$. However, the phase-matched model has no contribution from the harmonics at $\pm n\Delta\beta$, where $n \geq 2$. It is precisely these higher harmonics that we are neglecting.

3.3.2 Accuracy and timing

In the phase-matched model, the number of dependent variables is almost twice as large as in the full model. In particular, it is necessary to solve the temperature equation, Eq. (3.14), for both T_0 and T_+ instead of just solving the temperature equation, Eq. (3.13), for the single temperature T. As a result, we have found that the computational load on each z-step increases by roughly a factor of two. However, it is possible to take significantly larger steps, leading to a large computational advantage.

In Fig. 3.5, we show $\max[\rho(t)]$ for both the full model and phase-matched model as a function of $L_\mathrm{B}/\Delta z$ when $P_\mathrm{pump} = 250$ W, so that the pump power is slightly above threshold. As expected, the full model requires an $L_\mathrm{B}/\Delta z > 60$ to converge, while the phase-matched model appears to have converged in this case when $L_\mathrm{B}/\Delta z \simeq 2$.

In order to quantify the convergence, we define the relative error, ϵ, as the difference between our computation at a given Δz and a four-point Richardson extrapolation [105]. For the full model, we used $L_\mathrm{B}/\Delta z = 80$, 40, 20, and 10 for the extrapolation. For the phase-matched model, we used $L_\mathrm{B}/\Delta z = 40$, 20, 10, and 5.

In Fig. 3.6(a), we show the relative error as a function of $L_\mathrm{B}/\Delta z$. We see that achieving a relative error of 1% with the full model requires $L_\mathrm{B}/\Delta z \simeq 90$, while the

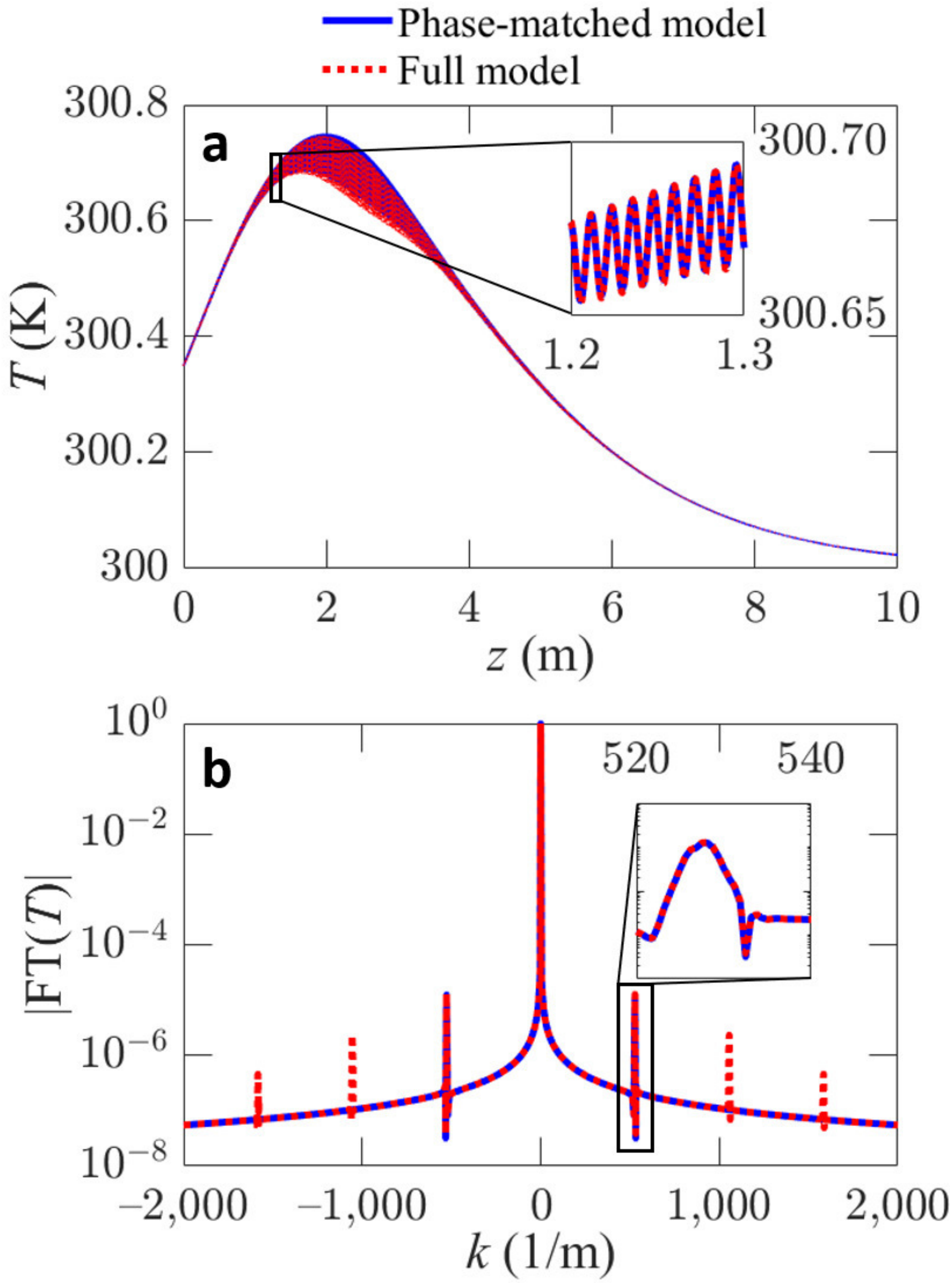

Figure 3.4: Temperature T at a point that is 10 μm from the amplifier center when $t = 0.5$ ms. (a) T vs. z. Agreement is excellent between the full model and the phase-matched model. The inset shows that the details of the temperature oscillations agree. (b) $|\mathrm{FT}(T)|$ vs. k, where k is the spatial Fourier transform variable. Agreement for the central harmonic and the harmonics at $k = \pm\Delta\beta$ is excellent. The inset shows excellent agreement for the harmonic at $k = \Delta\beta$. However, the harmonics at $k = \pm n\Delta\beta$ for $n \geq 2$ are not present in the phase-matched model. [Reprinted/Adapted] with permission from [80] © Optica Publishing Group.

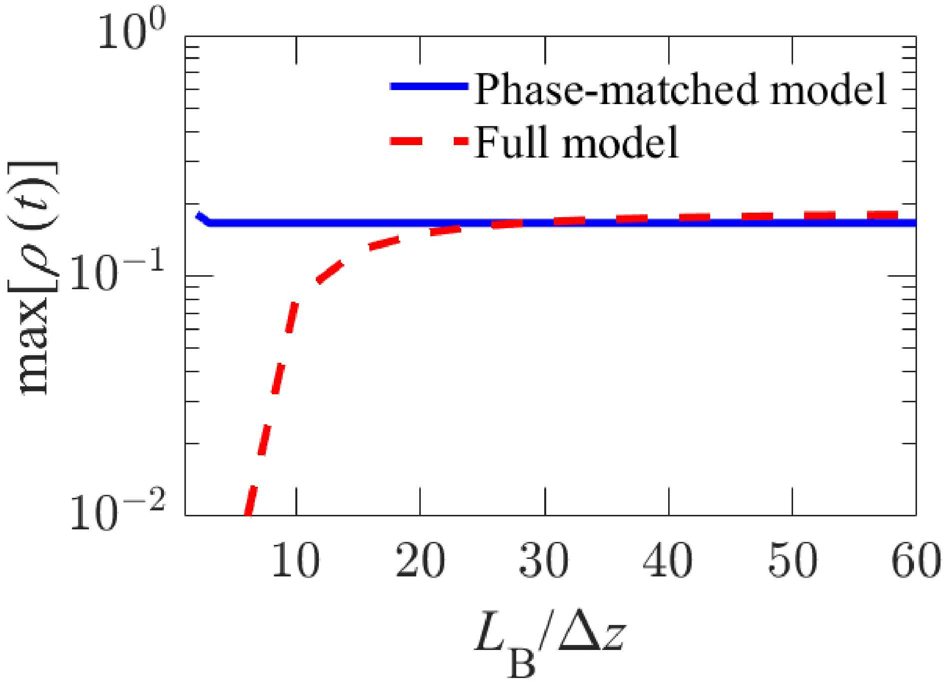

Figure 3.5: Convergence of the maximum power ratio at the amplifier end as $L_B/\Delta z$ increases. We set $P_{\mathrm{pump}} = 250$ W. [Reprinted/Adapted] with permission from [80] © Optica Publishing Group.

same relative error can be obtained with the phase-matched model when $L_\mathrm{B}/\Delta z \simeq 2$. Figure 3.6(a) also illustrates that the full model is second-order accurate in Δz, so that the relative error decreases proportional to $(\Delta z)^{-2}$. This result is consistent with the result of Naderi et al. [95], but may be surprising since our integration in z is done using the Runge-Kutta method. This result indicates that the global error is dominated by the accumulated error in computing the index of refraction. The variation of the relative error in the phase-matched model is more complex since it depends on the rate at which all the dependent variables change as a function of z. A complete error analysis is beyond the scope of this study, but Fig. 3.6(a) indicates that it decreases rapidly as Δz increases until it has become quite small.

In Fig. 3.6(b), we show the runtime of both the full model and the phase-matched model using 16 cores in a shared memory system that consists of dual Intel E5-2695 V4 processors. We observe that the runtime for the phase-matched model is

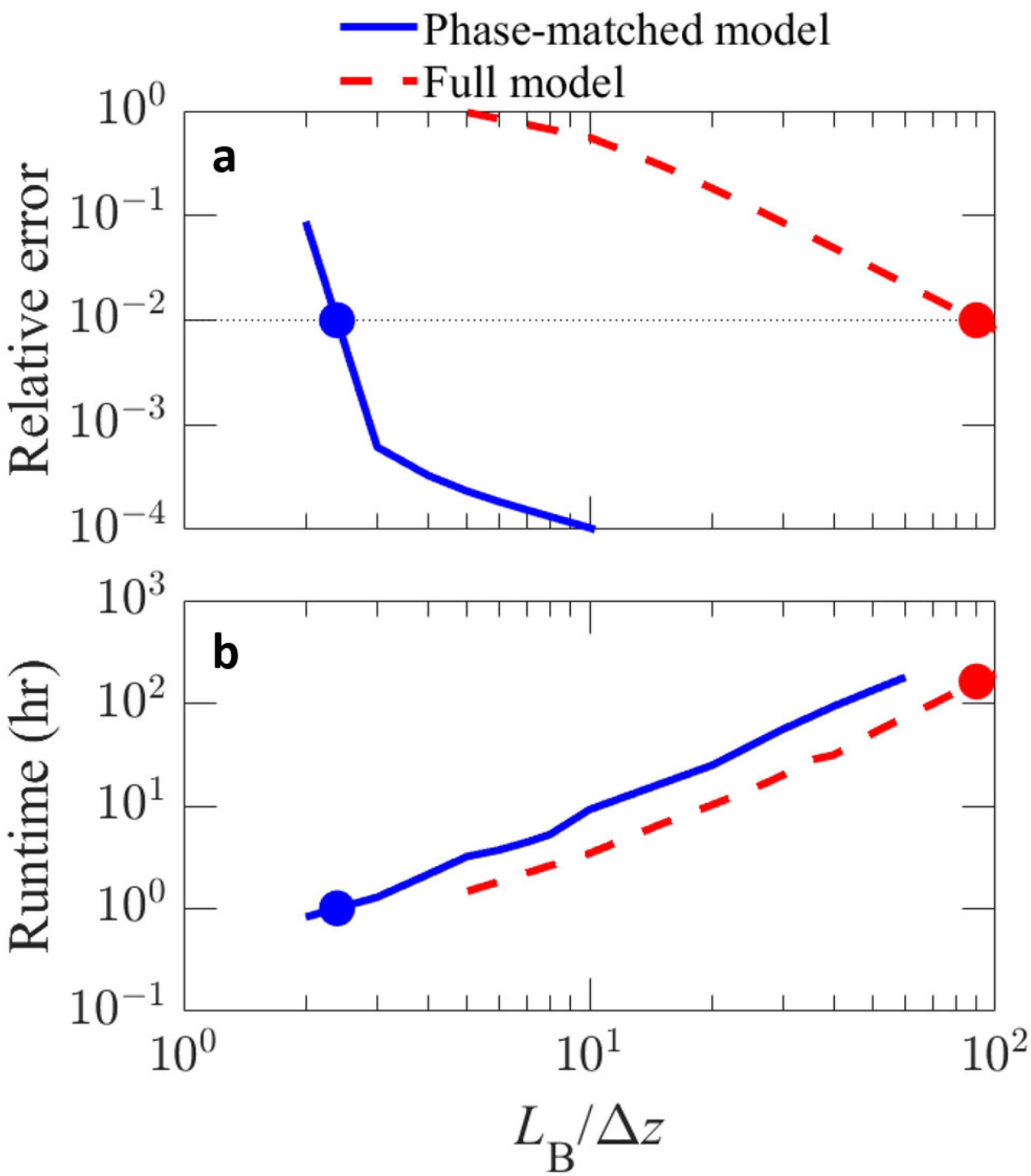

Figure 3.6: (a) Relative error vs. $L_B/\Delta z$ for the cases shown in Fig. 3.4. (b) Runtime vs. $L_{\mathrm{B}}/\Delta z$. The runtime for the phase-matched model is approximately twice as long as the runtime for the full model. Dots indicate the corresponding runtime with a relative error of 1%, as shown in (a). [Reprinted/Adapted] with permission from [80] © Optica Publishing Group.

approximately twice as the runtime for the full model, which is consistent with the greater computational load per step in the phase-matched model. When we compare the runtime corresponding to a relative error of 1%, shown with dots, we found a runtime of 163 hours for the full model and 1.17 hours for the phase-matched model, indicating that the phase-matched model runs a factor of 139 faster in this case. While we obtain a speedup of 139 in our study, this number will vary with different simulation parameters. Nevertheless, the advantage of using phase-matched model is clear.

3.4 TMI as an STRS process

The identification of TMI as an STRS process has remained somewhat controversial due to the complexity of TMI. Here, we will briefly argue in favor of this identification in the limit where the phase-matched model holds. We then point out some of the similarities and differences with the instability due to stimulated Brillouin scattering (SBS), which is another important effect limiting the performance of high-energy fiber laser amplifiers [106].

Rayleigh scattering is commonly observed as a spontaneous process. It is well known as the reason the sky is blue [107] and imposes a fundamental loss limit on optical fiber transmission [108]. It also imposes a fundamental limit on fiber interferometers and hence on opto-electronic oscillators [109].

Observation of STRS has proved more elusive, particularly in optical fibers. Zhu et al. [110] reported an observation of STRS in 2010, and Kong et al. [93] reported an observation of STRS in 2016. It is difficult to observe directly, and another observation that was reported in 2012 [111] was later shown to be incorrect [112].

STRS and SBS can be treated together theoretically because both are due to density fluctuations [101]. Rayleigh scattering is driven by isobaric processes, while Brillouin scattering is driven by isentropic processes. Both are three-wave scattering processes in which two optical fields couple to density fluctuations. When Eq. (3.3) holds, it is evident that TMI can be treated as a three-wave scattering process in which two optical modes couple to density fluctuations and that this process is isobaric. Hence, it is reasonable to identify TMI as an STRS-driven process.

While both STRS and SBS are three-wave processes in which two optical modes couple to density fluctuations, there are important differences—particularly in optical fibers. Rayleigh scattering is often referred to as an inelastic process, but that is almost never strictly true. Energy and momentum conservation implies that there is typically a small frequency offset. In the case of TMI this offset is quite small—on the order of a few kilohertz [89–92]. This offset plays a critical role in driving the instability, but it lies well within the linewidth of the optical modes, which is typically on the order of 100 MHz. While there is a significant difference between the wavenumbers of the fundamental and higher-order modes, this difference is small compared to the wavenumber of both modes ($\Delta\beta/\beta \sim 10^{-5}$). Both modes propagate in the same direction, but have different mode profiles. By contrast, the two optical modes that become unstable due to SBS are both fundamental modes, but they propagate in opposite directions. As a consequence, the wavenumber offset equals twice the wavenumber of each of the optical modes. The frequency offset, which is given by (the acoustic velocity)$\times$(twice the wavenumber of the optical modes), is of 10–20 GHz and much larger than the linewidth of the optical modes. These differences can be traced to the fundamental physical difference between pressure fluctuations, which propagate, and entropy fluctuations, which do not.

3.5 Coupled-mode theory background for TMI

The standard coupled-mode equations in Ref. [95] have been used to successfully model the transverse mode instability (TMI). The equations have been derived in the book from Marcuse [97] for coupled mode theory. For the completeness of this chapter, we give a detailed step-to-step derivation for the coupled mode equations. We follow the steps from Marcuse [97] but provide more steps to serve as a tutorial to understand the coupled mode theory for the general audience.

For time-harmonic electromagnetic fields, the curl Maxwell's equations become

$$\nabla \times \mathbf{E} = -j\omega\mu_0\mathbf{H}, \tag{3.20a}$$

$$\nabla \times \mathbf{H} = j\omega\epsilon_0 n^2\mathbf{E}. \tag{3.20b}$$

Next we express the ∇ operator, $\mathbf{E}$, and $\mathbf{H}$, as the sum of transverse and longitudinal components.

$$\nabla = \nabla_\perp + \hat{\mathbf{z}}\partial/\partial\ z, \tag{3.21a}$$

$$\mathbf{E} = \mathbf{E}_\perp + \mathbf{E}_z, \tag{3.21b}$$

$$\mathbf{H} = \mathbf{H}_\perp + \mathbf{H}_z. \tag{3.21c}$$

We can express the curl of $\mathbf{E}$ and $\mathbf{H}$ as transverse and longitudinal components,

$$(\nabla \times \mathbf{E})_\perp = \nabla_\perp \times \mathbf{E}_z + \hat{\mathbf{z}} \times \partial\mathbf{E}_\perp/\partial\ z, \tag{3.22a}$$

$$(\nabla \times \mathbf{E})_z = \nabla_\perp \times \mathbf{E}_\perp, \tag{3.22b}$$

$$(\nabla \times \mathbf{H})_\perp = \nabla_\perp \times \mathbf{H}_z + \hat{\mathbf{z}} \times \partial\mathbf{H}_\perp/\partial\ z, \tag{3.22c}$$

$$(\nabla \times \mathbf{H})_z = \nabla_\perp \times \mathbf{H}_\perp, \tag{3.22d}$$

where the subscripts on the left hand side indicate the transverse or longitudinal component of the curl operator.

Using (3.22b) and (3.22d) with (3.20a) and (3.20b), we then find that

$$\mathbf{E}_z = \nabla_\perp \times \mathbf{H}_\perp(1/j\omega\epsilon_0 n^2), \tag{3.23a}$$

$$\mathbf{H}_z = \nabla_\perp \times \mathbf{E}_\perp(-1/j\omega\mu_0). \tag{3.23b}$$

Now we need to find $\mathbf{E}_\perp$ and $\mathbf{H}_\perp$, since the longitudinal components will automatically be found by (3.23a) and (3.23b). We use (3.21a), (3.21c), (3.22c), and (3.22d) to expand (3.20b)

$$\nabla_\perp \times \mathbf{H}_\perp + \nabla_\perp \times \mathbf{H}_z + \hat{\mathbf{z}} \times \frac{\partial\mathbf{H}_\perp}{\partial\ z} = j\omega\epsilon_0 n^2(\mathbf{E}_z + \mathbf{E}_\perp).$$

Using (3.23a), we obtain

$$\nabla_\perp \times \mathbf{H}_\perp + \nabla_\perp \times (\nabla_\perp \times \mathbf{E}_\perp)(-1/j\omega\mu_0) + \hat{\mathbf{z}} \times \frac{\partial \mathbf{H}_\perp}{\partial\ z} =$$
$$j\omega\epsilon_0 n^2 (\nabla_\perp \times \mathbf{H}_\perp (1/j\omega\epsilon_0 n^2) + \mathbf{E}_\perp),$$

or,

$$(-1/j\omega\mu_0)\nabla_\perp \times (\nabla_\perp \times \mathbf{E}_\perp) + \hat{\mathbf{z}} \times \frac{\partial \mathbf{H}_\perp}{\partial\ z} = j\omega\epsilon_0 n^2 \mathbf{E}_\perp. \tag{3.24a}$$

Similar procedure with (3.20a) yields

$$(1/j\omega\epsilon_0)\nabla_\perp \times (\nabla_\perp \times [1/n^2]\mathbf{H}_\perp) + \hat{\mathbf{z}} \times \frac{\partial \mathbf{E}_\perp}{\partial\ z} = -j\omega\mu_0 \mathbf{H}_\perp. \tag{3.24b}$$

To express the refractive index, we find

$$n = n(x, y, z). \tag{3.25}$$

We assume waves propagate in the z direction with

$$e^{-j\beta_\nu\ z}. \tag{3.26}$$

An ideal waveguide has an index that is independent of z such that

$$n_0 = n_0(x, y). \tag{3.27}$$

We then replace the index terms and the field relation in the z direction in (3.24a) and (3.24b) by using (3.26) and (3.27) and find equations for the transverse electric and magnetic field vectors,

$$(-1/j\omega\mu_0)\nabla_\perp \times (\nabla_\perp \times \boldsymbol{\mathcal{E}}_{\nu\perp}) - (j\beta_\nu)\hat{\mathbf{z}} \times \boldsymbol{\mathcal{H}}_{\nu\perp} = j\omega\epsilon_0 n_0^2 \boldsymbol{\mathcal{E}}_{\nu\perp}, \tag{3.28a}$$

$$(1/j\omega\epsilon_0)\nabla_\perp \times (\nabla_\perp \times [1/n_0^2]\boldsymbol{\mathcal{H}}_{\nu\perp}) - (j\beta_\nu)\hat{\mathbf{z}} \times \boldsymbol{\mathcal{E}}_{\nu\perp} = -j\omega\mu_0 \boldsymbol{\mathcal{H}}_{\nu\perp}, \tag{3.28b}$$

where $\boldsymbol{\mathcal{E}}_{\nu\perp}$ and $\boldsymbol{\mathcal{H}}_{\nu\perp}$ are the transverse mode profiles and ν labels the mode number.

We now rewrite (3.23a) and (3.23b) for each transverse mode,

$$\boldsymbol{\mathcal{E}}_{\nu z} = \nabla_\perp \times \boldsymbol{\mathcal{H}}_{\nu\perp}(1/j\omega\epsilon_0 n^2), \tag{3.29a}$$

$$\boldsymbol{\mathcal{H}}_{\nu z} = \nabla_\perp \times \boldsymbol{\mathcal{E}}_{\nu\perp}(-1/j\omega\mu_0). \tag{3.29b}$$

We can use a series expansion of the transverse mode vectors as the sum of guided modes and radiation modes

$$\mathbf{E}_\perp = \sum_{\nu=1}^{N} a_\nu \boldsymbol{\mathcal{E}}_{\nu\perp} + \sum \int_0^\infty a_p \boldsymbol{\mathcal{E}}_{p\perp} dp, \tag{3.30a}$$

$$\mathbf{H}_\perp = \sum_{\nu=1}^{N} b_\nu \boldsymbol{\mathcal{H}}_{\nu\perp} + \sum \int_0^\infty b_p \boldsymbol{\mathcal{H}}_{p\perp} dp. \tag{3.30b}$$

We then disregard the coupling to radiation modes to simplify the above notation and use

$$\mathbf{E}_\perp = \sum_\nu a_\nu \boldsymbol{\mathcal{E}}_{\nu\perp}, \tag{3.31a}$$

$$\mathbf{H}_\perp = \sum_\nu b_\nu \boldsymbol{\mathcal{H}}_{\nu\perp}. \tag{3.31b}$$

We now substitute the field expressions in (3.31a) and (3.31b) into the differential equations (3.24a) and (3.24b) which gives

$$(-1/j\omega\mu_0)\nabla_\perp \times (\nabla_\perp \times \sum_\nu a_\nu \boldsymbol{\mathcal{E}}_{\nu\perp}) + \hat{\mathbf{z}} \times \frac{\partial \sum_\nu b_\nu \boldsymbol{\mathcal{H}}_{\nu\perp}}{\partial z} = j\omega\epsilon_0 n^2 \sum_\nu a_\nu \boldsymbol{\mathcal{E}}_{\nu\perp}.$$

We can further rearrange the above equation, which gives

$$\sum_\nu \{a_\nu(-1/j\omega\mu_0)\nabla_\perp \times (\nabla_\perp \times \boldsymbol{\mathcal{E}}_{\nu\perp}) + (\partial b_\nu/\partial z)\hat{\mathbf{z}} \times \boldsymbol{\mathcal{H}}_{\nu\perp} - j\omega\epsilon_0 n^2 a_\nu \boldsymbol{\mathcal{E}}_{\nu\perp}\} = 0, \tag{3.32a}$$

and similarly,

$$(1/j\omega\epsilon_0)\nabla_\perp \times (\nabla_\perp \times [1/n^2] \sum_\nu b_\nu \boldsymbol{\mathcal{H}}_{\nu\perp}) + \hat{\mathbf{z}} \times \frac{\partial \sum_\nu a_\nu \boldsymbol{\mathcal{E}}_{\nu\perp}}{\partial z} = -j\omega\mu_0 \sum_\nu b_\nu \boldsymbol{\mathcal{H}}_{\nu\perp},$$

or,

$$\sum_{\nu}\{b_\nu(1/j\omega\epsilon_0)\nabla_\perp\times(\nabla_\perp\times[1/n^2]\boldsymbol{\mathcal{H}}_{\nu\perp})+(\partial a_\nu/\partial z)\hat{\mathbf{z}}\times\boldsymbol{\mathcal{E}}_{\nu\perp}-j\omega\mu_0 b_\nu\boldsymbol{\mathcal{H}}_{\nu\perp}\}=0. \tag{3.32b}$$

Multiplying (3.28a) by a_ν, and adding the term $(\partial b_\nu/\partial z)\hat{\mathbf{z}}\times\boldsymbol{\mathcal{H}}_{\nu\perp}$ to both sides yields

$$\begin{aligned}a_\nu(-1/j\omega\mu_0)\nabla_\perp\times(\nabla_\perp\times\boldsymbol{\mathcal{E}}_{\nu\perp})-a_\nu(j\beta_\nu)\hat{\mathbf{z}}\times\boldsymbol{\mathcal{H}}_{\nu\perp}+(\partial b_\nu/\partial z)\hat{\mathbf{z}}\times\boldsymbol{\mathcal{H}}_{\nu\perp}=\\ a_\nu j\omega\epsilon_0 n_0^2\boldsymbol{\mathcal{E}}_{\nu\perp}+(\partial b_\nu/\partial z)\hat{\mathbf{z}}\times\boldsymbol{\mathcal{H}}_{\nu\perp}.\end{aligned}$$

Rearranging the above equation yields

$$\begin{aligned}a_\nu(-1/j\omega\mu_0)\nabla_\perp\times(\nabla_\perp\times\boldsymbol{\mathcal{E}}_{\nu\perp})+(\partial b_\nu/\partial z)\hat{\mathbf{z}}\times\boldsymbol{\mathcal{H}}_{\nu\perp}=\\ a_\nu j\omega\epsilon_0 n_0^2\boldsymbol{\mathcal{E}}_{\nu\perp}+[a_\nu(j\beta_\nu)+(\partial b_\nu/\partial z)]\hat{\mathbf{z}}\times\boldsymbol{\mathcal{H}}_{\nu\perp}.\end{aligned} \tag{3.33}$$

Substituting (3.33) into (3.32a) gives us

$$\sum_{\nu}\{[a_\nu(j\beta_\nu)+(\partial b_\nu/\partial z)]\hat{\mathbf{z}}\times\boldsymbol{\mathcal{H}}_{\nu\perp}-j\omega\epsilon_0(n^2-n_0^2)a_\nu\boldsymbol{\mathcal{E}}_{\nu\perp}\}=0. \tag{3.34a}$$

A similar procedure by multiplying (3.28b) by b_ν, subtracting the term $(\partial a_\nu/\partial z)\hat{\mathbf{z}}\times\boldsymbol{\mathcal{E}}_{\nu\perp}$ from both sides, and substituting the result into (3.32b) yields

$$\sum_{\nu}\{[b_\nu(j\beta_\nu)+(\partial a_\nu/\partial z)]\hat{\mathbf{z}}\times\boldsymbol{\mathcal{E}}_{\nu\perp}+(1/j\omega\epsilon_0)b_\nu\nabla_\perp\times(\nabla_\perp\times[n^{-2}-n_0^{-2}]\boldsymbol{\mathcal{H}}_{\nu\perp})\}=0. \tag{3.34b}$$

Next, we take the scalar product of (3.34a) with $\boldsymbol{\mathcal{E}}^*_{\mu\perp}$ then integrate over the infinite cross-section

$$\iint\sum_{\nu}\{[a_\nu(j\beta_\nu)+(\partial b_\nu/\partial z)]\boldsymbol{\mathcal{E}}^*_{\mu\perp}\cdot\hat{\mathbf{z}}\times\boldsymbol{\mathcal{H}}_{\nu\perp}-j\omega\epsilon_0(n^2-n_0^2)a_\nu\boldsymbol{\mathcal{E}}^*_{\mu\perp}\cdot\boldsymbol{\mathcal{E}}_{\nu\perp}\}dxdy=0.$$

We can rearrange the above equation to yield:

$$\sum_{\nu}\{[a_\nu(j\beta_\nu)+(\partial b_\nu/\partial z)](-\beta_\nu\delta_{\nu\mu}/\mu_0\omega)\}=j\omega\epsilon_0\sum_{\nu}\iint(n^2-n_0^2)a_\nu\boldsymbol{\mathcal{E}}^*_{\mu\perp}\cdot\boldsymbol{\mathcal{E}}_{\nu\perp}dxdy,$$

where we use the normalization

$$\iint dxdy\ \hat{\mathbf{z}} \cdot [\boldsymbol{\mathcal{E}}_{\nu\perp} \times \boldsymbol{\mathcal{H}}^*_{\mu\perp}] = \beta_\nu \delta_{\nu\mu}/\mu_0\omega. \tag{3.35}$$

The only contribution on the left-hand side is under the condition when $\nu = \mu$ because of the Kronecker delta $\delta_{\nu\mu}$, so

$$[a_\mu(j\beta_\mu) + (\partial b_\mu/\partial z)](-\beta_\mu/\mu_0\omega) = j\omega\epsilon_0 \sum_\nu \iint (n^2 - n_0^2) a_\nu \boldsymbol{\mathcal{E}}^*_{\mu\perp} \cdot \boldsymbol{\mathcal{E}}_{\nu\perp} dxdy.$$

We can further rearrage terms and obtain

$$a_\mu(j\beta_\mu) + (\partial b_\mu/\partial z) = \sum_\nu \overline{K}_{\nu\mu} a_\nu, \tag{3.36a}$$

where

$$\overline{K}_{\nu\mu} = (\omega^2/j\beta_\mu c^2) \iint (n^2 - n_0^2) \boldsymbol{\mathcal{E}}^*_{\mu\perp} \cdot \boldsymbol{\mathcal{E}}_{\nu\perp}\ dxdy. \tag{3.36b}$$

Using the same procedure on (3.34b) with $\boldsymbol{\mathcal{H}}^*_{\mu\perp}$, then integrating over the infinite cross-section, we find

$$b_\mu(j\beta_\mu) + (\partial a_\mu/\partial z) = \sum_\nu \overline{k}_{\nu\mu} b_\nu, \tag{3.37a}$$

where

$$\overline{k}_{\nu\mu} = (-\mu_0/j\epsilon_0\beta_\mu) \iint \boldsymbol{\mathcal{H}}^*_{\mu\perp} \cdot \nabla_\perp \times [\nabla_\perp \times [(n^{-2} - n_0^{-2}) \boldsymbol{\mathcal{H}}_{\nu\perp}]]\ dxdy. \tag{3.37b}$$

The above equation (3.37b) appears with an awkward form. To simplify (3.37b), we substitute $\nabla_\perp \times \boldsymbol{\mathcal{H}}_{\nu\perp}$ by using (3.29a), which yields

$$\overline{k}_{\nu\mu} = (-\mu_0/j\epsilon_0\beta_\mu) \iint \boldsymbol{\mathcal{H}}^*_{\mu\perp} \cdot \nabla_\perp \times [(n^{-2} - n_0^{-2})(j\omega\epsilon_0 n_0^2) \boldsymbol{\mathcal{E}}_{\nu z}]\ dxdy.$$

With the plane-wave approximation and rearranging the refractive index terms, we obtain

$$\overline{k}_{\nu\mu} = (\omega/\epsilon_0\beta_\mu c^2)\iint (1/n^2)(n^2 - n_0^2)\boldsymbol{\mathcal{E}}_{\nu z}\cdot\nabla_\perp\times\boldsymbol{\mathcal{H}}^*_{\mu\perp}\ dxdy.$$

Substituting $\nabla_\perp\times\boldsymbol{\mathcal{H}}_{\nu\perp}$ with (3.29a) into the above expression again yields

$$\overline{k}_{\nu\mu} = (\omega/\epsilon_0\beta_\mu c^2)\iint (1/n^2)(n^2 - n_0^2)\boldsymbol{\mathcal{E}}_{\nu z}\cdot(-j\omega\epsilon_0 n_0^2)\boldsymbol{\mathcal{E}}^*_{\mu z}\ dxdy,$$

or,

$$\overline{k}_{\nu\mu} = (\omega^2/j\beta_\mu c^2)\iint (n_0^2/n^2)(n^2 - n_0^2)\boldsymbol{\mathcal{E}}^*_{\mu z}\cdot\boldsymbol{\mathcal{E}}_{\nu z}\ dxdy. \tag{3.38}$$

Now we consider the coupled mode equations (3.36a) and (3.37a) in the absence of coupling, so that $\overline{k}_{\nu\mu} = \overline{K}_{\nu\mu} = 0$. We take the z derivative of (3.37a) and insert it into (3.36a), and obtain

$$a_\mu(j\beta_\mu) - 1/(j\beta_\mu)\partial^2 a_\mu/\partial z^2 = 0,$$

or,

$$\partial^2 a_\mu/\partial z^2 + \beta_\mu^2 a_\mu = 0. \tag{3.39a}$$

Similar procedure of taking the z derivative of (3.36a) and inserting it into (3.37a) gives

$$\partial^2 b_\mu/\partial z^2 + \beta_\mu^2 b_\mu = 0. \tag{3.39b}$$

Equations (3.39a) and (3.39b) have solutions in the form

$$a_\mu = a_\mu^+ + a_\mu^-, \tag{3.40a}$$

$$b_\mu = a_\mu^+ - a_\mu^-, \tag{3.40b}$$

with

$$a_\mu^+ = c_\mu^+ e^{-j\beta_\mu z}, \tag{3.41a}$$

$$a_\mu^- = c_\mu^- e^{+j\beta_\mu z}. \tag{3.41b}$$

The term with $e^{-j\beta_\mu z}$ represents a wave traveling in the positive z direction and the term with $e^{+j\beta_\mu z}$ corresponds to a wave traveling in the negative z direction.

Next we substitute (3.40a) into (3.36a)

$$\frac{\partial}{\partial z}(a_\mu^+ - a_\mu^-) + j\beta_\mu(a_\mu^+ + a_\mu^-) = \sum_\nu \overline{K}_{\nu\mu}(a_\nu^+ + a_\nu^-).$$

We can group the terms in association with the same propagation direction and obtain

$$[\frac{\partial a_\mu^+}{\partial z} + j\beta_\mu a_\mu^+] - [\frac{\partial a_\mu^-}{\partial z} - j\beta_\mu a_\mu^-] = \sum_\nu \overline{K}_{\nu\mu}(a_\nu^+ + a_\nu^-). \tag{3.42a}$$

Similarly, substituting (3.40b) into (3.36b) and grouping common terms yields

$$[\frac{\partial a_\mu^+}{\partial z} + j\beta_\mu a_\mu^+] + [\frac{\partial a_\mu^-}{\partial z} - j\beta_\mu a_\mu^-] = \sum_\nu \overline{k}_{\nu\mu}(a_\nu^+ - a_\nu^-). \tag{3.42b}$$

Addition and subtraction of (3.42a) and (3.42a) finally yields

$$\frac{\partial a_\mu^+}{\partial z} = -j\beta_\mu a_\mu^+ + \frac{1}{2}\sum_\nu K_{\nu\mu}^{+,+} a_\nu^+ + K_{\nu\mu}^{+,-} a_\nu^-, \tag{3.43a}$$

$$\frac{\partial a_\mu^-}{\partial z} = j\beta_\mu a_\mu^- + \frac{1}{2}\sum_\nu K_{\nu\mu}^{-,-} a_\nu^- + K_{\nu\mu}^{-,+} a_\nu^+, \tag{3.43b}$$

with

$$K_{\nu\mu}^{p,q} = p\overline{K}_{\nu\mu} + q\overline{k}_{\nu\mu} = \omega^2/j\beta_\mu c^2 \iint [p\boldsymbol{\mathcal{E}}_{\mu\perp}^* \cdot \boldsymbol{\mathcal{E}}_{\nu\perp} + q(n_0^2/n^2)\boldsymbol{\mathcal{E}}_{\mu z}^* \cdot \boldsymbol{\mathcal{E}}_{\nu z}](n^2 - n_0^2)dxdy, \tag{3.43c}$$

where p or q are $(+)$ or $(-)$ as superscripts or $(+1)$ or (-1) as factors.

The terms $a_\mu^{+,-}$ rapidly oscillate. We introduce a slowly varying approximation by substituting (3.40a) into (3.43a). We also assume that coupling occurs only between forward propagating modes so that $c_\mu^- = 0$ which yields

$$\frac{\partial c_\mu^+ e^{-j\beta_\mu z}}{\partial z} = -j\beta_\mu c_\mu^+ e^{-j\beta_\mu z} + \frac{1}{2}\sum_\nu K_{\nu\mu}^{+,+} c_\nu^+ e^{-j\beta_\nu z},$$

or,

$$\frac{\partial c_\mu^+}{\partial z} e^{-j\beta_\mu z} - j\beta_\mu c_\mu^+ e^{-j\beta_\mu z} = -j\beta_\mu c_\mu^+ e^{-j\beta_\mu z} + \frac{1}{2}\sum_\nu K_{\nu\mu}^{+,+} c_\nu^+ e^{-j\beta_\nu z}.$$

After canceling the common term, we obtain

$$\frac{\partial c_\mu^+}{\partial z} = \frac{1}{2}\sum_\nu K_{\nu\mu}^{+,+} c_\nu^+ e^{j(\beta_\mu - \beta_\nu)z}. \tag{3.44}$$

All the above equation derivations follow the main steps from [97]. We now relabel variables to obtain the expression used in [80, 95]

$$c^+ \to A, \mu \to l, \nu \to m, \beta_\mu \to -\beta_l, \beta_\nu \to -\beta_m, dxdy \to d^2\mathbf{r}_\perp.$$

Now equation (3.44) becomes

$$\frac{\partial A_l}{\partial z} = \frac{j\omega^2}{2\beta_l c^2}\sum_m \int d^2\mathbf{r}_\perp (n^2 - n_0^2)[\boldsymbol{\mathcal{E}}_{l\perp}^* \cdot \boldsymbol{\mathcal{E}}_{m\perp} + (n_0^2/n^2)\boldsymbol{\mathcal{E}}_{lz} \cdot \boldsymbol{\mathcal{E}}_{mz}] e^{j(\beta_m - \beta_l)z}. \tag{3.45}$$

We find that $(n^2 - n_0^2) \approx 2n_0\Delta n$, with $\Delta n = n - n_0$. We also limit our study to just one fundamental mode and one higher-order mode, and the other longitudinal mode is neglected. We let $\Delta\beta = \beta_0 - \beta_1, \beta_0 \approx \beta_1 \equiv \beta$. The coupled mode equations for a fundamental mode and single higher-order mode (HOM) become

$$\frac{\partial A_0}{\partial z} = \frac{j\omega^2}{\beta c^2}\int d^2\mathbf{r}_\perp (n_0\Delta n)[|\boldsymbol{\mathcal{E}}_0|^2 A_0^2 + \boldsymbol{\mathcal{E}}_0^* \cdot \boldsymbol{\mathcal{E}}_1 A_1 e^{-j\Delta\beta z}], \tag{3.46a}$$

$$\frac{\partial A_1}{\partial z} = \frac{j\omega^2}{\beta c^2}\int d^2\mathbf{r}_\perp (n_0\Delta n)[|\boldsymbol{\mathcal{E}}_1|^2 A_1^2 + \boldsymbol{\mathcal{E}}_1^* \cdot \boldsymbol{\mathcal{E}}_0 A_0 e^{+j\Delta\beta z}], \tag{3.46b}$$

where in this case A_0 and A_1 are the amplitudes for the fundamental and HOM.

3.6 Conclusions and discussion

In this work, we derived the three-wave mixing equations that govern TMI in the limit where a single higher-order mode is present, and the longitudinal rate of change of all quantities is slow compared to the beat length. This limit normally applies in practice. In this limit, TMI can be identified as an STRS process, and we reviewed the theoretical justification for this identification in the appendix, where we also discussed similarities and differences between STRS and SBS in the Appendix. There, we verified the accuracy of the phase-matched model in a Yb^{3+}-doped fiber amplifier with a relatively simple step index profile. The amplifier that we considered is like that of Naderi et al. [95], but has a more realistic 10-m length. We demonstrated that this model reproduces the nonlinear saturation of the higher-order mode and the instability threshold that are predicted by the full model. We demonstrated a computational speedup that is more than a factor of 100.

We derived the three-wave mixing equations in the case that a single higher-order mode is present, but we expect this result to be more broadly applicable when several higher-order modes are present. In the linear limit below threshold when HOMs have low power, HOMs will only interact with the fundamental mode. In that case, the three-wave mixing equations can be extended by adding a new set of equations for the index of refraction, Yb^{3+} population density, heat, temperature, and optical mode amplitude for each of the HOMs. The computational complexity scales proportional to M, where M is the number of modes. More generally, we anticipate that the three-wave mixing equations can be extended to include a coupling between all the modes as long as none of the beat lengths between any of mode pairs becomes large enough to be comparable to the scale length on which any of the amplitudes change. However, the computational complexity grows proportional to M^2, and higher-order nonlinear interactions with a slowly varying amplitude could invalidate this approach.

CHAPTER FOUR

Piecewise Parabolic Phase Modulation for BI Suppression

This chapter published as [19]: J. White, J. T. Young, C. Wei, J. Hu, and C. R. Menyuk, "Seeding fiber amplifiers with piecewise parabolic phase modulation for high SBS thresholds and compact spectra," Opt. Express **27**(3), 2962–2974 (2019).

In this chapter, we study phase modulation techniques for the suppression of the Brillouin instability (BI). We propose using piecewise parabolic phase modulation of the seed laser for suppressing BI in a fiber amplifier. A 9 m passive fiber is used in simulation. Compared with random phase modulation and 0-π pseudo-random phase modulation, the piecewise parabolic phase waveform yields a higher SBS threshold per unit bandwidth. If the bandwidth is defined as the range of frequencies containing 85% of the total power, the threshold for parabolic phase modulation is 1.4 times higher than the threshold for the five- or seven-bit pseudo-random modulation format. If the bandwidth is defined more tightly, e.g., the range of frequencies containing 95% of the total power, the threshold for parabolic phase modulation is three times higher. For both cases, achieving a bandwidth of 1.5 GHz requires a maximum phase shift of 30 radians.

4.1 Phase modulation as a suppression technique

Narrow-linewidth, high-power fiber amplifiers are needed for both coherent and incoherent beam combining or for spectral combining of multiple amplifiers. For coherent beam combining, a narrower linewidth improves combining efficiency in the presence of path length mismatch [113], allows higher angle beam steering, and enables better wavefront predistortion [114]. For the type of spectral beam combining in which a grating is the output coupler, a narrower linewidth reduces the output beam spreading due to diffraction. A larger number of parallel amplifiers can also be accommodated under the fiber gain spectrum, allowing higher powers to be reached. However, narrow linewidths lower the threshold for stimulated Brillouin scattering (SBS). This trade-off has led to a search for seed spectra that allow the highest threshold per unit bandwidth.

Pseudo-random bit sequence (PRBS) waveforms have a power spectrum with an envelope that is approximately sinc^2, and random phase modulation waveforms typically have a Gaussian spectrum. Many lasers tend to exhibit a random walk in phase, leading to a Lorentzian spectrum. The optimum shape for spectral combining is rectangular. Nearly rectangular spectra can be obtained with linearly-chirped seeds with sawtooth or triangular frequency waveforms, i.e., a phase that is piecewise parabolic in time. This chapter explores the suitability of chirped seeds with modulation periods in a range that covers the characteristic times given by the phonon lifetime and the fiber transit time. For a given spectral bandwidth, we will show how the threshold for sawtooth and triangular frequency waveforms depends on the period, and compare to the results for PRBS, random phase, and random-walk phase modulation.

SBS mitigation in a high-power amplifier has been achieved by engineering the fiber and by modulating the laser beam introduced into the amplifier as a seed. Random phase modulation of a narrow band laser has been realized by applying a white noise generator to an external electro-optic phase modulator [115–118]. More recently, PRBS waveforms with π phase shifts have been extensively investigated for SBS mitigation [119, 120]. A comprehensive theoretical study showed that "for a fiber length of length 9 m the patterns at or near n = 7 provide the best mitigation of SBS with suppression factors approaching 17 dB at a modulation frequency of 5 GHz" [17]. We will use those results as a benchmark for comparison to the waveforms we propose.

A frequency chirp of 1.2 $\times$ 1018 Hz/s has previously been used to suppress SBS in an 8.4 ns pulsed fiber amplifier [121]. A discontinuous frequency chirp (consisting of a succession of 30-MHz jumps) and a low-pass-filtered white noise source have also been used to suppress SBS in a high-gain parametric fiber amplifier [23]. A chirp with a period much longer than the fiber transit time has been used in an amplifier with a 25 m final stage to achieve a fundamental-mode pump-limited output of 1.6 kW [122]. For coherent combining, this waveform has the advantage that path length differences can be compensated with an acousto-optic frequency shifter [123]. The other significant advantage is that it is expected to yield fiber-length-independent SBS thresholds [124]. However, the techniques used to obtain μs-ms period chirps with 1-100-nm-wide spectra [125, 126] may not be applicable to the 10-100 ns period chirps with the sub-nm spectra that are desirable for spectral beam combining.

More sophisticated waveforms can be generated with a nonlinear algorithm that varies the phase at every point in time in order to minimize a cost function based on the difference between the resulting and ideal spectra [127]. The waveform can be programmed into an arbitrary waveform generator and used to drive an electro-optic modulator. This technique has been used to impress a 2-GHz-wide flat spectrum with between 16 and 380 discrete lines onto a seed, allowing amplification to 300 W [128]. Fringe visibility was also measured in a coherent combination experiment, and compared to standard- and filtered-PRBS modulation. Crosstalk between neighboring frequencies puts a limit on how closely the lines can be spaced, and thus the flatness of the spectrum. Crosstalk is not an issue with a swept-frequency source because the frequencies are not all present at the same time and position within the fiber.

The most recent work in this direction uses a model that includes the cross-interactions between spectral lines [129]. It also uses a genetic-algorithm-based Pareto multi-objective nonlinear optimization to minimize the Brillouin Stokes power and minimize the laser linewidth. The sawtooth and the triangle frequency chirp that we propose both have a phase that is piecewise parabolic in time (Fig. 4.1). These waveforms are comparatively simple and therefore can be generated without sophisticated algorithms and electronics. SBS threshold for a passive fiber is commonly taken to be a ratio of $10 - 2$ between the time-averaged backward Stokes power and the incident laser power, both measured at the fiber entrance ($z = 0$). For purposes of comparing different modulation formats, the exact definition of threshold should not play a large role.

Comparing spectra of different shapes requires a definition of spectral width. We define it as the range of frequencies that encompass a given fraction of the total power. (The spectra we consider are nominally symmetric, so the range will be centered on the mean frequency.) A commonly used fraction is 85%.

Future systems, or different applications, e.g., close spectral packing of amplifiers, may require a tighter standard, e.g., 90% or 95%. This could also be the case for spectral beam combining systems in which the extraneous power, propagating at a large diffraction angle, causes a problem in the far field and therefore has to be dissipated internally before it reaches the exit aperture. Another consideration is how much of the light is useful when it reaches the far field or the focal plane of a lens. It is necessary to weigh whether it is more useful to have the extraneous 15% packed tightly against the other 85%, or distributed over a wide frequency range. Considerations such as these could give rise to a tighter definition of bandwidth in practice. Therefore, we consider spectral widths of 85%, 90%, and 95% power to illustrate the difference between the following spectra: Lorentzian (arising from a random phase walk), Gaussian (arising from a random phase), sinc^2 (arising from a PRBS waveform), and nearly rectangular (arising from either a sawtooth or triangular frequency chirp). We consider the case where the entire seed spectrum is incident upon the fiber, although in some experiments the extraneous spectral components could be filtered before entering the fiber. Figure 4.2 shows the five spectra, normalized to have the same total power and the same 85% width. The spectrum in the fourth row is from one period of a triangle chirp waveform with the period equal to twice the transit time of a 9 m fiber, i.e., 87 ns [130]. The chirp amplitude is adjusted to give the correct 85% bandwidth. The spectrum in the fifth row is the raw Fourier transform of one period of a sawtooth chirp waveform with an 87 ns period.

Within the 85% width, the Lorentzian clearly has the most variation, the Gaussian and sinc^2 have substantially less variation, and the spectrum of the sawtooth chirp or

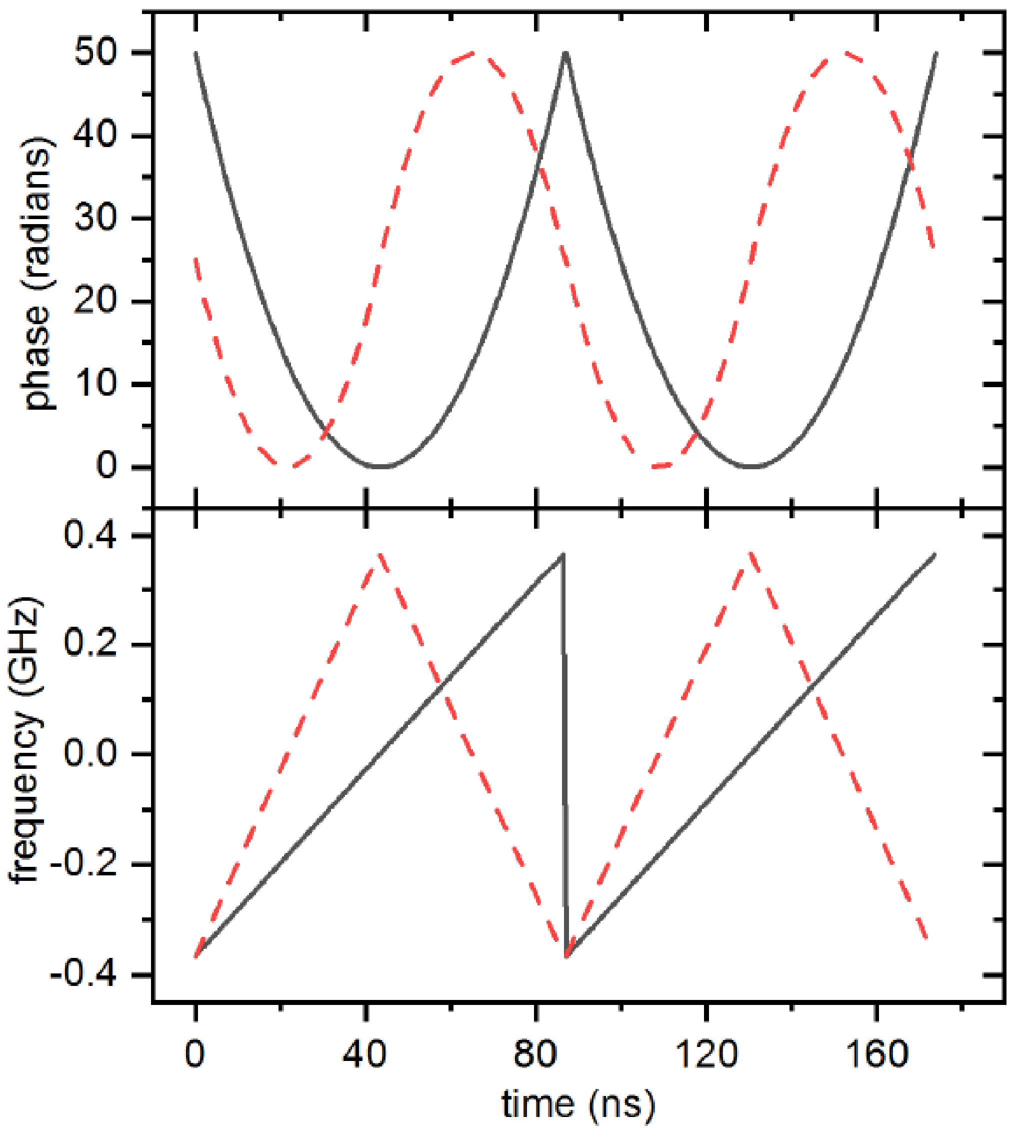

Figure 4.1: Phase (above) as a function of time, and frequency (below) as a function of time for the sawtooth (solid line) and triangle (dashed line) frequency chirp. [Reprinted/Adapted] with permission from [19] © Optica Publishing Group.

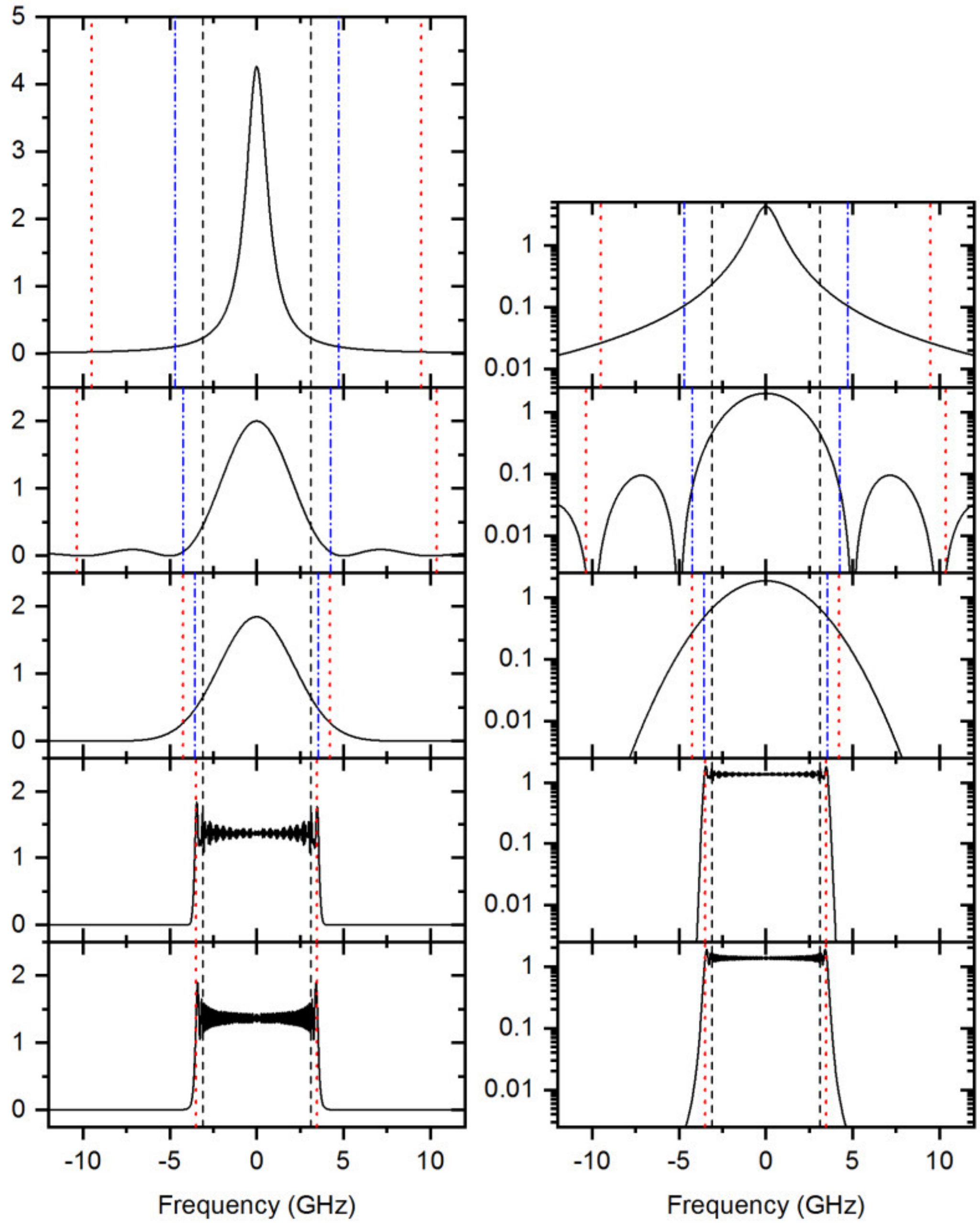

Figure 4.2: Frequency spectra associated with (1st row) a random phase walk (Lorentzian), (2nd row) a 0-π generic PRBS waveform (sinc^2), (3rd row) random frequency modulation (Gaussian), (4th row) one period of a triangle chirp, and (5th row) one period of a sawtooth chirp. Plots in the left (right) column have a linear (log) vertical axis. The log scales all show three orders of magnitude variation. All spectra are normalized to have a total power of one and the same 85% width. The 90% (blue) and 95% (red) widths are also shown. The 90% width is omitted from the last rows. [Reprinted/Adapted] with permission from [19] © Optica Publishing Group.

the smoothed triangle chirp have even less. Given the nonlinear nature of the SBS, less variation in the seed spectrum raises the threshold.

As mentioned above, the spectral distribution of the out-of-band 15% also has practical implications. Spreading it over a wide range of frequencies, as with the Lorentzian and sinc^2 spectra, may lower the threshold, but also reduce by 15% the impact of the output beam at the target or sample, and create other problems. Thus there are application-specific tradeoffs to be considered, in addition to the threshold. Also shown in Fig. 4.2 are the 90% and 95% bandwidths. For the Lorentzian and sinc^2 spectra, these widths are substantially larger than the 85% widths, but for the rectangular spectra, they are only marginally wider.

4.2 Theoretical model and parameters

We model the SBS following previous treatments that solve the coupled first order equations representing propagation of the laser and Stokes wave, buildup of the acoustic wave, and initiation from a Langevin noise source representing thermal phonons throughout the length of the fiber [131]. Our code has been verified by comparison with experiments and previous theoretical work [17, 122, 124].

There are many parameters involved in even a basic simulation of SBS in a fiber amplifier. Some choices will favor one modulation format, other choices may favor another, so it is hard to draw universal conclusions about the relative merit. We analyze a passive fiber, and use parameters equal to those in [17], reproduced in Table 4.1.

While intensity is the fundamental quantity, thresholds will be reported on the basis of power coupled into a 10 μm core fiber, for a direct comparison to [17]. There is no transverse spatial dependence in our calculation, i.e., it is a plane wave model, a standard approximation for a fiber with only the fundamental mode present.

Our 9 m fiber length corresponds to a 7 m active fiber, which would typically absorb 95% of a 976 nm pump beam, and a 2 m delivery fiber. Of course, the longitudinal dependence of the intensity in our simulation is quite different from that of an amplifier with 20 dB of gain. Since gain in the active fiber adds another degree of freedom in the comparison, we model a passive fiber in this chapter, consistent with [17].

4.3 Power threshold for different modulation schemes

As a function of incident power, the backward Stokes power increases rapidly around the threshold value, later saturating as the reflectivity approaches one. The data for six waveforms with the same 85% bandwidth are shown in Fig. 4.3. The sawtooth and triangle waveforms have a period of 23 ns. The thresholds are shown by the intersection with the dashed line.

For a signal with a linewidth much narrower than the Brillouin linewidth and the inverse of the fiber transit time, the threshold is 2.4 W. This value will be used to normalize the other thresholds. The normalized threshold for sawtooth and triangle waveforms has a broad peak ranging from a period of $1/\Delta\nu_B = 2\pi\tau$ to twice the fiber

Table 4.1. BI simulation parameters

silica density	ρ_0	2201 kg/m^3
optical angular freq.	ω	1.77×10^{15} rad/s
electrostrictive constant	γ_{e}	1.95
refractive index	n	1.5
temperature	T	300 K
sound velocity	ν_{s}	5.9×10^3 m/s
fiber core area	A	7.85×10^{-11} m^2
Brillouin angular freq.	Ω_{B}	10.1×10^10 rad/s
fiber length	L	9 m
$2\pi\times$phonon lifetime	$2\pi\tau$	17.5 ns

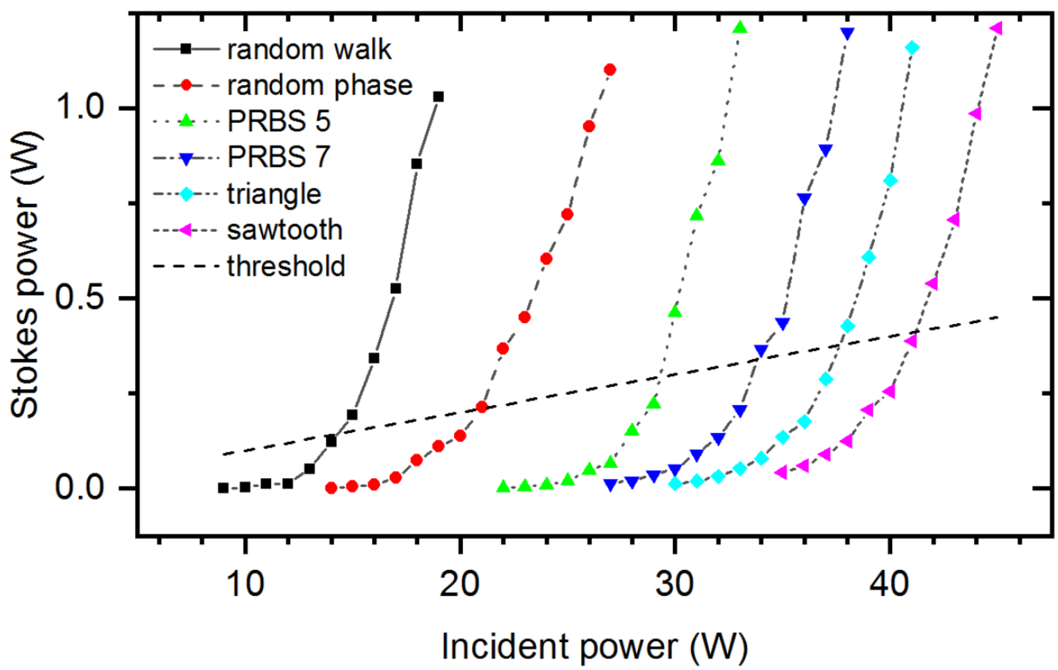

Figure 4.3: Backward Stokes power vs. incident laser power for waveforms with 85% bandwidths of 1.5 GHz (left to right): random walk phase, random phase, PRBS 5, PRBS 7, triangle chirp, sawtooth chirp. The latter two have a period of 23 ns. [Reprinted/Adapted] with permission from [19] © Optica Publishing Group.

transit time (Fig. 4.4). The three characteristic times are indicated with vertical lines. The thresholds for a random walk, a random phase, PRBS 5, and PRBS 7 are also shown for reference. For an 85% bandwidth equal to 1.5 GHz, the normalized threshold for the sawtooth waveform has a maximum of 16, achieved at a period of 23 ns, or $1.3/\Delta\nu_B$, and a maximum phase shift of 32 radians (Fig. 4.4). A second peak appears at a period of 95 ns, or $2nL/c$. No additional peaks appear at longer periods. The peak at 23 ns is of more practical interest because of the smaller required phase shifts. When compared on the basis of 85% bandwidths, the sawtooth chirp at the optimum period has a threshold 23% higher than PRBS 7, 44% higher than PRBS 5, 1.9 $\times$ higher than random phase modulation, and 3.0 $\times$ higher than a random walk phase.

The data for a 1.5 GHz bandwidth defined by the (tighter) 90% power criterion show a 4-6% decrease in threshold for the linear chirps, a 16-17% drop for the random

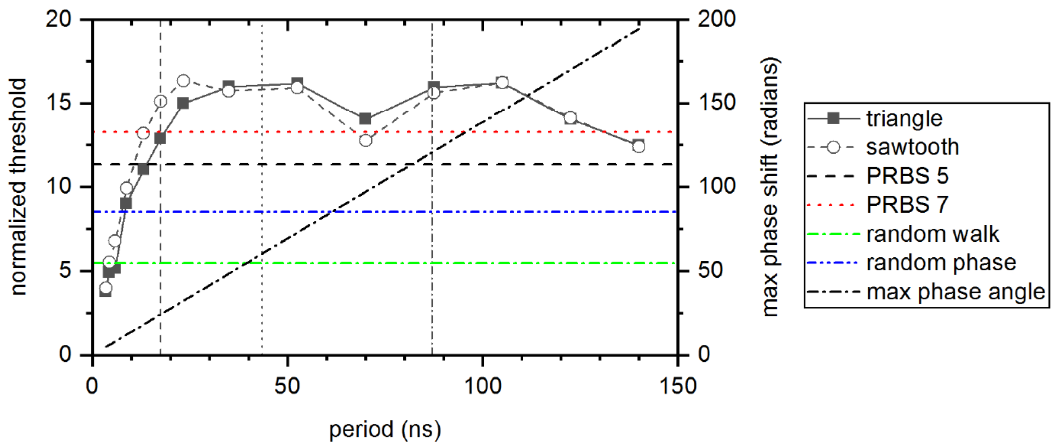

Figure 4.4: Normalized threshold vs. the period, for the following waveforms: sawtooth frequency chirp, triangle frequency, PRBS 5, PRBS 7, random walk in phase, and random phase. All have an 85% bandwidth of 1.5 GHz. (Right axis) Maximum phase shift required for the chirped waveforms. Also indicated are 2π times the phonon lifetime, fiber transit time (43 ns), and round trip time. [Reprinted/Adapted] with permission from [19] © Optica Publishing Group.

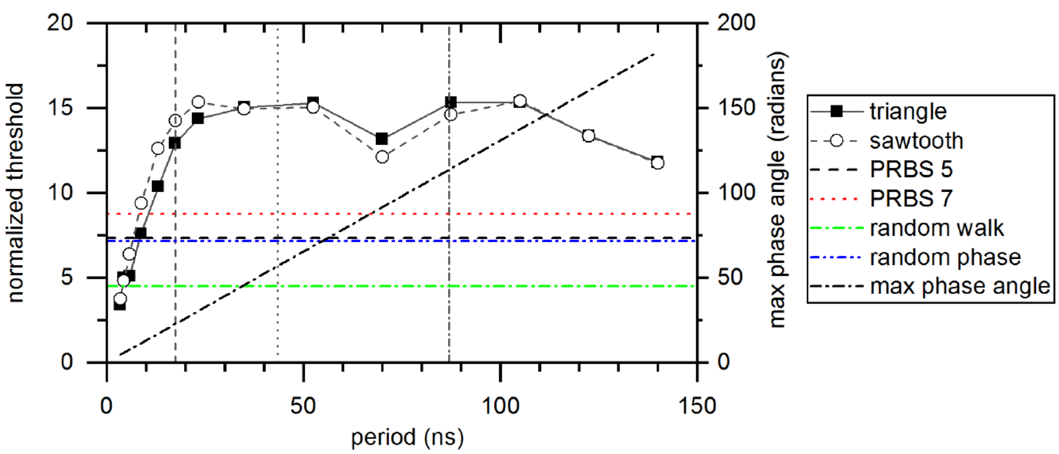

Figure 4.5: Normalized threshold vs. the period for the same waveforms, with a 90% bandwidth of 1.5 GHz. (Right axis) Maximum phase shift required for the chirped waveforms. [Reprinted/Adapted] with permission from [19] © Optica Publishing Group.

walk and random phase, and a 33% decrease for the PRBS (Fig.4.5). At the optimum period of 23 ns, the sawtooth waveform has a threshold 75% higher than the PRBS waveforms, and 31 radians are required. Note that the random phase and PRBS 5 have nearly the same threshold.

The data for a 1.5 GHz bandwidth defined by the 95% power criterion show further small threshold decreases for the linear chirps, and large decreases for the

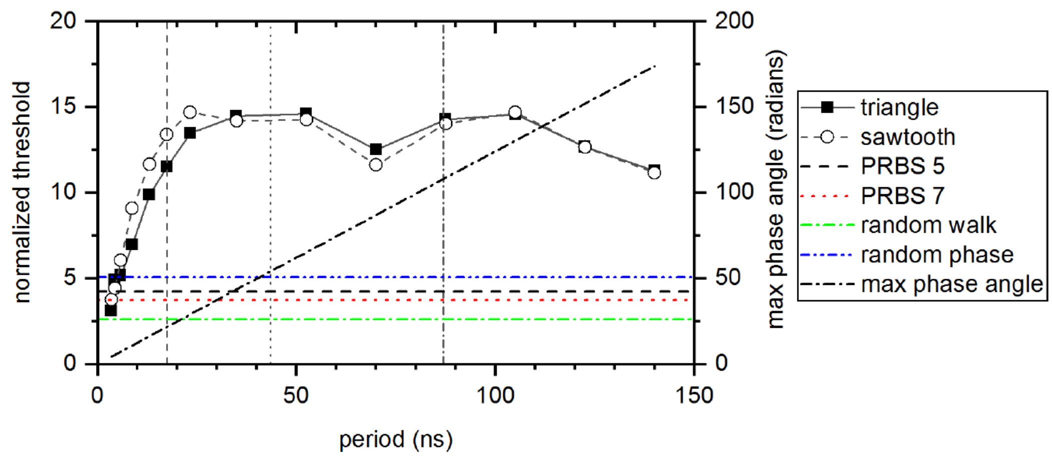

Figure 4.6: Normalized threshold vs. the period for the same waveforms with a 95% bandwidth of 1.5 GHz. (Right axis) Maximum phase shift required for the chirped waveforms. [Reprinted/Adapted] with permission from [19] © Optica Publishing Group.

other formats. At a period of 23 ns, the sawtooth waveform has a threshold that is $3.5\times$ larger than the PRBS 5 waveform, and 29 radians are required. With this definition of bandwidth, the random phase modulation has a higher threshold than either of the two PRBS waveforms (Fig. 4.6).

4.4 Discussion

For piecewise-parabolic phase waveforms, the threshold is relatively constant for periods ranging from 20 to 100 ns. The threshold decrease at long periods has a macroscopic origin. For periods longer than twice the fiber transit time, the Stokes wave originating at $z = L$ no longer encounters the entire seed bandwidth while propagating to $z = 0$. The threshold decreases at short periods because the stimulated phonons do not have time to sufficiently decay before they find themselves again in resonance with the laser-Stokes difference frequency. At short periods, the high fundamental Fourier component also means that the spectrum will be composed of harmonics spaced further apart, thus better resolved, putting more structure into the spectrum, thus lowering the threshold.

The optimal operating point for both the sawtooth and triangle waveforms is at a period of 23 ns. At this period, the maximum threshold has been achieved with a required phase shift of 30 radians, which will scale linearly with bandwidth. Increasing the period increases the required phase shift without increasing the threshold. The small differences in threshold between the triangle and sawtooth waveforms are reproducible, but the choice between sawtooth and triangle may come down to practical considerations other than threshold. For an experimental realization, the triangular waveform has the advantage of no large abrupt change in phase. The sawtooth waveform has the advantage of requiring a chirp that is half as large and has only one sign.

Future work could focus on electro-optic modulators capable of producing a 30 radian phase shift. The voltage applied to current waveguide e-o modulators is limited by the need to dissipate electrical power. Stringing multiple e-o modulators in series is limited by throughput, which is largely determined by the inefficiency of coupling the fundamental mode of the fiber pigtail to the fundamental mode of the waveguide, and vice versa. A potential solution is the lithium niobate on SiO_2 technology which allows long waveguides, CMOS-compatible driving voltages, and 70 Gbit s^{-1} data rates [132]. An alternative to large phase shifts and piecewise parabolic waveforms with 20-30 ns periods, is to reproduce the parabola modulo 2π. This shifts the practical difficulty to generating rapid 2π phase shifts at more frequent intervals.

4.5 Conclusions

For fiber amplifiers, seed lasers with piecewise parabolic phase waveforms, e.g., those produced by a sawtooth or triangular linear frequency chirp, offer a significantly higher SBS threshold, compared to the conventional random phase variation, and pseudo-random waveforms. The definition of bandwidth for spectra of qualitatively different shapes is shown to have a large influence on the relative thresholds. For example, at the 85% power definition, the PRBS waveforms have a threshold superior to that of the random phase. At the 95% power definition, the random phase has a higher threshold.

The trend in spectral beam combining toward squeezing more amplifiers under the Yb gain curve will favor the nearly rectangular spectra provided by the parabolic phase waveforms. Applications where the far-out-of-bandwidth power has to be dissipated will also benefit from the relatively compact rectangular spectrum.

Compared to binary waveforms, e.g., PRBS, coherent combination with piecewise parabolic and random phase waveforms will require tighter path length matching, due to their analog nature.

Practical implementation of the piecewise parabolic waveforms will depend on the development of electro-optic modulators with adequate throughput and capable of 30 radian phase shifts. Modulators producing more modest phase shifts could be used if the frequency response is sufficient to generate the same parabolic phase shift, modulo an integer multiple of 2π. If we compare the bandwidth required of the phase modulators, the piecewise parabolic waveforms require $5\times$ less modulator bandwidth than the PRBS waveforms, for a given spectral bandwidth.

CHAPTER FIVE

Tradeoff Between the Brillouin and Transverse Mode Instabilities

This chapter published as [133]: J. T. Young, A. J. Goers, D. M. Brown, M. L. Dennis, K. Lehr, C. Wei, C. R. Menyuk, and J. Hu, "Tradeoff Between the Brillouin and Transverse Mode Instabilities in Yb-doped Fiber Amplifiers," Opt. Express **30**(22), 40691–40703 (2022).

In this chapter, we formulate a model that includes the Brillouin instability (BI) and the transverse mode instability (TMI) in a single simulation. The BI due to stimulated Brillouin scattering (SBS) and the TMI due to stimulated thermal Rayleigh scattering (STRS) limit the achievable power in high-power lasers and amplifiers. The pump power threshold for BI increases as the core diameter increases, but the threshold for TMI may decrease as the core diameter increases. In this chapter, we use a multi-time-scale approach to simultaneously model BI and TMI, which gives us the ability to find the fiber diameter with the highest power threshold. We formulate the equations to compare the thresholds of the combined and individual TMI and BI models. At the pump power threshold and below, there is a negligible difference between the full and individual models, as BI and TMI are not strong enough to interact with each other. The highest pump threshold occurs at the optimal core size of 43 μm for the simple double-clad geometry that we considered. We found that both effects contribute equally to the threshold, and the full BI and TMI model yields a similar threshold as the BI or TMI model alone. However, once the reflectivity is sufficiently large, we find in the full BI and TMI model that BI may trigger TMI and reduce the TMI threshold to a value lower than is predicted in simulations with TMI alone. This result cannot be predicted by models that consider BI and TMI separately. Our approach can be extended to more complex geometries and used for their optimization.

5.1 Introduction

Stimulated Brillouin Scattering (SBS) and stimulated thermal Rayleigh scattering (STRS) can lead respectively to the Brillouin instability (BI) and the transverse mode instability (TMI) which limit the output power in optical fibers [3, 4, 134]. For BI, a forward-propagating optical mode couples to an acoustic mode and the same optical mode propagating in the backward direction (Stokes mode) [16, 17, 19, 119, 124, 135, 136]. For TMI, an optical mode couples to a higher-order mode (HOM) that has nearly the same frequency [2, 87–89, 94, 95, 137] and a transverse thermal mode. In both cases, the instability is characterized by exponential growth that leads to a sharp pump power threshold, beyond which significant power is transferred to modes other than the forward-propagating fundamental mode. Both instabilities impose limits on the output power of Yb^{3+}-doped fiber amplifiers, and the interaction between these two instabilities is not well understood. Also, the limits that they impose depend differently on the fiber core diameter. As the fiber core diameter increases, all else being equal, the BI threshold increases because the optical intensity decreases for a fixed power. However, as the fiber core diameter increases, the TMI threshold may decrease due to an increased interaction between the fundamental mode and the HOM. The wavenumbers of the HOMs at the same frequency come closer to the wavenumber of the fundamental mode, easing the coupling condition for the thermal mode so that TMI is more easily triggered. Thus, a tradeoff typically exists between BI and TMI as the diameter increases.

Figure 5.1 illustrates schematically the dependence of the pump power threshold for the individual BI and TMI effects. Using mitigation techniques for BI such as phase modulation [17, 19] will likely decrease the core diameter where both BI and TMI play a roughly equal role in limiting the pump power threshold. On the other hand, mitigation techniques for TMI, such as fiber bending [29, 138], fiber tapering [139], gain filtering [27], use of specially designed photonic crystal fibers [140], and

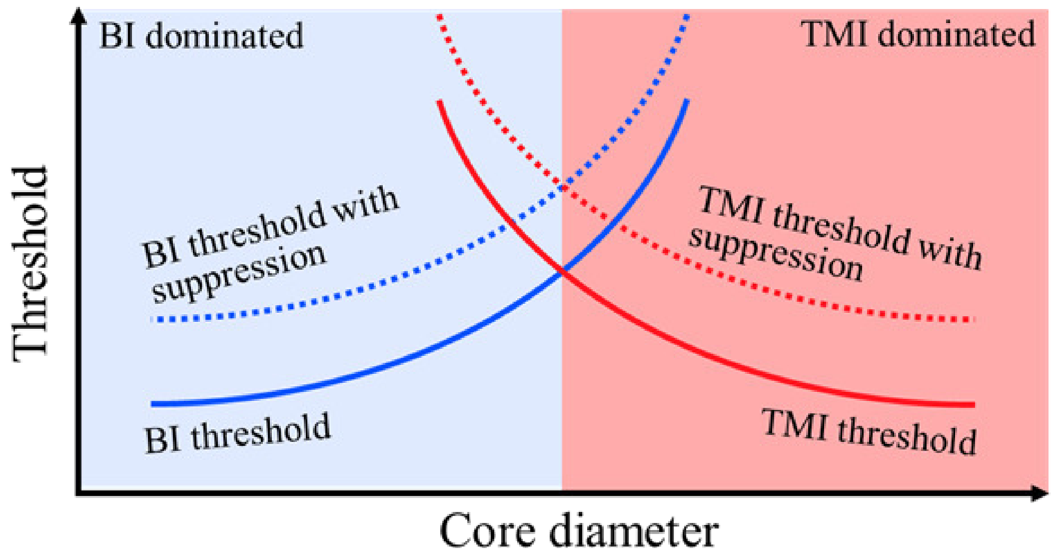

Figure 5.1: Illustration of the tradeoff between the Brillouin instability and the transverse mode instability. [Reprinted/Adapted] with permission from [133] © Optica Publishing Group.

detuning of the pump and signal wavelengths [30, 31] will increase the core diameter at which both BI and TMI play an equal role in limiting the pump power threshold. Thus, it is typically the case that the maximum power threshold is obtained for designs in which BI and TMI play a roughly equal role in limiting the power. Hence, it is critical to develop a model that can study the interaction between BI and TMI.

In this chapter, we determine the optimal fiber core diameter for an Yb^{3+}-doped fiber amplifier with a simple double-clad geometry. Previous research has examined the tradeoff among BI and TMI [86, 106, 141]. Here, we formulate the full BI and TMI model and compare this full model to their respective individual models at different pump powers in order to highlight the differences between them. Simultaneously modeling BI and TMI is challenging because the time scales on which they develop are different. BI, which is associated with acoustic phonons, has a characteristic time scale on the order of nanoseconds, while TMI, which is associated with thermal diffusion, has a time scale on the order of milliseconds. This large difference in time scales implies that a multi-time-scale approach must be used. For that reason, almost

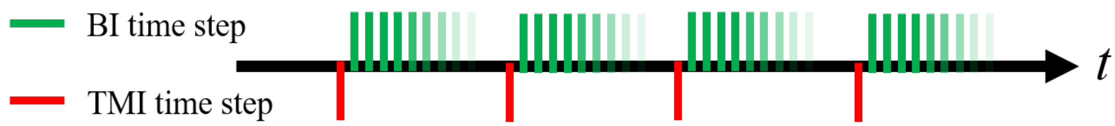

Figure 5.2: Time step scheme. After each TMI time step, a series of BI steps are taken until the fundamental mode and Stokes mode reach steady state. [Reprinted/Adapted] with permission from [133] © Optica Publishing Group.

all work to date has considered these two instabilities separately. In this chapter, we describe a multi-time-scale approach that allows us to simultaneously model BI and TMI. This approach can be extended to more complex geometries in which the overlap of the fundamental mode with the acoustic mode, the thermal mode, and HOMs is minimized. That in turn will make it possible to optimize the optical fiber designs to increase the threshold powers.

5.2 Modeling scheme

Figure 5.2 shows the time discretization scheme for the simulation. Between two TMI iteration steps, which are separated by a time on the order of 1 ms, we take many small time steps, which are separated by a time on the order of 1 ns in order to take BI into consideration. Once the modes have reached steady state on the BI time scale, we jump to the next TMI step. For simplicity, we keep the z-step the same when modeling both BI and TMI. At a minimum, three optical modes representing the forward fundamental mode, forward HOM, and backward fundamental Stokes mode, one thermal mode, and one acoustic mode must be considered for the full BI and TMI simulation.

Figure 5.3 shows an illustration of all the modes that we keep in our model. To model TMI, we include the fundamental mode and one HOM. Most theoretical studies of TMI to date focus on evolution after the onset of TMI when the fundamental mode is significantly depleted. These studies are of little interest for most applications, including applications to high-energy laser beam production, because once forward propagating HOMs have a total power that exceeds about 1% of the output power, the beam quality is unacceptably degraded [88]. Hence, only one HOM is needed to determine the onset of TMI. In BI modeling, we only account for the backward-propagating Stokes mode that is generated by the fundamental mode since we only consider cases where the HOM does not make up the majority of the output power at or below the threshold.

We must also clarify the nomenclature that we use for the different modes. In the TMI literature, it is usual to refer to the optical modes as the pump mode, fundamental mode, and HOM. However, in the BI literature, it is usual to refer to the optical modes as the pump mode and Stokes mode. Although, there is no ambiguity for the Stokes mode, the pump mode in the BI literature corresponds to the fundamental mode in the TMI literature. In this chapter, we will refer to the mode that pumps the laser amplifier as the pump mode, the mode that is amplified as the fundamental mode, the optical mode generated by TMI as the HOM, and the optical mode generated by BI as the Stokes mode.

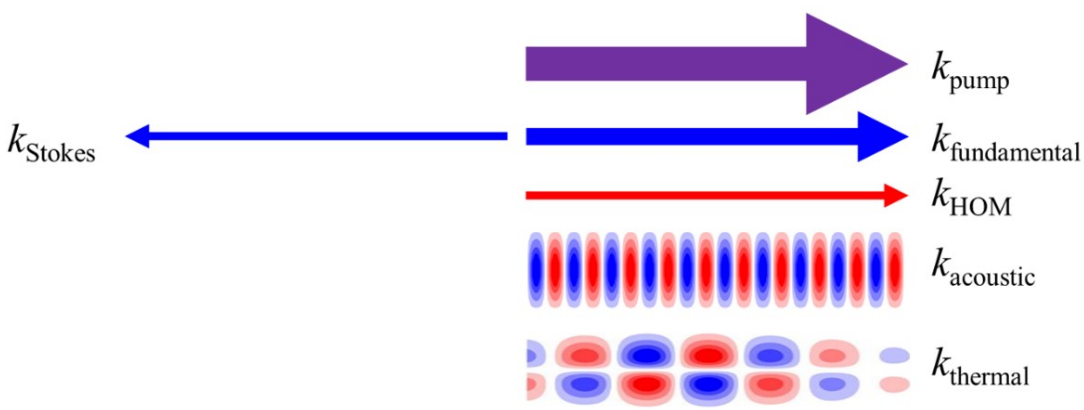

Figure 5.3: Illustration of the modes for the BI and TMI simulations. The pump (k_{pump}), fundamental mode ($k_{\text{fundamental}}$), and HOM (k_{HOM}) propagate in the positive z-direction and have positive wavenumbers. The Stokes mode (k_{Stokes}) propagates backwards and has a negative wavenumber. We represent the density oscillation for k_{acoustic}, and the oscillation in the transverse temperature flow for k_{thermal}. [Reprinted/Adapted] with permission from [133] © Optica Publishing Group.

5.3 *Model for BI and TMI*

In much of the current literature, the equations that describe BI use an electric field amplitude for each mode that has been normalized so that the power for mode l, P_l, is given by $P_l = (1/2)nc\epsilon_0 A_{\mathrm{eff}}|E_l|^2$, where A_{eff} is the effective area [142]. This choice of normalization is possible since both the forward-propagating fundamental mode and the backward-propagating Stokes mode have the same transverse mode profile. In the case of TMI, this normalization is no longer possible since the fundamental mode and the HOM have different mode profiles. Moreover, as Kobyakov et al. [143] have pointed out, this choice is of limited utility since the definition of A_{eff} becomes ambiguous, and it is important to correctly account for the overlap between the optical and acoustic modes when computing gain coefficients. For that reason, we will consistently use field amplitudes A_l that are normalized so that $P_l = (1/2)cn\epsilon_0|A_l|^2$ where $A_l = E_l(A_{\mathrm{eff},l})^{1/2}$. The amplitudes of the fundamental mode, HOM, and Stokes mode will be denoted as A_{F}, A_{H}, and A_{S}, respectively.

In this chapter, we will focus on fibers with a simple geometry in which the interacting modes are all LP modes in a single polarization so that we may write the electric field for mode l as [97]

$$\mathbf{E}_l(\mathbf{r}_\perp, z, t) = \hat{\mathbf{x}}\frac{1}{2}[A_l(z,t)\mathcal{E}_l(\mathbf{r}_\perp)\exp(i\beta z - i\omega t) + \text{c.c.}], \tag{5.1}$$

where $\hat{\mathbf{x}}$ denotes the mode polarization direction, A_l (l=F, H, or S) denotes the mode amplitude, and $\mathcal{E}_l(\mathbf{r}_\perp)$ is the transverse mode profile, normalized so that $\int d^2\mathbf{r}_\perp|\mathcal{E}_l(\mathbf{r}_\perp)|^2 = 1$. We note that $\mathcal{E}_{\mathrm{S}}(\mathbf{r}_\perp) = \mathcal{E}_{\mathrm{F}}(\mathbf{r}_\perp)$. We then find that the equations describing TMI may be written as [80]

$$\begin{aligned} \frac{dA_{\mathrm{F}}}{dz} &= C_{\mathrm{FF}}A_{\mathrm{F}} + C_{\mathrm{FH}}A_{\mathrm{H}}, \\ \frac{dA_{\mathrm{H}}}{dz} &= C_{\mathrm{HH}}A_{\mathrm{H}} + C_{\mathrm{HF}}A_{\mathrm{F}}, \end{aligned} \tag{5.2}$$

where

$$
\begin{aligned}
C_{\mathrm{FF}} &= \frac{i\omega^2}{\beta c^2} n_0 \int d^2\mathbf{r}_\perp |\mathcal{E}_{\mathrm{F}}|^2 \Delta n_0, \\
C_{\mathrm{FH}} &= \frac{i\omega^2}{\beta c^2} n_0 \int d^2\mathbf{r}_\perp \mathcal{E}_{\mathrm{F}}^* \mathcal{E}_{\mathrm{H}} \Delta n_+, \\
C_{\mathrm{HF}} &= \frac{i\omega^2}{\beta c^2} n_0 \int d^2\mathbf{r}_\perp \mathcal{E}_{\mathrm{F}} \mathcal{E}_{\mathrm{H}}^* \Delta n_-, \\
C_{\mathrm{HH}} &= \frac{i\omega^2}{\beta c^2} n_0 \int d^2\mathbf{r}_\perp |\mathcal{E}_{\mathrm{H}}|^2 \Delta n_0.
\end{aligned} \tag{5.3}
$$

Here, the quantities C_{FF}, C_{FH}, C_{HF}, and C_{HH} are optical gains or losses influenced by TMI. These gains or losses do not vary on the BI's nanosecond time scale since they are only dependent on the change in refractive index and temperature, which vary on the order of milliseconds. In Eq. (5.3), we are using the phase-matched model [80], in which we set

$$
\Delta n(z,t) = \Delta n_0(z,t) + \frac{1}{2}[\Delta n_+(z,t)\exp(i\Delta\beta z) + \Delta n_-(z,t)\exp(-i\Delta\beta z)], \tag{5.4}
$$

where $\Delta n(z,t)$ is the total change in the refractive index due to TMI and $\Delta\beta = \beta_{\mathrm{H}} - \beta_{\mathrm{F}}$ represents the difference in propagation constants of the fundamental mode and HOM. The basic assumption of the phase-matched model is that all quantities have a component that varies slowly along the fiber compared to the beat length $2\pi/\Delta\beta$ and a component that oscillates at the beat length period, whose complex amplitude varies slowly compared to the beat length. In the phase-matched model, we ignore contributions to $\Delta n(z,t)$ from higher harmonics of $\Delta\beta$. It was previously shown that this approximation greatly speeds the computational calculations with no loss in accuracy [80] since the contributions of higher harmonics that are proportional to $\exp(im\Delta\beta z)$ with $m > 1$ are negligible. Conversely, we have $|\Delta\beta| \ll \beta_{\mathrm{H}},\ \beta_{\mathrm{F}} \approx \beta$.

We model BI [16, 17] including the contributions from TMI using the equations

$$
\begin{aligned}
\frac{\partial A_{\mathrm{F}}}{\partial z}+\frac{1}{\nu_g}\frac{\partial A_{\mathrm{F}}}{\partial t} &= C_{\mathrm{FF}}A_{\mathrm{F}}+C_{\mathrm{FH}}A_{\mathrm{H}}+i\kappa A_{\mathrm{S}}\rho,\\
\frac{\partial A_{\mathrm{H}}}{\partial z}+\frac{1}{\nu_g}\frac{\partial A_{\mathrm{H}}}{\partial t} &= C_{\mathrm{HH}}A_{\mathrm{H}}+C_{\mathrm{HF}}A_{\mathrm{F}},\\
-\frac{\partial A_{\mathrm{S}}}{\partial z}+\frac{1}{\nu_g}\frac{\partial A_{\mathrm{S}}}{\partial t} &= C_{\mathrm{FF}}A_{\mathrm{S}}+i\kappa A_{\mathrm{F}}\rho^{*},\\
\frac{\partial \rho}{\partial t}+\pi\Delta\nu_B\rho &= i\frac{\Lambda}{A_{\mathrm{eff,F}}}A_{\mathrm{F}}A_{\mathrm{S}}^{*}+f,
\end{aligned}
\tag{5.5}
$$

where $\rho(z,t)$ is the acoustic wave density, κ and Λ are the optical and acoustic coupling parameters [16], $\Delta\nu_B$ is the Brillouin linewidth, and $A_{\mathrm{eff,F}}$ is the effective area for the fundamental mode and Stokes mode. The parameters C_{FF}, C_{FH}, C_{HF}, and C_{HH} are the TMI contributions to the evolution of different fields according to Eq. (5.3). The quantity ν_g represents the group velocity of the fundamental mode. Since the frequency difference between the fundamental mode and HOM is on the order of kHz, we assume that the difference in group velocities between the two modes is negligible. Since the Stokes mode and fundamental mode share nearly the same transverse mode profile, and the frequency shift between them is only on the order of tens of GHz [21, 22], we assume that gain and group velocity for the Stokes mode is the same as for the fundamental mode. We assume that the acoustic noise source $f(z,t)$ is white thermal noise [16, 131], which is delta-correlated such that

$$
\langle f(z,t)f^{*}(z',t')\rangle = Q\delta(z-z')\delta(t-t'). \tag{5.6}
$$

Here, the coefficient Q is the phonon strength parameter and is expressed as

$$
Q=\frac{4\pi kT\rho_0\Delta\nu_B}{v^2A_{\mathrm{eff}}}, \tag{5.7}
$$

where k is the Boltzmann constant, T is the temperature along the fiber, and v is the speed of sound through the material.

To model the heat flow in the fiber, we write

$$
\rho_0C\frac{\partial T_0}{\partial t}+\kappa\nabla_{\perp}^2T_0=Q_0, \qquad \rho_0C\frac{\partial T_+}{\partial t}+\kappa\nabla_{\perp}^2T_+=Q_+, \tag{5.8}
$$

where, consistent with the phase-matched model [80], we write the temperature as $T = T_0 + (1/2)[T_+ \exp(i\Delta\beta z) + T_- \exp(-i\Delta\beta z)]$, and we assume that T_0, T_+, and $T_- = T_+^*$ all vary slowly along z compared to the beat length $2\pi/\Delta\beta$. We similarly write $Q = Q_0 + (1/2)[Q_+ \exp(i\Delta\beta z) + Q_- \exp(-i\Delta\beta z)$, where Q_0, Q_+, and $Q_- = Q_+^*$ all vary slowly compared to the beat length. More details on the phase-matched model that we use here can be found in [80].

When including BI in our model, we only consider the Stokes mode generated by the fundamental mode. Since we focus on the power threshold, the power in the HOM is low (1%) compared to the power in the fundamental mode. Any Stokes light generated from the HOM would be orders of magnitude smaller than the Stokes light generated from the fundamental mode and would make a negligible contribution to the reflectivity. Also, we only consider the forward propagating fundamental mode as any backward propagating fundamental modes would be small at or below the threshold.

Since the gain and temperature profiles vary on the scale of milliseconds, they may be treated as time-independent in each BI evolution, which occurs on the scale of nanoseconds. This implies that C_{FF}, C_{FH}, C_{HF}, and C_{HH} are fixed with respect to the BI time step. After each TMI step, we solve the BI equations, taking time steps on the order of picoseconds until a steady state is reached. When modeling the BI portion of the simulation, we set the temporal step size $\Delta t = \Delta z/\nu_g$, where Δz is the step size in the longitudinal direction [16, 17]. In each BI time step, we first propagate the fundamental mode and the HOM in the forward direction. Then, we propagate the Stokes mode in the backward direction. This relaxation algorithm is commonly used for two-point boundary value problems [144], where $A_{\mathrm{F}}(z = 0, t) = [2P_{\mathrm{F}0}/(cn\epsilon_0)]^{1/2}$, $A_{\mathrm{S}}(z = L, t) = 0$, and $P_{\mathrm{F}0}$ is the input optical power of the signal in fundamental mode. At the beginning of the simulation, we assume that $A_{\mathrm{S}}(z, t < 0) = 0$. We propagate the optical fields for 40 fiber transient times to ensure that the power reaches a steady state, and we then take a statistical average of the Stokes mode at the front of the fiber and the power at the fiber output for an additional 40 fiber transient times. The transient time equals L/ν_g, which is 7.7 ns in this case. Because we use a noise source to seed the BI process, we must take a statistical average, which better reflects experimental measurement.

Table 5.1 shows the fiber parameters used for the simulation [16, 95]. The ratio of cladding diameter, d_{clad}, to core diameter, d_{core}, is fixed at 5 to ensure that the total signal gain is the same within 5% for all core sizes when the pump power is below threshold. The overall goal of our simulation is to vary the core diameter to find the highest threshold when both BI and TMI are considered. Consistent with prior work [80, 95], we assume that the frequency difference between the fundamental mode and the HOM is 1 kHz. We consider a numerical aperture of 0.03, which is consistent with the numerical apertures reported in experiments [145–147]. We use a 10^{th}-order super-Gaussian profile for the rare-earth doping concentration in the fiber cross-section [148].

In this chapter, we focus on the contribution to TMI due to the quantum defect heating [89, 94, 95]. It has been shown that photodarkening can also contribute to TMI [30, 100]. Photodarkening contributes to the thermally induced index grating coherently with quantum defect heating [2]. Hence, the heat source term and absorption term from photodarkening [30] could in principle be added to the phase-matched model for TMI [80].

5.4 BI and TMI threshold at core diameters of 30 and 45 μm

When we refer to the threshold, we are always referring to the pump power threshold that is limited by either BI or TMI. We define the threshold for BI, $P_{\text{pump,BI}}$, as the input pump power at which the reflectivity defined as $\rho_{\text{S}} = \overline{P_{\text{S}}}(z=0)/[\overline{P_{\text{F}}}(z=L) + \overline{P_{\text{S}}}(z=0)]$ reaches 1%, where the overline indicates an average over the 40 tran-

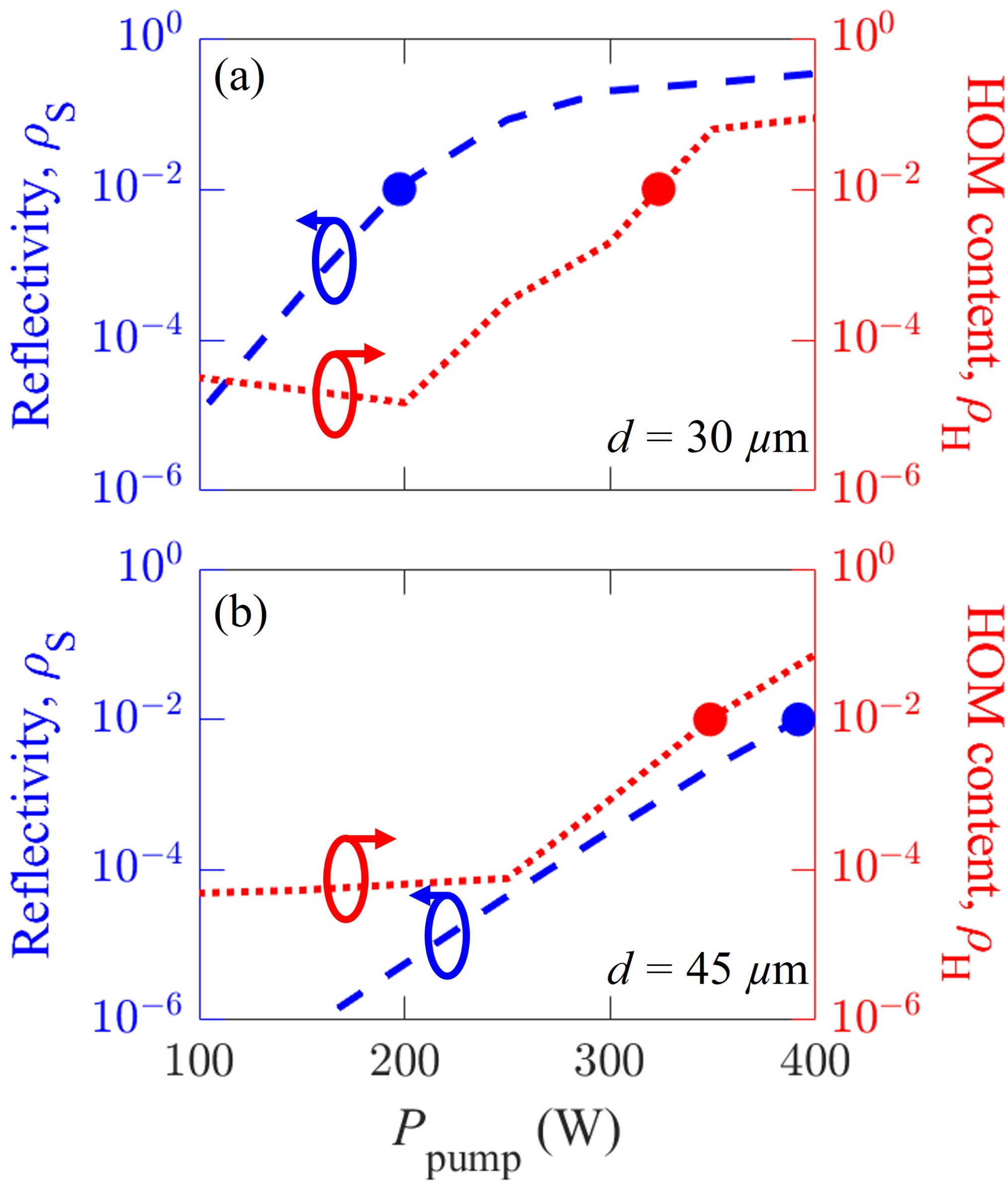

Figure 5.4: Reflectivity ρ_S due to BI and the HOM content ρ_H due to TMI as a function of pump power for a core diameter of (a) $d = 30$ μm and (b) $d = 45$ μm. The results here are obtained using the full model that includes both BI and TMI. [Reprinted/Adapted] with permission from [133] © Optica Publishing Group.

sient fiber times $t_f = Ln/c$, as described in the previous section. This definition of reflectivity is used in the gain fiber so that the reflectivity represents the ratio of the reflected power relative to the amount of total output power that is reflected, and the lower and upper bounds of ρ_{S} in this definition are 0 and 1, which is consistent with the definition of the HOM content. To ensure that the power reaches a steady state due to TMI, we also average the reflectivity in the full model over the last 50 TMI steps. We define the threshold for TMI, $P_{\mathrm{pump,TMI}}$, as the input pump power at

Table 5.1. BI-TMI model simulation parameters

Fiber length	L	1.6 m
Core index	n_{core}	1.45031
Numerical aperture	$N.A.$	0.03
Signal power	P_{sig}	30 W
HOM seed power	P_{HOM}	3 mW
Pump emission	$\sigma_p^{(e)}$	1.87×10^{-27} m^2
Signal emission	$\sigma_s^{(e)}$	6×10^{-27} m^2
z step	Δz	8×10^{-5} m
t step,TMI	Δt_{TMI}	20 μs
t step, BI	Δt_{BI}	0.774 ps
Transverse step	$\Delta x, \Delta y$	2 μm
Doping concentration	N_0	6×10^{25} m^{-3}
Brillouin linewidth	$\Delta\nu_B$	57 MHz
Heat lifetime	τ	0.85 ms
Pump wavelength	λ_{pump}	977 nm
Signal wavelength	$\lambda_{\mathrm{signal}}$	1064 nm
Pump absorption	$\sigma_p^{(a)}$	1.53×10^{-24} m^2
Signal absorption	$\sigma_s^{(a)}$	3.58×10^{-25} m^2
Density	ρ_0	2200 kg/m^3
Heat capacity	C	703 J/(kg − K)
Thermal conductivity	κ	1.38 W/(m − K)
Initial temperature	T	300 K

which the HOM content defined as $\rho_{\mathrm{H}} = \max\{P_{\mathrm{H}}(z=L)/[P_{\mathrm{F}}(z=L) + P_{\mathrm{H}}(z=L)]\}$ reaches 1% [80]. We write the maximum in the definition since the impact of TMI is determined by this maximum value [80,95]. When we consider BI and TMI together, the threshold, $P_{\mathrm{pump,full}}$, is defined as the pump power at which the maximum of the reflectivity ρ_{S} or the HOM content ρ_{H} reaches 1%. We study the thresholds for BI and TMI using the full model described in the previous section for core diameters of 30 and 45 μm. The dashed blue and dotted red curves in Fig. 5.4 show reflectivity, ρ_{S}, and the HOM content, ρ_{H}, respectively, as a function of pump power. For fibers with the smaller core diameter of 30 μm, shown in Fig. 5.4(a), the pump power is 197 W when the reflectivity ρ_{S} reaches 1%, and the pump power is 323 W when the HOM content ρ_{H} reaches 1%. In this case, BI plays a more important role and reaches threshold at a lower pump power since the relatively small core size increases the intensity. By contrast, for fibers with the larger core diameter of 45 μm, the pump power is 391 W when the reflectivity ρ_{S} reaches 1%, and the pump power is 348 W when the HOM content ρ_{H} reaches 1%. In this case, TMI is the dominant effect that limits the pump power threshold due to a stronger coupling between the fundamental mode and the HOM. When TMI is the limiting nonlinear effect, decreasing the core diameter improves the TMI threshold.

5.5 BI and TMI thresholds as a function of core diameter

In Fig. 5.5(a), the solid green curve shows the threshold $P_{\mathrm{pump,full}}$, which is the power, including the effects of both BI and TMI. We also show P_{fund}, which is the output power for the fundamental mode at the pump power threshold $P_{\mathrm{pump,full}}$. As explained in the previous section, increasing the diameter increases the modal area and lowers the intensity, which helps to improve the BI threshold. However, further increasing the diameter eventually increases the impact of the HOM in our study, which lowers the TMI threshold. The cutoff diameter in our study for the HOM

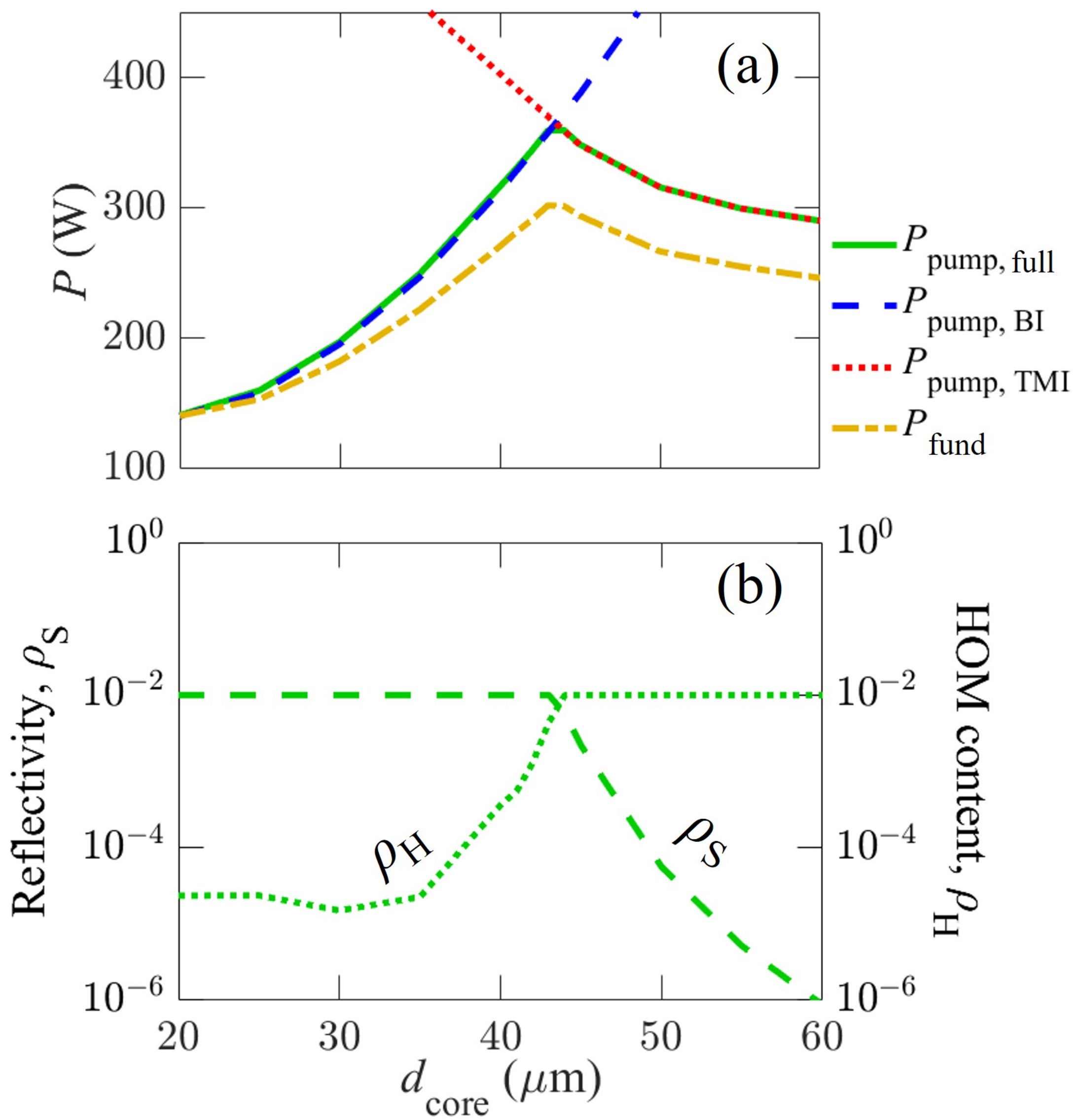

Figure 5.5: (a) Pump power threshold when we consider BI and TMI altogether or BI and TMI separately. The fundamental mode power P_{fund} shows the output power for the fundamental mode at the pump power threshold $P_{\text{pump,full}}$. (b) Reflectivity ρ_{S} and HOM content ρ_{H} for the full model at the corresponding pump power threshold, $P_{\text{pump,full}}$, indicated by the green curve in (a). [Reprinted/Adapted] with permission from [133] © Optica Publishing Group.

is at 27.2 μm. Decreasing the core diameter to values near the cutoff of the HOM will cause the HOM to be less confined and greatly increase the TMI threshold. In Fig. 5.5(b), the dashed and dotted green curves show the reflectivity ρ_{S} and the HOM content ρ_{H}, respectively, for the full model at the corresponding pump power indicated by the green curve in Fig. 5.5(a). Since our definition of threshold is when either the reflectivity or the HOM content reaches 1%, the curves in Fig. 5.5(b) will be capped at 1%. Figure 5.5(b) clearly indicates the limiting effect on the instability corresponding to the pump power threshold curve in Fig. 5.5(a). The core diameter of 43 μm yields the highest threshold; at that diameter the threshold contributions due to BI and TMI are equal. The dash-dotted orange curve in Fig. 5.5(a) shows the output power at the pump power threshold, which indicates the maximum output power at the optimal core diameter of 43 μm.

In Fig. 5.5(a), the dotted red curve shows the threshold power, $P_{\mathrm{pump,TMI}}$, when only TMI is present. The dashed blue curve shows the threshold power, $P_{\mathrm{pump,BI}}$, when only BI is present. At a small diameter of 20 μm, the full model agrees with the BI only model, that only includes BI, as there is a negligible influence on the pump power threshold due to TMI. At a large diameter of 60 μm, the threshold for the full model agrees with the threshold for the TMI only model, the model that only includes TMI, as BI makes a negligible contribution to the pump power threshold.

5.6 Comparison of the individual and full models

Figure 5.4 also shows that when the full BI and TMI model is considered, the TMI threshold for a core diameter of 30 μm is lower than the threshold for a core diameter of 45 μm. This result is contrary to the expectation that decreasing the core diameter should increase the TMI threshold. In Fig. 5.4(a), we see that after the BI threshold is reached at 197 W, there is significant reflection of the output power. We observe that the onset of TMI may occur at a lower-than-normal pump power when the reflectivity due to BI is sufficiently high and the pump power is above the BI threshold so the reflectivity is greater than 1%.

Next, we study when BI will trigger TMI. Figure 5.6 shows the full model reflectivity and HOM content compared to the HOM content from the TMI only model as a function of pump power. The core diameter is 30 μm. The dashed blue and dotted red curves are replotted from Fig. 5.4(a) so that the comparison may be easily made. The solid green curve shows the HOM content from the TMI only model. The dotted black horizontal line in Fig. 5.6 marks the 1% threshold criterion. Figure 5.6 shows that when the pump power is under 200 W, the reflectivity is low, and there is a negligible difference between the HOM content predicted by the TMI only model and the full model. However, further increasing the pump power past 200 W yields an increase in reflectivity that then triggers TMI in the full model. The TMI threshold

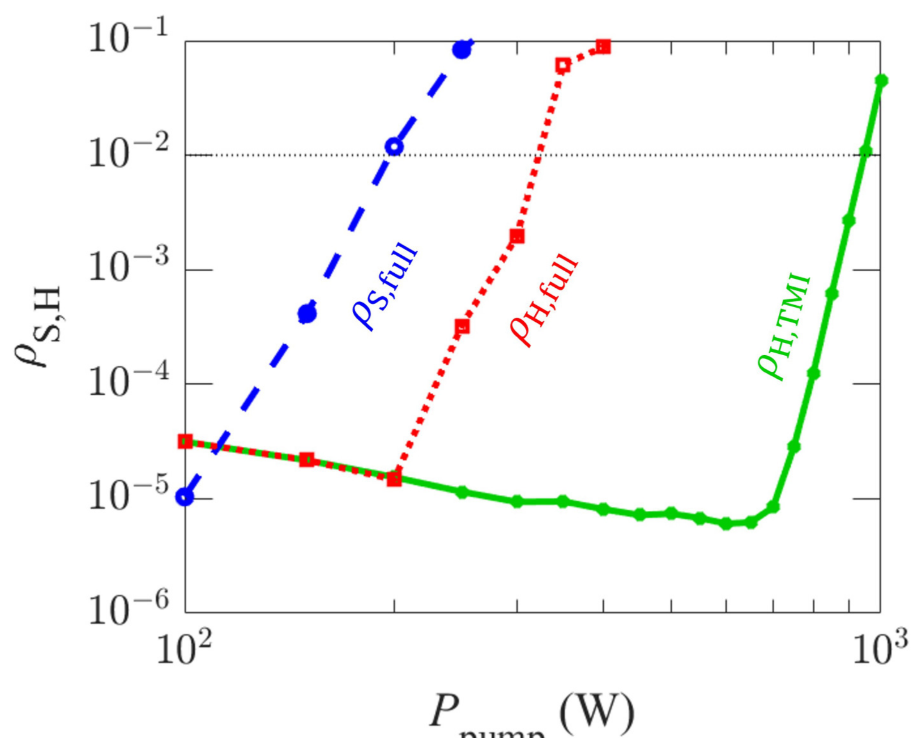

Figure 5.6: Reflectivity and HOM content from the full model and the TMI only model as a function of pump power. The core diameter is 30 μm. [Reprinted/Adapted] with permission from [133] © Optica Publishing Group.

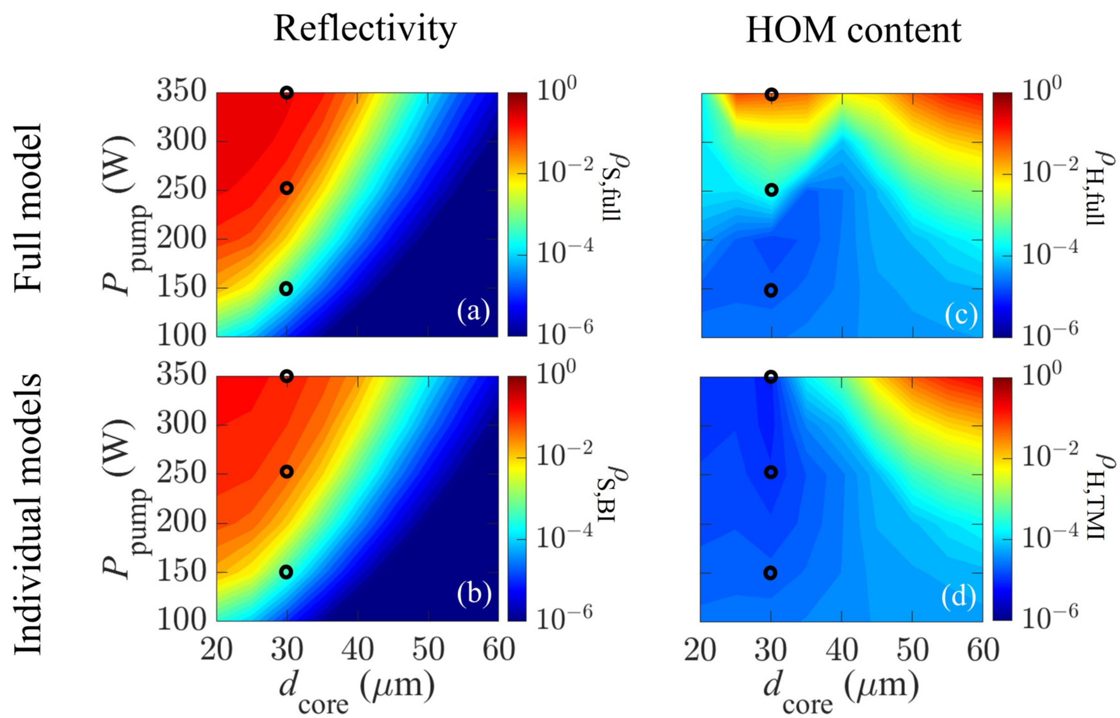

Figure 5.7: (a) Reflectivity from the full model, (b) reflectivity from the BI only model, (c) HOM content from the full model, and (d) HOM content from the TMI only model as a function of pump power and core diameter. Black circles in (a)−(d) show pump powers of 150, 250, and 350 W at a core diameter of 30 μm. [Reprinted/Adapted] with permission from [133] © Optica Publishing Group.

with the full model is at a pump power of 323 W compared to the TMI only threshold of 946 W.

In this example, the onset of BI at 1% does not trigger TMI, but rather TMI is trigged by BI when the reflectivity reaches about 10%. If there is significant reflectivity, much greater than the 1% used to denote the onset of BI, the interaction between the Stokes and fundamental mode causes the fundamental mode to fluctuate stochastically along the fiber. Rather than seeding the HOM directly, these fluctuations may make it possible for the fundamental mode and the HOM to interact. This result is consistent with experiments of Lee et al. [149] who found that stimulated Brillouin scattering may induce TMI and that the TMI threshold closely follows the BI threshold. This behavior is not captured by previous models that consider TMI or BI separately.

To gain a better understanding of the interaction between the TMI and BI, we now compare the full model and individual models at different power levels so that any differences between them may be distinguished. Figures 5.7(a)−(d) show the full model reflectivity $\rho_{\mathrm{S,full}}$, BI only reflectivity $\rho_{\mathrm{S,BI}}$, full model HOM content $\rho_{\mathrm{H,full}}$, and TMI only HOM content, $\rho_{\mathrm{H,TMI}}$ as a function of pump power and core diameter. In Fig. 5.7(a), the reflectivity increases as the power increases or the core diameter decreases.

To further understand the difference in predicted reflectivity and HOM content between the individual BI and TMI models to the full model, we show the difference in predicted reflectivity $\Delta\rho_{\mathrm{S}} = |\rho_{\mathrm{S,BI}} - \rho_{\mathrm{S,full}}|$ and HOM content $\Delta\rho_{\mathrm{H}} = |\rho_{\mathrm{H,TMI}} - \rho_{\mathrm{S,full}}|$, between the full model and individual models in Fig. 5.8. The temperature in the full model increases due to the quantum defect, which can lead to a difference in the predicted reflectivity values between the full model and the BI only model, as shown in Fig. 5.8(a). Figure 5.8(b) shows that when the full model is under the BI threshold, there is a negligible difference in the predicted HOM content between the full model and the TMI only model. However, once there is significant reflectivity at $d_{\text{core}} = 30\ \mu$m and $P_{\text{pump}} = 350$ W, the HOM content predicted by the full model differs from the HOM content predicted by the TMI only model.

To compare the HOM content that is predicted by the different models, we study the evolution of the reflectivity and the HOM content as a function of time for the three regions marked with circles in Fig. 5.7. Figures 5.9(a)−(c) show the reflectivity

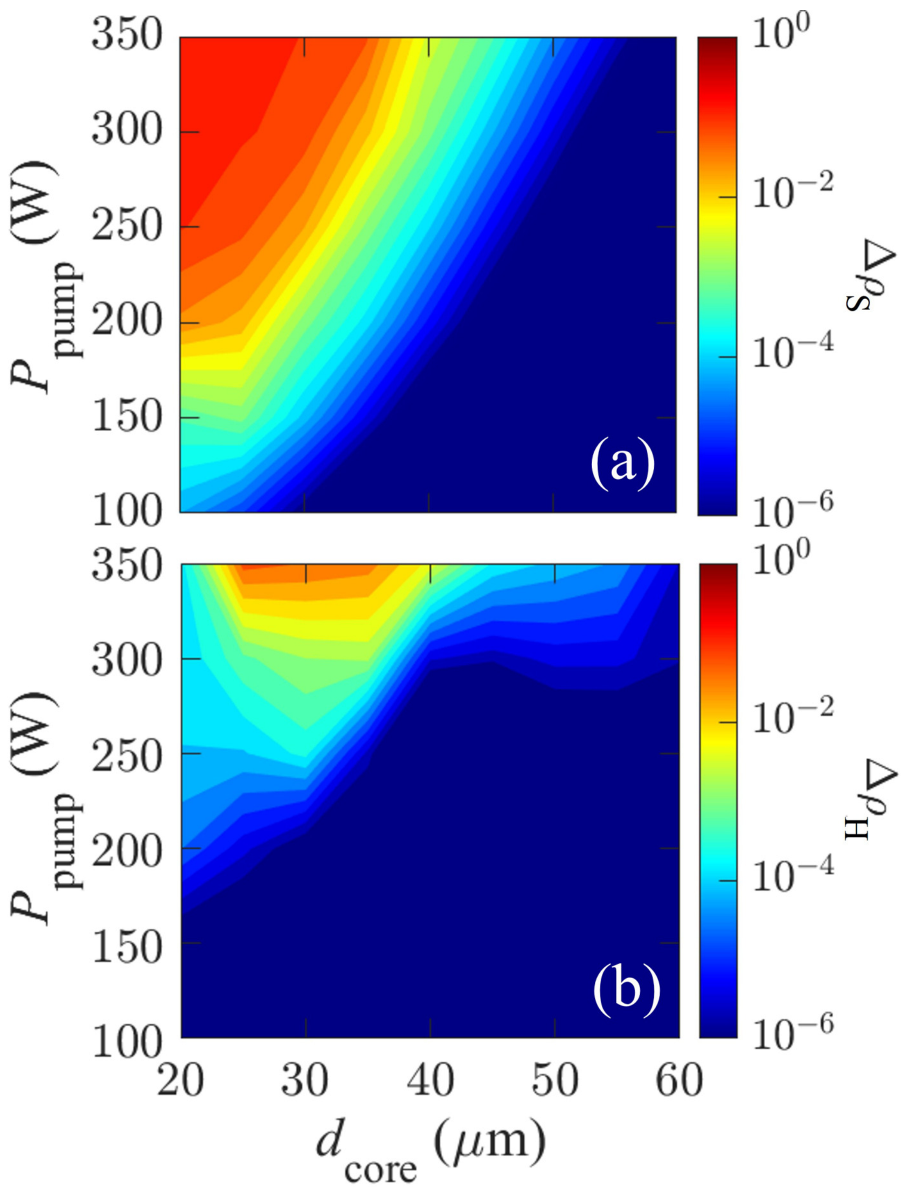

Figure 5.8: Absolute value of the difference in the predicted (a) reflectivity and (b) HOM content between the full and individual models. [Reprinted/Adapted] with permission from [133] © Optica Publishing Group.

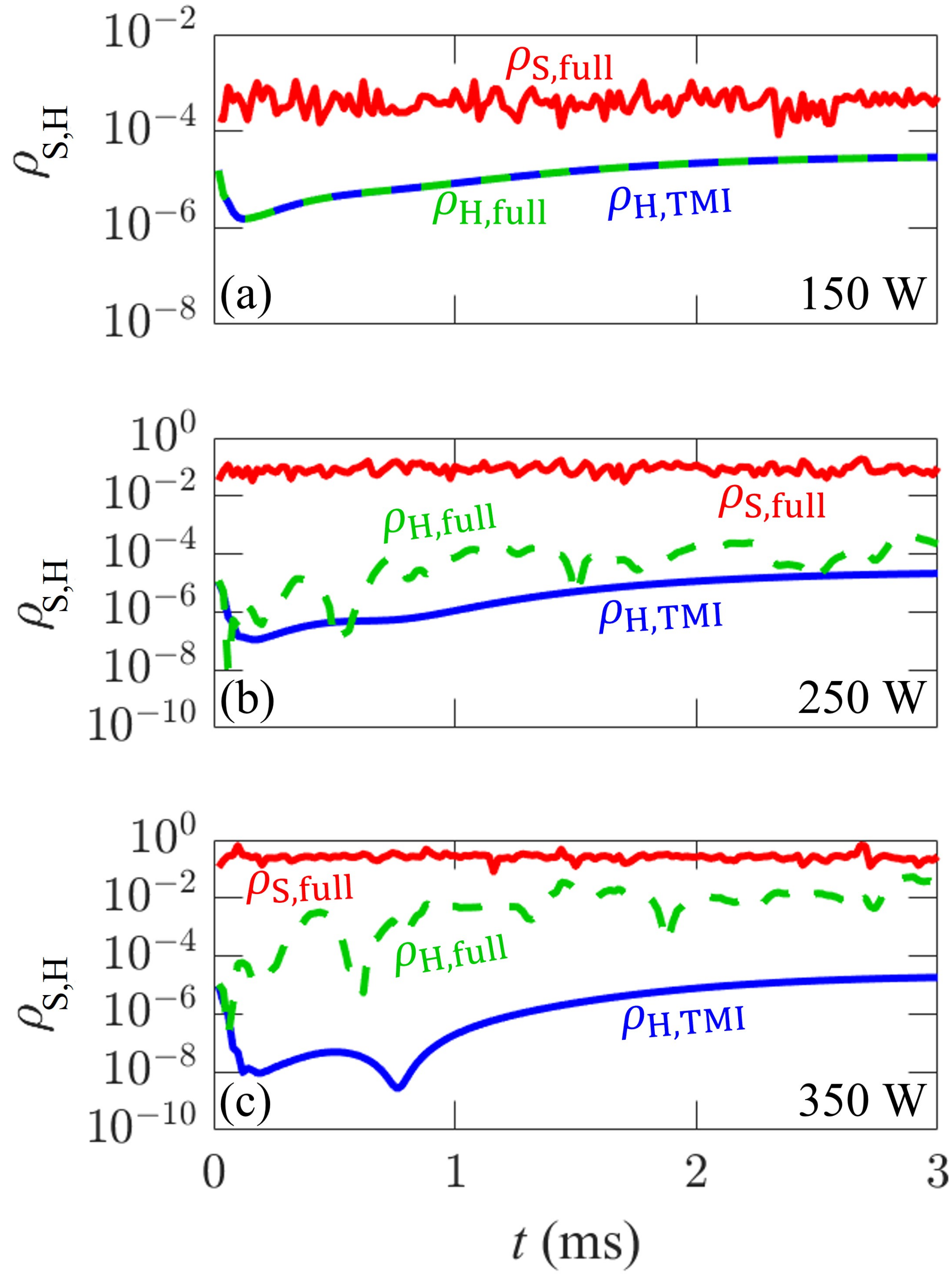

Figure 5.9: Reflectivity and HOM content as a function of time for pump powers of (a) 150 W, (b) 250 W, and (c) 350 W with a core diameter of 30 μm. [Reprinted/Adapted] with permission from [133] © Optica Publishing Group.

and the HOM content for pump powers of 150, 250, and 350 W, respectively, as a function of time. The core diameter is 30 μm. The solid blue, dashed green, and solid red curves represent the HOM content from a TMI only simulation $\rho_{\mathrm{H,TMI}}$, HOM content for the full model $\rho_{\mathrm{H,full}}$, and reflectivity from the full model $\rho_{\mathrm{S,full}}$, respectively. When the pump power is 150 W, the averaged reflectivity is 0.043% which is under the BI threshold. The HOM content predicted by the full model and by the TMI only model are nearly identical. In this case, adding BI in the model does not have any impact on TMI. At a pump power of 250 W, the averaged reflectivity is near 8.9%. Both the TMI only model and full model lead to a small HOM content below 1%. The difference in the peak HOM content is also small. Hence, around the BI threshold, the interaction between BI and TMI is not significant, as shown in Fig. 5.9(b). However, when the pump power increases to 350 W, the averaged reflectivity reaches 27%. The higher reflectivity leads to amplitude modulation of the signal and triggers TMI, as shown in Fig. 5.9(c). In this case, the large BI leads to significant power transfer between the fundamental mode and the Stokes mode. Hence, there is a substantial difference in the time evolution of the HOM contents between the full model and the TMI only model, which leads to different contours in Figs. 5.7(c) and (d).

5.7 Conclusions

BI and TMI have been modeled separately in the past, but including both effects in one simulation is necessary to determine when and how they interact particularly since both effects have roughly equal magnitudes at the optimal operating points in the parameter space. We formulate the equations to model both BI and TMI in a single simulation. For the system model and parameters that we considered, the optimal core diameter with a maximum power threshold is around 43 μm. For small core sizes less than the optimal core diameter of 43 μm, BI dominates and TMI plays little role in limiting the pump power threshold. For core sizes that are greater than 43 μm, the BI effect is negligible, and the full model with both BI and TMI yields a similar threshold as the threshold for TMI alone. The difference between the full model and individual model pump power thresholds is negligible in this case, as BI and TMI are not strong enough to interact with each other. At large pump powers and small core diameters, where the reflectivity is large, BI may trigger TMI due to modulation of the power in the fundamental mode, so that the TMI threshold is significantly lower than is the case when modeling TMI alone.

Combining both BI and TMI in a single simulation makes it possible to simultaneously optimize the fiber design to minimize both effects and yield the highest power thresholds.

CHAPTER SIX

Summary and Future Prospects

6.1 Summary

In this dissertation, first we studied avoided crossings due to mode coupling in adjacent slab waveguides. The principal features of avoided crossings in index-guided and antiresonant waveguides may be explained by using a simple one-dimensional slab waveguide model. We also showed that the coupled mode theory that predicts the behavior of avoided crossings in guided modes may be modified to predict the avoided-crossing behavior for leaky modes. We described the similarities and differences between the specialty optical fibers and the simpler slab waveguides and found that this model is a useful basis for understanding avoided crossings in the more complex geometries that are typically found in photonic crystal fibers. The motivation to study avoided crossings in antiresonant slab waveguides comes from the idea of using gas-filled negative curvature fibers which may be used for high-energy laser beam production and may lead to the suppression of nonlinear effects like BI and TMI. Fiber designs such as negative curvature fiber may support multiple transverse modes that all have low loss since the optical mode is confined in a low index gas core. This may enable certain conditions where transverse modes interact and couple leading to avoided crossings which is not ideal for high-energy laser systems.

Second, we formulated the phase-matched model for TMI which is described as three-wave mixing equations with a single HOM. TMI is induced by a thermally seeded refractive index grating that couples power from usually a near Gaussian fundamental mode to other HOMs. In extreme cases TMI is characterized by a temporally changing unstable output mode profile which may severely affect power scalability in high-energy laser systems and unpredictable behavior when propagating through the atmosphere. In the phase-matched model, only the first harmonic frequency tone that describes the refractive index and temperature grating which causes TMI is considered and was found that higher harmonic tones do not significantly contribute to the evolution of TMI. With the fiber parameters considered, the phase-matched model showed a large computational speedup with no loss of accuracy compared to the full model, which includes all high frequency components that make up the refractive index and temperature gratings.

Third, we studied how the BI may be suppressed using piecewise parabolic phase modulation. BI is caused by the interaction of acoustic phonons and forward propagating light, where at sufficient powers causes large pulses to be reflected toward the laser source. Phase modulation works by broadening the laser linewidth which spreads the gain among many frequency tones which lowers the overall Brillouin gain. Piecewise parabolic phase modulation has a particular advantage over other popular phase modulation techniques such as PRBS, in that the associated spectrum for piecewise parabolic phase modulation is nearly rectangular. This is desirable in power scaling applications that rely on spectral beam combining compared to PRBS, which has a sinc^2 envelope in its spectrum. We compared the performance of piecewise parabolic phase modulation such as triangle and sawtooth modulation to PRBS phase modulation. The triangle and sawtooth frequency modulation with a period of 23 ns yielded a higher BI threshold compared to PRBS 5 and PRBS 7 with a modulation frequency of 1.5 GHz. However, the drawback to piecewise parabolic phase modulation is the large phase shifts required but may be possible with Lithium niobate electro-optic modulators [132].

Lastly, we formulated equations to model BI and TMI in a single simulation. A multi-time-scale approach must be used since each of the nonlinear effects evolve at drastically different rates. Combining both nonlinear effects into a single simulation is only possible due to the use of the phase-matched model for TMI. The full model for TMI requires that the longitudinal discretization be much smaller than the beat length $L_B/\Delta z$ and was shown in [80] that this requirement led to over a 100-fold increase in wall time. Adding the BI model with gain terms influenced by TMI as previously mentioned would quickly lead to unreasonably large wall times. BI which is due to the interaction of optical and acoustic modes, occurs on the nanosecond time scale; whereas TMI which is attributed to thermal diffusion, occurs on a scale of milliseconds. Only a single backward Stokes mode and forward HOM are needed for the study since the interest is to find the pump power threshold under both effects. At and under the pump power threshold, there is negligible interaction between the two nonlinear effects, and the total pump power threshold may be described as the intersection of the individual threshold curves for BI and TMI. However, at sufficiently high pump power and small core diameter, there is some region where BI may stimulate TMI due to large stochastic amplitude modulation of the fundamental mode. This result cannot be predicted by either the BI or TMI only model alone.

6.2 Future Prospects

Because of their excellent beam quality, fiber amplifier-based high-energy lasers have grown in popularity. We expect extensive work to continue regarding the development of higher output powers for high-energy lasers, especially with the current political atmosphere in the world. With the addition of computationally efficient simulation modeling tools previously described, it will be feasible to optimize fiber geometries and achieve larger operating powers. Further improvements in the power thresholds for fiber amplifiers may be done with either intrinsic methods such as optimizing the fiber design by employing photonic crystal fibers and fiber tapering, or extrinsic methods like fiber coiling optimization and tuning of the laser parameters.

Most of the research related to simulation and theory regarding TMI have treated the thermal seed source as quantum defect heating. While defect heating may contribute to the heat load in a fiber amplifier, it has recently been shown that another heat source may also contribute to the TMI threshold, which is photodarkening [2]. Photodarkening leads to the development of color centers in the fiber. The fiber develops a non transparent center that absorbs signal and pump light. The absorption spectra is centered in the visible region of light, hence "color center", however, the tail of the absorption spectra creeps into the 1 μm region [2, 150]. Thus photodarkening may affect typical signal and pump wavelengths used in fiber amplifiers. It has been shown though that thermally annealing the fiber may temporarily increase the TMI power threshold [2]. Accurate modeling of photodarkening may lead to additional suppression of the TMI effect.

Nonlinear effects like BI and TMI may be suppressed using photonic crystal fiber designs. One avenue of pursuit is to employ gas filled negative curvature fibers. Negative curvature fibers with a broad bandwidth and low loss have drawn attention because it is possible to fill the fibers with fluids [151–154]. Filling negative curvature fibers with gases such as H_2 or N_2O gases [155–157] and using a pump at 1.5 μm, emission near 4.5 μm has been observed. Being able to host gases allows negative curvature fibers to serve as mid-infrared lasers, which are currently being used in sensing, medical, and defense applications [158]. Designing hollow-core negative curvature fibers to find the optimum structure that can simultaneously provide low transmission loss at both the pump and signal wavelength for different gases. Hollow-core fibers usually have a large core with higher order modes, even with some higher order mode suppression scheme. This will enable the study of nonlinear effects like BI and TMI in fiber lasers that employ negative curvature fibers.

Along with PCFs, tapering of the core diameter may also mitigate nonlinear effects. The number of transverse modes that may be supported is directed tied to the diameter of the fiber. Increasing the fiber diameter also increases the number of transverse optical modes that may be supported. Tapering of the core diameter may be used to effectively make a portion of the fiber single mode thereby suppressing TMI by yielding high loss for HOMs, and by tapering to a large diameter the intensity may be kept low to suppress BI. Preliminary study of fiber tapering has been successfully demonstrated using a saddle shaped fiber to suppress TMI [139]. Optimizing the taper design will lead to larger output powers. Another avenue to pursue is efficient fiber coiling methods. Coiling the fiber results in an exponential increase in loss for HOMs while the fundamental mode sees relatively low loss; however, at sufficiently small bend radii, the fundamental mode can also see large loss, which is followed by a decrease in output power. Coiling techniques usually rely on monotonical increase in bend radius where the fiber is coiled in a flat spiral, which is usually implemented so that cold plates can thermally regulate the fiber temperature. Coiling techniques with the intention of providing the maximum possible loss for the HOM while keeping power in the fundamental mode may prove beneficial in increasing threshold powers for nonlinear effects. We believe that further research in this field will lead to more developments for high energy laser applications in the medical, industrial, manufacturing, and defense industries.

[1] M. N. Zervas and C. A. Codemard, "High power fiber lasers: a review," IEEE J. Sel. Top. Quantum Electron. **20**5, 219–241 (2014).

[2] C. Jauregui, C. Stihler, and J. Limpert, "Transverse mode instability," Adv. Opt. Photon. **12**2, 429–484 (2020).

[3] C. Jauregui, J. Limpert, and A. Tünnermann, "High-power fibre lasers," Nat. Photonics **7**(11), 861—867 (2013).

[4] D. J. Richardson, J. Nilsson, and W. A. Clarkson, "High power fiber lasers: current status and future perspectives [Invited]," J. Opt. Soc. Am. B **27**(11), B63–B92 (2010).

[5] D. Gloge, "Optical fibres for communication." Appl. Opt. **13**(2), 249–254 (1974).

[6] K. C. Kao, and T. W. Davies, "Spectroscopic studies of ultra-low loss optical glasses I: single beam method" J. Sci. Instrum. **1**(11), 1063–1068 (1968).

[7] F. P. Kapron and D. B. Keck, "Pulse transmission through a dielectric optical waveguide" Appl. Opt. **10**(7), 1519–1523 (1971).

[8] W. Shi, Q. Fang, X. Zhu, R. A. Norwood, and N. Peyghambarian, "Fiber lasers and their applications [Invited]," Appl. Opt. **53**28, 6554–6568 (2014).

[9] H. Injeyan and G. D. Goodno, *High Power Laser Handbook*, 1st edition (McGraw-Hill, 2011), Chap. 18.

[10] T. H. Maiman, "Stimulated optical radiation in ruby," Nature **187**, 493–494 (1960).

[11] E. Snitzer, H. Po, F. Hakimi, R. Tumminelli, and B. C. McCollum, "Double clad, offset core Nd fibre laser," in Proc. Opt. Fib. Sensors 2, PD5 (1988).

[12] R. Maurer, "Optical waveguide light source," US patent 3,808,549 (1974).

[13] M. O'Connor, V. Gapontsev, V. Fomin, M. Abramov, and A. Ferin, "Power scaling of SM fiber lasers toward 10 kW," in Proc. Conf. Lasers Electro-Optics/Int. Quantum Electron., CThA3 (2009).

[14] G. P. Agrawal, *Nonlinear Fiber Optics: Fundamentals and Applications* (Academic Press, 2006).

[15] T. Eidam, S. Hanf, E. Seise, T. V. Andersen, T. Gabler, C. Wirth, T. Schreiber, J. Limpert, and A. Tünnermann, "Femtosecond fiber CPA system emitting 830 W average output power," Opt. Lett. **35**(2), 94–96 (2010).

[16] C. E. Mungan, S. D. Rogers, N. Satyan, and J. O. White , "Time-dependent modeling of Brillouin scattering in optical fibers excited by a chirped diode laser," IEEE Journal of Quantum Electronics **48**(12), 1542–1546 (2012).

[17] C. Zeringue, I. Dajani, S. Naderi, G. T. Moore, and C. Robin, "A theoretical study of transient stimulated Brillouin scattering in optical fibers seeded with phase-modulated light," Opt. Express **20**(19), 21196–21213 (2012).

[18] A. Flores, C. Robin, A. Lanari, and I. Dajani, "Pseudo-random binary sequence phase modulation for narrow linewidth, kilowatt, monolithic fiber amplifiers," Opt. Express **22**(15) 17735–17744, (2014).

[19] J. White, J. T. Young, C. Wei, J. Hu, and C. R. Menyuk, "Seeding fiber amplifiers with piecewise parabolic phase modulation for high SBS thresholds and compact spectra," Opt. Express **27**(3), 2962–2974 (2019).

[20] L.-G. Hwa, J. Schroeder, and X.-S. Zhao, "Intrinsic Brillouin linewidths and stimulated Brillouin gain coefficients in glasses studied by inelastic light scattering," J. Opt. Soc. Am. B **6**(4), 833–839 (1989).

[21] G. W. Faris, L. E. Jusinski, and A. P. Hickman, "High-resolution stimulated Brillouin gain spectroscopy in glasses and crystals," J. Opt. Soc. Am. B **10**(4), 587–599 (1993).

[22] E. P. Ippen, and R. H. Stolen, "Stimulated Brillouin scattering in optical fibers," Appl. Phys. Lett. **21**(11), 539–541 (1972).

[23] J. B. Coles, B. P.-P. Kuo, N. Alic, S. Moro, C.-S. Bres, J. M. Chavez Boggio, P.A. Andrekson, M. Karlsson, and S. Radic, "Bandwidth-efficient phase modulation techniques for stimulated Brillouin scattering suppression in fiber optic parametric amplifiers," Opt. Express 18(17), 18138–18150 (2010).

[24] J. O. White, A. Vasilyev, J. P. Cahill, N. Satyan, O. Okusaga, G. Rakuljic, C. E. Mungan, and A. Yariv, "Suppression of stimulated Brillouin scattering in optical fibers using a linearly chirped diode laser," Opt. Express 20(14), 15872–15881 (2012).

[25] B. Anderson, A. Flores, R. Holten, and I. Dajani, "Comparison of phase modulation schemes for coherently combined fiber amplifiers," Opt. Express 23(21), 27046–27060, (2015).

[26] N. A. Naderi, A. Flores, B. M. Anderson, and I. Dajani, "Beam combinable, kilowatt, all-fiber amplifier based on phase-modulated laser gain competition," Opt. Lett. 41(17), 3964–3967 (2016).

[27] J. P. Leidner and J. R. Marciante, "Three fiber designs for mitigating thermal mode instability in high-power fiber amplifiers," Opt. Express **28**(19), 28502–28517 (2020).

[28] F. Beier, C. Hupel, J. Nold, S. Kuhn, S. Hein, J. Ihring, B. Sattler, N. Haarlammert, T. Schreiber, R. Eberhardt, and A. Tünnermann, "Narrow linewidth, single mode 3 kW average power from a directly diode pumped ytterbium-doped low NA fiber amplifier," Opt. Express 24(6), 6011–6020 (2016).

[29] R. Tao, R. Su, P. Ma, X. Wang, and P. Zhou, "Suppressing mode instabilities by optimizing the fiber coiling methods," Laser Phys. Lett. **14**, 025101 (2017).

[30] C. Jauregui, H.-J. Otto, F. Stutzki, J. Limpert, and A. Tünnermann, "Simplified modelling the mode instability threshold of high power fiber amplifiers in the presence of photodarkening," Opt. Express 23(16), 20203–20218 (2015).

[31] R. Tao, P. Ma, X. Wang, P. Zhou, and Z. Liu, "Mitigating of modal instabilities in linearly-polarized fiber amplifiers by shifting pump wavelength," J. Opt. **17**(4), 045504 (2015).

[32] R. L. Farrow, G. R. Hadley, A. V. Smith and D. A. V. Kliner, "Numerical modeling of self-focusing beams in fiber amplifiers," Proc. SPIE, **6453**, 645309, (2007).

[33] : J. T. Young, C. Wei, J. Hu, and C. R. Menyuk, "Mode coupling at the avoided crossings in slab waveguides with comparison to optical fibers: tutorial" J. Opt. Soc. Am. B **38**(12), F104–F114 (2021).

[34] J. Hu and C. R. Menyuk, "Understanding leaky modes: slab waveguide revisited," Adv. Opt. Photon. **1**, 58–106 (2009).

[35] A. Yariv, *Quantum Electronics* (Wiley, 1989).

[36] L. A. Coldren, S. W. Corzine, and M. L. Mašanović, *Diode Lasers and Photonic Integrated Circuits, Second Edition*, (John Wiley and Sons, 2012).

[37] R. Marchetti, C. Lacava, L. Carroll, K. Gradkowski, and P. Minzioni, "Coupling strategies for silicon photonics integrated chips [Invited]," Photon. Res. **7**, 201–239 (2019).

[38] H. Sakr, Y. Chen, G. T. Jasion, T. D. Bradley, J. R. Hayes, H. C. H. Mulvad, I. A. Davidson, E. N. Fokoua, and F. Poletti, "Hollow core optical fibres with comparable attenuation to silica fibres between 600 and 1100 nm," Nat. Commun. **11**, 6030 (2020).

[39] H. Sakr, T. D. Bradley, G. T. Jasion, E. N. Fokoua, S. R. Sandoghchi, I. A. Davidson, A. Taranta, G. Guerra, W. Shere, Y. Chen, J. R. Hayes, D. J. Richardson, and F. Poletti, "Hollow core NANFs with five nested tubes and record low loss at 850, 1060, 1300 and 1625nm," 2021 Optical Fiber Communications Conference and Exhibition (OFC), F3A.4 (2021).

[40] T. D. Bradley, G. T. Jasion, H. Sakr, I. A. Davidson, J. R. Hayes, A. Taranta, K. Harrington, E. N. Fokoua, Y. Chen, D. J. Richardson, F. Poletti, "Towards low loss hollow core optical fibers," Proceedings Volume 11713, Next-Generation Optical Communication: Components, Sub-Systems, and Systems X, 117130A (2021).

[41] F. Amrani,J. H. Osório, F. Delahaye, F. Giovanardi, L. Vincetti, B. Debord, F. Gérôme, and F. Benabid, "Low-loss single-mode hybrid-lattice hollow-core photonic-crystal fibre," Light: Sci. Appl. **10**, 7 (2021).

[42] T. D. Bradley, J. R. Hayes, Y. Chen, G. T. Jasion, S. R. Sandoghchi, R. Slavik, E. N. Fokoua, S. Bawn, H. Sakr, I.A. Davidson, A. Taranta, J. P. Thomas, M. N. Petrovich, D.J. Richardson and F. Poletti, "Record low-loss 1.3dB/km data transmitting antiresonant hollow core fibre," 2018 European Conference on Optical Communication (ECOC), 1–3 (2018).

[43] T. D. Bradley. G. T. Jasion, J. R. Hayes, Y. Chen, L. Hooper, H. Sakr, M. Alonso, A. Taranta, A. Saljoghei, H. C. Mulvad, M. Fake, I. A. Davidson, N. Wheeler, E. N. Fokoua, W. Wang, S. R. Sandoghchi, D. Richardson, and F. Poletti, "Antiresonant hollow core fibre with 0.65 dB/km attenuation across the C and L telecommunication bands," 45th European Conference on Optical Communication (ECOC 2019), 1–4 (2019).

[44] G. T. Jasion, T. D. Bradley, K. Harrington, H. Sakr, Y. Chen, E. N. Fokoua, I. A. Davidson, A. Taranta, J. R. Hayes, D. J. Richardson, and F. Poletti, "Hollow core NANF with 0.28 dB/km attenuation in the C and L bands," in Optical Fiber Communication Conference Postdeadline Papers 2020, Th4B.4 (Optical Society of America, 2020).

[45] M. Michieletto, J. K. Lyngsø, C. Jakobsen, J. Lægsgaard, O. Bang, and T. T. Alkeskjold, "Hollow-core fibers for high power pulse delivery," Opt. Express **24**, 7103–7119 (2016).

[46] J. D. Shephard, A. Urich, R. M. Carter, P. Jaworski, R. R. J. Maier, W. Belardi, F. Yu, W. J. Wadsworth, J. C. Knight, and D. P. Hand, "Silica hollow core microstructured fibers for beam delivery in industrial and medical applications," Front. Phys. **3**, 24 (2015).

[47] F. Giovanardi, A. Cucinotta, A. Rozzi, R. Corradini, F. Benabid, L. Rosa; L. Vincetti, "Hollow core inhibited coupling fibers for biological optical sensing," J. Lightwave Technol. **37**, 2598–2604 (2019).

[48] F. Benabid, J. Knight, G. Antonopoulos, P. Russell, "Stimulated Raman scattering in Hydrogen-filled hollow-core photonic crystal fiber," Science **298**, 399–402 (2002).

[49] A. V. V. Nampoothiri, A. M. Jones, C. Fourcade-Dutin, C. Mao, N. Dadashzadeh, B. Baumgart, Y.Y. Wang, M. Alharbi, T. Bradley, N. Campbell, F. Benabid, Brian R. Washburn, K. L. Corwin, and W. Rudolph, "Hollow-core optical fiber gas lasers (HOFGLAS): a review [Invited]," Opt. Mater. Express **2**, 948–961 (2012).

[50] F. Couny, F. Benabid, and P. S. Light, "Subwatt threshold cw Raman fiber-gas laser based on H_2-filled hollow-core photonic crystal fiber," Phys. Rev. Lett. **99**, 143903 (2007).

[51] R. Sollapur, D. Kartashov, M. Zürch, A. Hoffmann, T. Grigorova, G. Sauer, A. Hartung, A. Schwuchow, J. Bierlich, J. Kobelke, M. Chemnitz, M. A. Schmidt, and C. Spielmann. "Resonance-enhanced multi-octave supercontinuum generation in antiresonant hollow-core fibers," Light Sci. Appl. **6**, e17124 (2017).

[52] C. Wei, R. A. Kuis, F. Chenard, C. R. Menyuk, and J. Hu, "Higher-order mode suppression in chalcogenide negative curvature fibers," Opt. Express **23**, 15824–15832 (2015).

[53] C. Wei, C. R. Menyuk, and J. Hu, "Polarization-filtering and polarization-maintaining low-loss negative curvature fibers," Opt. Express **26**, 9528–9540 (2018).

[54] L. Provino, "Effect of Nested Elements on Avoided Crossing between the Higher-Order Core Modes and the Air-Capillary Modes in Hollow-Core Antiresonant Optical Fibers," Fibers **6**, 42 (2018).

[55] W. Bogaerts, P. D. Heyn, T. V. Vaerenbergh, K. D. Vos, S. K. Selvaraja, T. Claes, P. Dumon, P. Bienstman, D. V. Thourhout, and R. Baets, "Silicon microring resonators," Laser Photonics Rev. **6**, 47–73 (2012).

[56] J. von Neumann, E. P. Wigner, "Über merkwürdige diskrete eigenwerte," Physikalische Zeitschrift. **30**, 465–467 (1929).

[57] R. S. Mulliken, "Solved and unsolved problems in the spectra of diatomic molecules," J. of Phys. Chem. **41**, 5–45 (1937).

[58] A. G. Gaydon, and W. G. Penney. "The dissociation energies of CO, N_2, NO and CN." Proceedings of the Royal Society of London. Series A 183, 374–388 (1945).

[59] T. G. Eck, L. L. Foldy, and H. Wieder, "Observation of "anticrossings" in optical resonance fluorescence," Phys. Rev. Let. **10**, 239–242 (1963).

[60] D. Marcuse and I. P. Kaminow, "Modes of a symmetric slab optical waveguide in birefringent media, part II: slab with coplanar optical axis," J. Quantum Electron. **15**, 92–101 (1979).

[61] R. J. Spreeuw, J. P. Woerdman, and D. Lenstra, “Photon band structure in a Sagnac fiber-optic ring resonator,” Phys. Rev. Lett. **61**, 318–321 (1988).

[62] F. Jansen, F Stutzki, C Jauregui, J Limpert, and A Tünnermann, “Avoided crossings in photonic crystal fibers,” Opt. Express **19**, 13578–13589 (2011).

[63] C. M. Smith, N. Venkataraman, M. T. Gallagher, D. Müller, J. A. West, N. F. Borrelli, D. C. Allan, and Karl W. Koch, “Low-loss hollow-core silica/air photonic bandgap fibre,” Nature **424**, 657–659 (2003).

[64] J. A. West, C. M. Smith, N. F. Borrelli, D. C. Allan, and K. W. Koch, “Surfaces modes in air-core photonic band-gap fibers,” Opt. Express **12**, 1485–1496 (2004).

[65] K. Saitoh, N. A. Mortensen, and M. Koshiba, “Air-core photonic band-gap fibers: the impact of surface modes,” Opt. Express **12**, 394-400 (2004).

[66] J. Hu and C. R. Menyuk, “Leakage loss and bandgap analysis in air-core photonic bandgap fiber for nonsilica glasses,” Opt. Express **15**, 339–349 (2007).

[67] J. M. Fini, J. W. Nicholson, B. Mangan, L. Meng, R. S. Windeler, E. M. Monberg, A. DeSantolo, F. V. DiMarcello, and K. Mukasa, “Polarization maintaining single-mode low-loss hollow-core fibres,” Nat. Commun. **5**, 5085 (2014).

[68] B. Debord, F. Amrani, L. Vincetti, F. Gérôme, F. Benabid, “Hollow-Core Fiber Technology: The Rising of “Gas Photonics”,” Fibers **7**, 16 (2019).

[69] D. Noordegraaf, L. Scolari, J. Lægsgaard, T. T. Alkeskjold, G. Tartarini, E. Borelli, P. Bassi, J. Li, and S.-T. Wu, “Avoided-crossing-based liquid-crystal photonic-bandgap notch filter,” Opt. Lett. **33**, 986–988 (2008).

[70] T. Han, Y.-G. Liu, Z. Wang, B. Zou, B. Tai, and B Liu, “Avoided-crossing-based ultrasensitive photonic crystal fiber refractive index sensor,” Opt. Lett. **35**, 2061–2063 (2010).

[71] B. Shuai, L. Xia, Y. Zhang, and D. Liu, “A multi-core holey fiber based plasmonic sensor with large detection range and high linearity,” Opt. Express **20**, 5974–5986 (2012).

[72] A. Hassani and M. Skorobogatiy, “Surface plasmon resonance-like integrated sensor at terahertz frequencies for gaseous analytes.,” Opt. Express **16**, 20206–20214 (2008).

[73] J. Zuo, T. Han, J. Yang, Y. Chen, Y.-G. Lin, and J. Cai, “High sensitivity temperature sensor with an avoided-crossing based selective-filling high birefringent photonic crystal fiber Sagnac interferometer,” IEEE MC-SSN **6**, 45527–45533 (2018).

[74] F. Poli, E. Coscelli, T. T. Alkeskjold, D. Passaro, A. Cucinotta, L. Leick, J. Broeng, and S. Selleri, “Cut-off analysis of 19-cell Yb-doped double-cladding rod-type photonic crystal fibers,” Opt. Express **19**, 9896-9907 (2011).

[75] P. Uebel, M. C. Günendi, M. H. Frosz, G. Ahmed, N. N. Edavalath, J.-M. Ménard, and P. St. J. Russell, “Broadband robustly single-mode hollow-core pcf by resonant filtering of higher-order modes,” Opt. Lett. **41**, 1961–1964 (2016).

[76] N. M. Litchinitser, A. K. Abeeluck, C. Headley, and B. J. Eggleton, “Antiresonant reflecting photonic crystal optical waveguides,” Opt. Lett. **27**, 1592–1594 (2002).

[77] C. Wei, R. J. Weiblen, C. R. Menyuk, and J. Hu , “Negative curvature fibers” Adv. in Opt. Photon **9**, 504–561 (2017).

[78] C. Wei, J. Hu, C. R. Menyuk, “Comparison of loss in silica and chalcogenide negative curvature fibers as the wavelength varies,” Front. Phys. **4**, 30 (2016).

[79] M. A. Duguay, Y. Kokubun,T. L. Koch, L. Pfeiffer, “Antiresonant reflecting optical waveguides in SiO_2-Si multilayer structures,” Appl. Phys. Lett. **49**, 13–15 (1986).

[80] : C. R. Menyuk, J. T. Young, J. Hu, A. J. Goers, D. M. Brown, and M. L. Dennis, “Accurate and Efficient Modeling of the Transverse Mode Instability in High Energy Laser Amplifiers,” Opt. Express **29**(12), 17746–17757 (2021).

[81] M. N. Zervas and C. A. Codemard, “High power fiber lasers: A review,” IEEE J. Sel. Topics Quantum Electron. **20**(5), 219–241 (2014).

[82] C. Robin, I. Dajani, and B. Pulford,“Modal instability-suppressing, single-frequency photonics fiber with 811 W output power,” Opt. Lett. **39**(3), 666–669 (2014).

[83] L. Dong, F. Kong, G. Gu, T. W. Hawkins, M. Jones, J. Parsons, M. T. Kalichevsky-Dong, K. Saitoh, B. Pulford, and I. Dajani, “Large-mode-area all-solid photonic bandgap fibers for mitigation of optical nonlinearities,” IEEE J. Sel. Topics Quantum Electron. **22**(2), 4900207 (2016).

[84] F. Kong, G. Gu, T. W. Hawkins, M. Jones, J. Parsons, M. T. K.-Dong, Stephen P. Palese, E. Cheung, and L. Dong, “Efficient 240W single-mode 1018nm laser from an Ytterbium-doped 50/400µm all-solid photonic bandgap fiber,” Opt. Express **26**(3), 3138–3144 (2018).

[85] H. Chen, J. Cao, Z. Huang, Y. Ren, A. Liu, Z. Pan, X. Wang, and J. Chen, “Experimental investigations on multi-kilowatt all-fiber distributed side-pumped oscillators,” Laser Phys. **29**(7), 075103 (2019).

[86] M. Zervas, "Transverse mode instability, thermal lensing, and power scaling in Yb^{3+}-doped high-power fiber amplifiers," Opt. Express **27**(13), 19019–19041 (2019).

[87] C. Jauregui, T. Eidam, J. Limpert, and A. Tünnermann, "Impact of modal interference on beam quality of high-power amplifiers," Opt. Express **19**(4), 3258–3271 (2011).

[88] T. Eidam, C. Wirth, C. Jauregui, F. Stutzki, F. Jansen, H.-J. Otto, O. Schmidt, T. Schreiber, J. Limpert, and A. Tünnermann, "Experimental observations of the threshold-like onset of mode instabilities in high power fiber amplifiers," Opt. Express **19**(14), 13218–13224 (2011).

[89] A. V. Smith and J. J. Smith, "Mode instability in high power amplifiers," Opt. Express **19**(11), 10180–10192 (2011).

[90] C. Jauregui, T. Eidam, H.-J. Otto, F. Stutzki, F. Jansen, J. Limpert, and A. Tünnermann, "Physical origin of mode instabilities in high-power fiber laser systems," Opt. Express **20**(12), 12912–12925 (2012).

[91] L. Dong, "Stimulated thermal Rayleigh scattering in optical fibers," Opt. Express **21**(3), 2642–2656 (2013).

[92] A. V. Smith and J. J. Smith, "Overview of a steady-periodic model of modal instability in fiber amplifiers," IEEE J. Sel. Top. Quantum Electron. **20**(5), 3000112 (2014).

[93] F. Kong, J. Xue, R. H. Stolen, and L. Dong, "Direct experimental observation of stimulated thermal Rayleigh scattering with polarization modes in a fiber amplifier," Optica **3**(9), 975–978 (2016).

[94] B. Ward, C. Robin, and I. Dajani, "Origin of the thermal mode instabilities in large mode area fiber amplifiers," Opt. Express **20**(10), 11407–11422 (2012).

[95] S. Naderi, I. Dajani, T. Madden, and C. Robin, "Investigations of modal instabilities in fiber amplifiers through detailed numerical simulations," Opt. Express **21**(13), 16111–16129 (2013).

[96] B. G. Ward, "Modeling of transient modal instability in fiber amplifiers," Opt. Express **21**, 12053–12067 (2013).

[97] D. Marcuse, *Theory of Dielectric Waveguides* (Academic, 1991), Chap. 3.2.

[98] A. W. Snyder and J. D. Love, *Optical Waveguide Theory* (Chapman and Hall, 1983), Chap. 31.11.

[99] I. S. Gradshteyn and I. M. Rhyzik, *Table of Integrals, Series, and Products* (Academic, 1980), pp. 366, See item 3.613.1.

[100] H.-J. Otto, N. Modsching, C. Jauregui, J. Limpert, and A. Tünnermann, "Impact of photodarkening on the mode instability threshold," Opt. Express **23**(12), 15265–15277 (2015).

[101] Z. Li, C. Li, Y. Liu, Q. Luo, H. Lin, Z. Huang, S. Xu, Z. Yang, J. Wang and F. Jing, "Impact of stimulated Raman scattering on the transverse mode instability threshold," IEEE Phot. J. **10**(3), 085109 (2018).

[102] R. C. Hilborn, "Seagulls, butterflies, and grasshoppers: A brief history of the butterfly effect in nonlinear dynamics," Am. J. Phys. **72**(4), 425–427 (2004).

[103] H.-J. Otto, F. Stutzki, F. Jansen, T. Eidam, C. Jauregui, J. Limpert, and A. Tünnermann, "Temporal dynamics of mode instabilities in high-power fiber lasers and amplifiers," Opt. Express **20**(14), 15710–15722 (2012).

[104] H.-J. Otto, C. Jauregui, F. Stutzki, F. Jansen, and A. Tünnermann, "Controlling instabilities by dynamic mode excitation with an acoustic-optic detector," Opt. Express **21**(14), 19375–19386 (2013).

[105] W. H. Press, S. A. Teukolsky, W. T. Vetterling, B. P. Flannery, *Numerical Recipes*, 3rd edition (Cambridge, 2007), Chap. 4 and 17.

[106] J. W. Dawson, M. J. Messerly, R. J. Beach, M. Y. Shverdin, E. A. Stappaerts, A. K. Sridharan, P. H. Pax, J. E. Heebner, C. W. Siders, and C. P. J. Barty, "Analysis of the scalabiity of diffraction-limited fiber lasers and amplifiers to high average power," Opt. Express **16**(17), 13240–13266 (2008).

[107] See, e.g., M. Born and E. Wolf, *Principles of Optics* (Cambridge, 2005), Chap. 14.5.

[108] See, e.g., G. Keiser, *Optical Fiber Communications* (McGraw-Hill, 2002), Chap. 3.1.3.

[109] M. Fleyer, J. P. Cahill, M. Horowitz, C. R. Menyuk, and O. Okusaga, "Comprehensive model for studying noise induced by self-homodyne detection of backward Rayleigh schattering in optical fibers," Opt. Express **23**(20), 25635–25652 (2015).

[110] T. Zhu, X. Bao, L. Chen, H. Liang, and Y. Dong, "Experimental study on stimulated Rayleigh scattering in optical fibers," Opt. Express **18**(22), 22958–22963 (2010).

[111] O. Okusaga, J. P. Cahill, A. Docherty, W. Zhou, and C. R. Menyuk, "Guided entropy mode Rayleigh scattering in optical fibers," Opt. Lett. **37**(4), 683–685 (2012).

[112] O. Okusaga, J. P. Cahill, A. Docherty, C. R. Menyuk, and W. Zhou, "Spontaneous inelastic Rayleigh scattering in optical fibers," Opt. Lett. **38**(4), 549–551 (2013).

[113] I. Dajani, A. Flores, R. Holten, B. Anderson, B. Pulford, and T. Ehrenreich, "Multi-kilowatt power scaling and coherent beam combination of narrow-linewidth fiber lasers," Proc. SPIE **9728**, 972801 (2016).

[114] M. Vorontsov, G. Filimonov, V. Ovchinnikov, E. Polnau, S. Lachinova, T. Weyrauch, and J. Mangano, "Comparative efficiency analysis of fiber-array and conventional beam director systems in volume turbulence," Appl. Opt. **55**(15), 4170–4185 (2016).

[115] G. D. Goodno, S. J. McNaught, J. E. Rothenberg, T. S. McComb, P. A. Thielen, M. G. Wickham, and M. E. Weber, "Active phase and polarization locking of a 1.4 kW fiber amplifier," Opt. Lett. **35**(10), 1542–1544 (2010).

[116] A. Mussot, M. Le Parquier, and P. Szriftgiser, "Thermal noise for SBS suppression in fiber optical parametric amplifiers," Opt. Commun. **283**(12), 2607–2610 (2010).

[117] C. X. Yu, S. J. Augst, S. M. Redmond, K. C. Goldizen, D. V. Murphy, A. Sanchez, and T. Y. Fan, "Coherent combining of a 4 kW, eight-element fiber amplifier array," Opt. Lett. **36**(14), 2686–2688 (2011).

[118] V. R. Supradeepa, "Stimulated Brillouin scattering thresholds in optical fibers for lasers linewidth broadened with noise," Opt. Express **21**(4), 4677–4687 (2013).

[119] D. Brown, M. Dennis, and W. Torruellas, "Improved phase modulation for SBS mitigation in kW-class fiber amplifiers," presented at SPIE Photonics West, San Francisco, CA (January 24, 2011).

[120] A. Flores, T. Ehrehreich, R. Holten, B. Anderson, and I. Dajani, "Multi-kW coherent combining of fiber lasers seeded with pseudo random phase modulated light," Proc. SPIE **9728**, 97281Y (2016).

[121] P. I. Ionov and T. S. Rose, "SBS reduction in nanosecond fiber amplifiers by frequency chirping," Opt. Express **24**(13), 13763–13777 (2016).

[122] J. O. White, M. Harfouche, J. Edgecumbe, N. Satyan, G. Rakuljic, V. Jayaraman, C. Burgner, and A. Yariv, "1.6 kW Yb fiber amplifier using chirped seed amplification for stimulated Brillouin scattering suppression," Appl. Opt. **56**(3), B116–B122 (2017).

[123] A. Vasilyev, E. Petersen, N. Satyan, G. Rakuljic, A. Yariv, and J. O. White, "Coherent power combining of chirped-seed Erbium-doped fiber amplifiers," IEEE Photonics Technol. Lett. **25**(16), 1616–1618 (2013).

[124] E. Petersen, Z. Y. Yang, N. Satyan, A. Vasilyev, G. Rakuljic, A. Yariv, and J. O. White, "Stimulated Brillouin scattering suppression with a chirped laser seed: comparison of dynamical model to experimental data," IEEE J. Quantum Electron. **49**(12), 1040–1044 (2013).

[125] N. Satyan, A. Vasilyev, G. Rakuljic, V. Leyva, and A. Yariv, "Precise control of broadband frequency chirps using optoelectronic feedback," Opt. Express **17**(18), 15991–15999 (2009).

[126] V. Jayaraman, G. D. Cole, M. Robertson, C. Burgner, D. John, A. Uddin, and A. Cable, "Rapidly swept, ultrawidely-tunable 1060 nm MEMS-VCSELs," Electron. Lett. **48**(21), 1331–1333 (2012).

[127] A. V. Harish and J. Nilsson, "Optimization of phase modulation with arbitrary waveform generators for optical spectral control and suppression of stimulated Brillouin scattering," Opt. Express **23**(6), 6988–6999 (2015).

[128] B. M. Anderson, R. Hui, A. Flores, and I. Dajani, "SBS suppression and coherence properties of a flat top optical spectrum in a high power fiber amplifier," Proc. SPIE **10083**, 100830V (2017).

[129] A. V. Harish and J. Nilsson, "Optimization of phase modulation formats for suppression of stimulated Brillouin scattering in optical fibers," IEEE J. Sel. Topics in Quantum Elect. **24**, 5100110 (2018).

[130] Fringes occur in the raw triangle chirp spectrum due to the interference stemming from the same frequency occurring at two places in the period. For this reason, the raw spectrum has been smoothed on a very fine scale with a moving average over 69 MHz. This is close to the same averaging that will occur physically, by virtue of the 57.1 MHz Brillouin linewidth.

[131] R. W. Boyd, K. Rzążewski, and P. Narum, "Noise initiation of stimulated Brillouin scattering," Phys. Rev. A **42**(9), 5514–5521 (1990).

[132] C. Wang, M. Zhang, X. Chen, M. Bertrand, A. Shams-Ansari, S. Chandrasekhar, P. Winzer, and M. Lončar, "Integrated lithium niobate electro-optic modulators operating at CMOS-compatible voltages," Nature **562**(7725), 101–104 (2018).

[133] J. T. Young, A. J. Goers, D. M. Brown, M. L. Dennis, K. Lehr, C. Wei, C. R. Menyuk, and J. Hu, "Tradeoff Between the Brillouin and Transverse Mode Instabilities in Yb-doped Fiber Amplifiers," Opt. Express **30**(22), 40691–40703 (2022).

[134] M. N. Zervas and C. A. Codemard, "High power fiber lasers: A review," IEEE J. Sel. Topics Quantum Electron **20**(5), 219–241 (2014).

[135] A. David and M. Horowitz, "Low-frequency transmitted intensity noise induced by stimulated Brillouin scattering in optical fibers," Opt. Express **19**(12), 11792–11803 (2011).

[136] B. M. Cannon, D M. Brown, M. J. Mayr, M. L. Dennis, W E. Torruellas, and J. O. White, "High energy fiber laser amplifier with reduced optical linewidth," US patent 20180269645A1 (Sep. 20, 2018).

[137] K. R. Hansen, T. T. Alkeskjold, J. Broeng, and J. Lægsgaard, "Theoretical analysis of mode instability in high-power amplifiers," Opt. Express **21**(2), 1944–1971 (2013).

[138] F. Beier, C. Hupel, J. Nold, S. Kuhn, S. Hein, J. Ihring, B. Sattler, N. Haarlammert, T. Schreiber, R. Eberhardt, and A. Tünnermann, "Narrow linewidth, single mode 3 kW average power from a directly diode pumped ytterbium-doped low NA fiber amplifier," Opt. Express **24**(6), 6011–6020 (2016).

[139] L. Zeng, X. Xi, Y. Ye, X. Lin, X. Wang, J. Li, C. Shi, B. Yang, H. Zhang, P. Wang, P. Zhou, X. Xu, "A novel fiber laser oscillator employing saddle-shaped core ytterbium-doped fiber," Applied Physics B **126**, 185 (2020).

[140] F. Kong, G. Gu, T. W. Hawkins, M. Jones, J. Parsons, M. T. Kalichevsky-Dong, S. P. Palese, E. Cheung, and L. Dong, "Efficient 240W single-mode 1018nm laser from an Ytterbium-doped 50/400μm all-solid photonic bandgap fiber," Opt. Express **26**(3), 3138–3144 (2018).

[141] J. T. Young, C. R. Menyuk, C. Wei, and J. Hu, "Increasing the power threshold in fiber amplifiers considering both the transverse mode and Brillouin instabilities," in Proc. Conference on Lasers and Electro-Optics, 3691159 (2022).

[142] G. P. Agrawal *Nonlinear Fiber Optics* (Academic 2013).

[143] A. Kobyakov, S. Kumar, D. Q. Chowdhury, A. B. Ruffin, M. Sauer, S. R. Bickham, and R. Mishra, "Design concept for optical fibers with enhanced SBS threshold," Opt. Express **13**(14), 5338–5346 (2005).

[144] J. Hu, B. S. Marks, Q. Zhang, and C. R. Menyuk, "Modeling backward-pumped Raman amplifiers," J. Opt. Soc. Am. B, **22**(10), 2083–2090, (2005).

[145] F. Kong, C. Dunn, J. Parsons, M. T. Kalichevsky-Dong, T. W. Hawkins, M. Jones, and L. Dong, "Large-mode-area fibers operating near single-mode regime," Opt. Express **24**(10), 10295–10301 (2016).

[146] N. Haarlammert, B. Sattler, A. Liem, M. Strecker, J. Nold, T. Schreiber, R. Eberhardt, A. Tünnermann, K. Ludewigt, and M. Jung, "Optimizing mode instability in low-NA fibers by passive strategies," Opt. Lett. **40**(10), 2317–2320 (2015).

[147] D. Jain, Y. Jung, P. Barua, S. Alam, and J. K. Sahu, "Demonstration of ultra-low NA rare-earth doped step index fiber for applications in high power fiber lasers," Opt. Express **23**(6), 7407–7415 (2015).

[148] C. Ye, J. Koponen, T. Kokki, J. Montiel-Ponsoda, A. Tervonen, and S. Honkanen, "Confined-doped ytterbium fibers for beam quality improvement: Fabrication and performance," SPIE **8237**, 823737 (2012).

[149] K.-H. Lee, K. Lee, Y. Kim, Y.-H. Cha, G. Lim, H. Park, H. Cho, and D.Y. Jeong, "Transverse mode instability induced by stimulated Brillouin scattering in a pulsed single-frequency large-core fiber amplifier," Appl. Opt. **54**(2), 189–194 (2015).

[150] J. Koponen, M. J. Söderlund, S. K. T. Tammela, H. Po, "Photodarkening in ytterbium-doped silica fibers," Proc. SPIE **5990**, 99008 (2005).

[151] Y. Wang, F. Couny, P. J. Roberts, and F. Benabid, "Low loss broadband transmission in optimized core-shaped Kagome hollow-core PCF," in Conference on Lasers and Electro-Optics (CLEO), CPDB4 (2010).

[152] Y. Wang, N. V. Wheeler, F. Couny, P. J. Roberts, and F. Benabid, "Low loss broadband transmission in hypocycloid-core Kagome hollow-core photonic crystal fiber," Opt. Lett. **36**(5), 669–671 (2011).

[153] F. Yu, and J. C. Knight, "Negative curvature hollow-core optical fiber," IEEE J. Sel. Top. Quantum Electron. **22**(2), 4400610 (2016).

[154] C. Wei, J. T. Young, C. R. Menyuk, and J. Hu, "Temperature sensor based on liquid-filled negative curvature optical fibers," OSA Continuum **2**(7), 2123–2130 (2019).

[155] A. V. Gladyshev, A. F. Kosolapov, M. M. Khudyakov, Y. P. Yatsenko, A. N. Kolyadin, A. A. Krylov, A. D. Pryamikov, A. S. Biriukov, M. E. Likhachev, I. A. Bufetov, and E. M. Dianov, "4.4 μm Raman laser based on hollow-core silica fibre," Quantum Electron. **47**(5), 491–494 (2017).

[156] M. S. Astapovich, A. N. Kolyadin, A. V. Gladyshev, A. F. Kosolapov, A. D. Pryamikov, M. M. Khudyakov, M. E. Likhachev, and I. A. Bufetov, "Efficient 1556 to 4400 nm hydrogen Raman laser based on hollow-core silica fiber," Proc. 2018 International Conference Laser Optics (ICLO), 312–312 (2018).

[157] F. B. A. Aghbolagh, V. Nampoothiri, B. Debord, F. Gerome, L. Vincetti, F. Benabid, and W. Rudolph, "Mid IR hollow core fiber gas laser emitting at 4.6 µm," Opt. Lett. **44**(2), 383–386 (2019).

[158] I. T. Sorokina, and K. L. Vodopyanov, *Solid-state mid-infrared laser sources*, (Springer, 2003).

Josh Young

5512 Old Caufield Ranch Rd, McGregor, TX 76657

www.linkedin.com/in/josh-young-TX cell: **254-640-1645**

scholar.google.com/citations?user=XSormbcAAA email: **joshyoung0830@gmail.com**

CAREER PROFILE

PhD in electrical engineering with a focus on nonlinear effects in high-energy laser (HEL) systems to maximize system power. Possesses strong technical and analytical prowess for designing and implementing simulation tools for modeling the physics within HEL systems. Ability to communicate abstract, technical concepts to non-technical individuals.

EDUCATION

BAYLOR UNIVERSITY – Waco, TX

Doctor of Philosophy of Electrical and Computer Engineering December 2022

- GPA: 3.93
- Research/Teaching assistant

BAYLOR UNIVERSITY – Waco, TX

Bachelor of Science of Electrical and Computer Engineering December 2017

- GPA: 3.73
- Tau Sigma, Eta Kappa Nu

EXPERIENCE

BAYLOR UNIVERSITY – Waco, TX

Research Assistant **2017 – present**

- Modeled suppression techniques for nonlinear effects to increase output power

- Incorporated the phase-matched model for transverse mode instability to reduce simulation wall time 100 fold
- Examined the interaction between nonlinear effects in high energy lasers

Teaching Assistant **2018 – present**

- Directed Optics lab and demonstrated laser safety using Class 3 laser
- Supervised Embedded Systems and Electronics Design labs of 20+ students

President of Baylor OPTICA Student Chapter **2017 – present**

- Established "Fun in Optics" seminar series to increase awareness regarding
- Hosted monthly Journal Clubs consisting of an average of 6 members
- Led outreach events to recruit potential freshmen from visiting high school students

396MARO CREATIONS – McGregor, TX

Owner/Designer **2021 – present**

- Managed and operated automotive aftermarket business
- Designed and created aftermarket automotive products for 36 different model years of classic and modern vehicles
- Shipped products and provided service internationally across 5 different countries

YOUNG ELECTRIC – McGregor, TX

Electrician **2014 – 2017**

- Diagnosed and debugged circuits to reduce costs by 40%
- Implemented electrical infrastructure systems in 3 banks, 1 police station, and numerous houses and restraunts

ADDITIONAL

AWARD

- Directed Energy Professional Society (DEPS) fellow (2020, 2021, 2022)

SKILLS

- Technical Skills: C++, Visual Basic, Matlab, Solidworks, Fusion360, Programming
- Classic car restorer: Restored and customized classic cars

PROFESSIONAL SERVICES

- Reviewer for IEEE Photonics Journal
- CNC routing and 3D printing design consultant

PUBLICATIONS

JOURNAL PUBLICATIONS

[1] **J. T. Young**, C. R. Menyuk, and J. Hu, "SBS suppression using PRBS phase modulation with different orders," Opt. Express, (conditional acceptance) (2022).

[2] **J. T. Young**, A. J. Goers, D. M. Brown, M. L. Dennis, K. Lehr, C. Wei, C. R. Menyuk, and J. Hu, "Tradeoff Between the Brillouin and Transverse Mode Instabilities in Yb-doped Fiber Amplifiers," Opt. Express **30**(22), 40691–40703 (2022).

[3] **J. T. Young**, C. Wei, J. Hu, and C. R. Menyuk, "Mode Coupling at the Avoided Crossings in Slab Waveguides with Comparison to Optical Fibers: Tutorial" J. Opt. Soc. Am. B **38**, F104–F114 (2021).

[4] C. R. Menyuk, **J. T. Young**, J. Hu, A. J. Goers, D. M. Brown, and M. L. Dennis, "Accurate and Efficient Modeling of the Transverse Mode Instability in High Energy Laser Amplifiers," Opt. Express **29**, 17746–17757 (2021).

[5] J. White, **J. T. Young**, C. Wei, J. Hu, and C. R. Menyuk, "Seeding fiber amplifiers with piecewise parabolic phase modulation for high SBS thresholds and compact spectra," Opt. Express **27**, 2962–2974 (2019).

[6] C. Wei, **J. T. Young**, C. R. Menyuk, and J. Hu, "Temperature sensor based on liquid-filled negative curvature optical fibers," OSA Continuum **2**, 2123–2130 (2019).

CONFERENCE PROCEEDINGS

[1] **J. T. Young**, J. Hu, and C. R. Menyuk, "Limitations of the power threshold for fiber amplifiers under both the Brillouin and transverse mode instabilities," SPIE, (2023).

[2] **J. T. Young**, J. Hu, and C. R. Menyuk, "Efficient modeling of the transverse mode instability using the phase-matched model," WSOF, Adelaide, South Australia # 731, (2022).

[3] **J. T. Young**, C. R. Menyuk, C. Wei, and J. Hu, "Increasing the power threshold in fiber amplifiers considering both the transverse mode and Brillouin instabilities," in Proc. Conference on Lasers and Electro-Optics (CLEO), San Jose, CA, paper # 3691159, (2022).

[4] **J. T. Young**, C. R. Menyuk, and J. Hu, "Comparison of the full model and phase-matched model for transverse mode instability," in Proc. Conference on Lasers and Electro-Optics (CLEO), San Jose, CA, paper #3699843, (2022).

[5] **J. T. Young**, J. O. White, C. Wei, J. Hu, and C. R. Menyuk, "Comparison of piecewise parabolic and PRBS phase modulation schemes on the SBS threshold," (FiO/LS), Virtual Conference, FTh4E.4 (2021).

[6] C. R. Menyuk, **J. T. Young**, Jonathan Hu, A. J. Goers, D. M. Brown, and M. L. Dennis, "Accurate and Efficient Modeling of the Transverse Mode Instability in High-Energy Laser Amplifiers Using the Phase-Matched Model," SPIE 11867-8 (2021) **[Invited]**.

[7] **J. T. Young**, J. O. White, C. Wei, J. Hu, and C. R. Menyuk, "Piecewise Parabolic Phase Modulation Scheme for Suppression of Stimulated Brillouin Scattering," in IEEE Photonics Conference (IPC), Virtual Conference, WE3.3 (2020).

[8] C. Wei, **J. T. Young**, C. R. Menyuk, and J. Hu, "Impact of the Glass Thickness in Fluid-Filled Negative Curvature Fibers for Temperature Sensing," in Frontiers in Optics + Laser Science (FiO/LS), Washington DC, JW4A.5 (2019).

[9] C. Wei, **J. T. Young**, C. R. Menyuk, and J. Hu, "Temperature Sensor Using Fluid-Filled Negative Curvature Fibers," in Proc. Conference on Lasers and Electro-Optics (CLEO), San Jose, CA, paper #2929860, (2018).